Energy & Environmental Science

REVIEW

View Article Online
View Journal | View Issue

Cite this: *Energy Environ. Sci.*, 2018, **11**, 1945

New horizons for inorganic solid state ion conductors

Zhizhen Zhang,[ab] Yuanjun Shao,[a] Bettina Lotsch,[c] Yong-Sheng Hu,[a] Hong Li,[a] Jürgen Janek,*[d] Linda F. Nazar,*[b] Ce-Wen Nan,*[e] Joachim Maier,*[c] Michel Armand*[f] and Liquan Chen*[a]

Among the contenders in the new generation energy storage arena, all-solid-state batteries (ASSBs) have emerged as particularly promising, owing to their potential to exhibit high safety, high energy density and long cycle life. The relatively low conductivity of most solid electrolytes and the often sluggish charge transfer kinetics at the interface between solid electrolyte and electrode layers are considered to be amongst the major challenges facing ASSBs. This review presents an overview of the state of the art in solid lithium and sodium ion conductors, with an emphasis on inorganic materials. The correlations between the composition, structure and conductivity of these solid electrolytes are illustrated and strategies to boost ion conductivity are proposed. In particular, the high grain boundary resistance of solid oxide electrolytes is identified as a challenge. Critical issues of solid electrolytes beyond ion conductivity are also discussed with respect to their potential problems for practical applications. The chemical and electrochemical stabilities of solid electrolytes are discussed, as are chemo-mechanical effects which have been overlooked to some extent. Furthermore, strategies to improve the practical performance of ASSBs, including optimizing the interface between solid electrolytes and electrode materials to improve stability and lower charge transfer resistance are also suggested.

Received 10th April 2018,
Accepted 4th June 2018

DOI: 10.1039/c8ee01053f

rsc.li/ees

Broader context

Driven by the necessity to reduce greenhouse effects caused by the emission of CO_2, the development of new electrochemical energy conversion and storage devices is of prime significance. Lithium ion batteries have revolutionized the portable electronics industry but may not be able to satisfy future customers' demands in the field of large-scale energy storage systems such as electrical vehicles and power grids. In particular, safety concerns have been a long-standing issue hindering the development of commercial liquid batteries with liquid organic electrolytes. In this context, all solid-state batteries (ASSBs) based on solid electrolytes (SEs) can not only address safety concerns, but may also enable the use of high voltage cathode materials and Li/Na metal anodes to enable long life and high energy density batteries. As the most important component in ASSBs, the SE determines the power density, long cycle stability and the safety of batteries. In this review a state of art and comprehensive description of the recent developments in SEs will be given, and general descriptors to guide the design of SEs are proposed. Critical issues of SEs with respect to their potential problems for practical applications (*e.g.*, the chemical and electrochemical stability of SE, chemo-mechanical effects, large charge transfer resistance at the interface) are discussed, and strategies to overcome these obstacles are also proposed.

1. Introduction

The development of electrochemical energy conversion and storage devices is one of the most important challenges to alleviate the greenhouse effects caused by emission of CO_2.[1,2] Owing to their high specific energy, large-scale rechargeable batteries have recently become highly sought after for applications in power grids and electric vehicles.[2,3] However, the flammable,

[a] *Key Laboratory for Renewable Energy, Beijing Key Laboratory for New Energy Materials and Devices, Beijing National Laboratory for Condensed Matter Physics, Institute of Physics, Chinese Academy of Sciences, School of Physical Sciences, University of Chinese Academy of Sciences, Beijing 100190, China. E-mail: lqchen@aphy.iphy.ac.cn*
[b] *Department of Chemistry, Waterloo Institute of Nanotechnology, University of Waterloo, 200 University Avenue West, Waterloo, Ontario, N2L 3G1, Canada. E-mail: lfnazar@uwaterloo.ca*
[c] *Max Planck Institute for Solid State Research, Stuttgart 70569, Germany. E-mail: s.weiglein@fkf.mpg.de*
[d] *Institute of Physical Chemistry & Center for Materials Research, Justus-Liebig-University Giessen, Heinrich-Buff-Ring 17, 35392 Giessen, Germany. E-mail: Juergen.Janek@phys.Chemie.uni-giessen.de*
[e] *School of Materials Science and Engineering, Tsinghua University, Beijing 100084, China. E-mail: cwnan@mail.tsinghua.edu.cn*
[f] *CIC Energigune, Alava Technology Park, Albert Einstein, 4801510 MIÑANO Álava, Spain. E-mail: marmand@cicenergigune.com*

reactive organic electrolytes used in conventional batteries incur severe safety issues.[4] In addition, although Li metal has an extremely high theoretical specific capacity (3860 mA h g^{-1}), low mass and the lowest negative electrochemical potential (−3.04 V *vs.* SHE), rechargeable batteries using Li metal have not been commercialized because of lithium metal's low cycling efficiency and tendency to form dendrites during repeated charge/discharge.[5,6] The only exceptions are the Blue Solutions™ batteries for EVs and buses that use a polymer electrolyte that operates at about 70 °C instead of a liquid electrolyte.

In this context, all solid-state batteries (ASSBs) based on solid electrolytes (SEs) can not only address safety concerns, but may also enable the use of high voltage cathode materials and Li/Na metal anodes to allow for long-term stable and high energy density batteries. An increase of more than 20% in energy density (depending on additional cathode capacity at high voltage) can be achieved by increasing the cell voltage from 4.2 V to 5 V.[7] Oxide-based inorganic solid electrolytes can endure such high voltages whereas liquid electrolytes are not stable at such very oxidizing potentials.[7] ASSBs exhibit additional advantages including low self-discharge, versatile geometries, high thermal stability, and thus wide operating temperature,[2] and as well as resistance to shocks and vibrations.[8] Moreover, the solidification of the electrolyte allows for the design of high-voltage bipolar stacked batteries and effectively decreases the dead space between single cells with thinner current collectors.

The SE is the most vital component in solid-state batteries – together with the electrode materials – as it determines the power density, long-term stability and the safety of the batteries. To realize ASSBs that can operate at ambient and moderate

Zhizhen Zhang

Zhizhen Zhang is currently a postdoctoral fellow in Linda F. Nazar's group at the University of Waterloo. She received her PhD degree in condensed matter Physics from the Institute of Physics, Chinese Academy of Sciences. Her research mainly focuses on solid electrolytes, interface stability study of solid-state batteries and the understanding of ion transport in fast ion conductors by DFT calculations.

Jürgen Janek

Jürgen Janek holds a chair for Physical Chemistry at Justus-Liebig University in Giessen (Germany) and is scientific director of BELLA, a joint lab of BASF SE and KIT in Karlsruhe/Germany. He received his doctoral degree in physical chemistry under supervision of Hermann Schmalzried and Alan B. Lidiard. He was visiting professor at Seoul National University, Tohuku University and Université d'Aix-Marseille, and got several awards for his scientific work. His research spans a wide range from fundamental transport studies in mixed conductors and at interfaces to in situ studies in electrochemical cells. Current key interests include new solid electrolytes and solid electrolyte interfaces.

Linda F. Nazar

Linda F. Nazar received her PhD degree in materials chemistry from the University of Toronto, and has held a Senior Canada Research Chair in Energy Materials at the University of Waterloo since 2004. She has been a visiting professor at the Institut des Matériaux Jean Rouxel and the CNRS Grenoble in France, at UCLA, and at Caltech as a Moore Scholar. Dr Nazar is the recipient of several academic and professional awards, and was elected an Officer of the Order of Canada in 2015. Her research interests extend over a wide range of solid state electrochemistry and ionics, including solid electrolytes, and Li and Na-ion solid state batteries.

Cewen Nan

Ce-Wen Nan is a Professor of School of Materials Science and Engineering, Tsinghua University, Beijing, China. Before joining the faculty of Tsinghua University in 1999, he had worked in Wuhan University of Technology, China, since 1985. He was elected to the Chinese Academy of Sciences in 2011 and as a Fellow of TWAS – the academy of sciences for the developing world in 2012. His recent research focuses on solid state electrolytes, polymer-based composites, multiferroic materials, and thermoelectric oxides.

temperatures, SEs with high ion conductivity ($>10^{-4}$ S cm^{-1}, better $>10^{-3}$ S cm^{-1} in case of thick composite electrodes),[9] negligible electronic conductivity ($<10^{-12}$ S cm^{-1}),[9] and a wide electrochemical window[10,11] are necessary. The greatest obstacles to the integration of SEs into batteries are the inherently poor ion conductivity of most SEs and the large resistance at the interface between the SE and active material, but also chemo-mechanical issues related to volume changes of active materials. Favorable interfacial contact and chemical stability between the SE and the electrode materials are both critical to achieve good electrochemical performance. The electrode–electrolyte interface particularly becomes an issue if nanostructured electrodes are to be considered and/or if large volume variations arise during cycling.[12–14] The chemical stability of SEs is not necessarily better than that of liquid electrolytes and, in the majority of cases, relies on kinetic, not thermodynamic factors (as in liquid systems).

Inorganic conductors and organic polymers are the most commonly used solid electrolyte materials in ASSBs. The former are characterized by high ion conductivity ($>10^{-4}$ S cm^{-1}) in many cases and high thermal stability. Furthermore, typical inorganic SEs are single ion conductors that preclude concentration polarization effects. However, ASSBs using inorganic ceramics often exhibit lower-than-expected electrochemical performance due to their poor interfacial contact with the electrode material.[4,15] Inorganic ceramics and organic polymers differ greatly in their mechanical properties and are thus suitable for different battery designs. The high elastic moduli of ceramics lead to poor processability because of their brittleness and hardness. Nevertheless, they are appropriate for rigid battery designs, such as thin-film batteries. In contrast, polymer electrolytes are well suited for flexible battery designs owing to their low elastic moduli. However, they suffer from other drawbacks, such as low ion conductivity ($<10^{-5}$ S cm^{-1} at ambient temperature), low cation transference number ($t_+ \approx 0.2$–0.5) unless the anion itself is tethered to a polymer and poor oxidation resistance.[16] Ceramic/polymer composite electrolytes may combine the high conductivity of ceramics and excellent flexibility of polymers and hence have recently attracted much attention.[17]

Full reviews of inorganic Li-ion conductors were published by Knauth in 2009,[18] Shao-Horn's group in 2015,[19] and Chen *et al.* in 2016,[20] in addition to many other shorter articles which focus on specific classes of SEs, including perovskites[21] and garnets.[22] Brief accounts of the pros and cons of solid electrolytes in battery systems have been recently provided.[7,23] Following the fast progress in the search for new and optimized SEs, our current review gives an up-to-date, yet comprehensive description of the

Joachim Maier

Joachim Maier received his PhD at the University of Saarbrücken in 1982, and completed his habilitation at the University of Tübingen in 1988. He has lectured at the University of Tübingen, at the Massachusetts Institute of Technology as a foreign faculty member, at the University of Graz as a visiting professor, and at the University of Stuttgart as an honorary professor. As director of the physical chemistry department (since 1991) of the Max Planck Institute for Solid State Research he co-authored more than 800 papers on chemical and electrochemical phenomena. His major interest are solid state ionics, electrochemistry and nanoionics.

Michel Armand

Michel Armand is Directeur de Recherche at CNRS since 1989, Lawrence Berkeley Laboratory (1982–1983). Professor, University of Montreal (1995–2004). Now sharing his time between CIC Energigune (Spain), CNRS (France) and Deakin University (Australia). He proposed several concepts that resulted in practical applications for energy-related electrochemistry: he ushered the concept of intercalation (1972) then of polymer electrolytes (1978), followed by new families of highly conductive salts (perfluorosulfonimides and Hückel-stabilized anions) for liquid, polymer electrolytes and as base for ionic liquids. The carbon "nanopainting" process has made $LiFePO_4$@C the safest cathode. Innovations in redox-active organics include polyquinones and aromatic dicarboxylates.

Liquan Chen

Liquan Chen is an Academician of Chinese Academy of Engineering. He is a professor in the Institute of Physics, Chinese Academy of Sciences. His major research area is solid state ionics. His research activity is related to ion and/or electron transport in solid state materials related with rechargeable lithium batteries. He has made great contribution to the development of Li-ion batteries in China. In recent years he has studied solid state lithium batteries and sodium batteries as well as aqueous Li-ion and Na-ion batteries.

recent exciting developments in inorganic solid electrolytes, including Na-ion conductors and covering both oxide and sulfide-based materials. Based on a survey of the previous studies, the major factors that influence the ion conductivity are summarized and general descriptors that govern conductivity are also proposed. Even though low-conductivity phases (*e.g.* LiF) may act as relevant electrolytes for very thin film systems, we concentrate here on bulk phases with high conductivities above 10^{-4} S cm^{-1}. Finally, the chemical and electrochemical stabilities of SEs against Li/Na metal and electrode materials are evaluated, a topic that has been somewhat overlooked except in a few recent reports.[14,23–25] Moreover, strategies to enhance the stability of SEs and to modify the interface between the SEs and electrode layers are proposed.

2. Lithium ion conductors

Crystalline ion conductors exhibit better thermal stability than polymeric materials. However, several difficulties arise for crystalline electrolytes that are associated with their grain boundaries and their fabrication into thin sheets or layers. Grain boundaries in polycrystalline conductors can lead to a locally perturbed structure – often in conjunction with high defect concentrations[9] – which may cause a large resistive barrier and hinder ion migration across the interface in materials with otherwise high bulk conductivity. The transport of mobile ions across grain boundaries thus becomes the rate-determining step. The opposite effect can also occur: in solid electrolytes with low bulk conductivity, a high fraction of grain boundaries (*i.e.*, in nanostructured materials) may improve the total conductivity by providing better transport paths. The beneficial effect of interfaces on ion transport is highlighted in Section 4.2.

Compared to crystalline ceramic materials, glasses are superior in terms of isotropic conductivity and lack of grain boundaries. From the technological point of view, glasses are often easy to process into thin films. The use of thin film separators can significantly reduce the internal resistance of batteries. For practical applications, the minimum conductivity required depends on the thickness of the separator layer. A total Li ion conductivity greater than 10^{-6} S cm^{-1} is required in order to avoid having to use a separator thickness well below one micron to minimize the IR drop across the film. Lithium phosphorous oxide nitride (LiPON) is one of the successful examples that has been employed in thin-film solid-state batteries. LiPON is an amorphous phase deposited by magnetron sputtering of Li_3PO_4 in a N_2 atmosphere.[26] The conductivity is a function of the N/O ratio and deposition conditions, with the maximum reported conductivity being *ca.* 2×10^{-6} S cm^{-1} to 3.3×10^{-6} S cm^{-1}.[27–31] Aside from their moderate ion conductivity, LiPON films exhibit very low electronic conductivities (8×10^{-14} S cm^{-1}), making them appropriate for practical applications.[32,33] LiPON can also be used as a protective layer in conventional lithium ion batteries. Thin-film solid-state batteries containing LiPON film as the electrolyte, Li or V_2O_5 as the anode, and $LiMn_2O_4$ or $LiCoO_2$ as the cathode display excellent cycling performance.[32,33] Another important family of glasses is based on mixtures of Li_2S and P_2S_5, where conductivity on the order of 10^{-3} S cm^{-1} has been reported with the addition of lithium halides.[34–36] Interest in glasses has reignited recently due to observations of dendrite growth through grain boundaries in polycrystalline ion conductors such as LLZO.[37–39] A particularly important advance was reported by Hayashi in 2014, where an extremely high conductivity of 1.7×10^{-2} S cm^{-1} was reported for a Li_2S–P_2S_5 glass-ceramic phase.[40] By employing glasses, unavoidable local mechanical pressure during cycling in ASSBs may be better compensated, while protective interphases are necessary in order to stabilize anode and/or cathode contacts. Although this review focusses on crystalline oxide and sulfide conductors owing to several major breakthroughs in crystalline conductors, some discussion on glasses and glass-ceramics is also covered here.

2.1 Crystalline conductors

A wide variety of lithium metal oxides, sulfides, phosphates, nitrides, and halides have been shown to exhibit high ion conductivities, as summarized in Fig. 1.[41–52] LiI,[53] Li_3N,[54] Li–β″-Al_2O_3,[55,56] and LiSICON[51] were the first studied. Although single crystals of Li_3N possess a high ion conductivity (10^{-3} S cm^{-1} at room temperature),[57] the low decomposition voltage of Li_3N[57] (0.44 V based on thermodynamic considerations) and its extreme sensitivity toward moisture have limited its practical use. Nonetheless, thin films of Li_3N formed *in situ* by reaction of Li with N_2 gas can be used to protect other SEs from direct contact with Li.[58] Sputtering of Cu_3N followed by evaporation of Li metal results in a Cu^0/Li_3N composite that has been used to

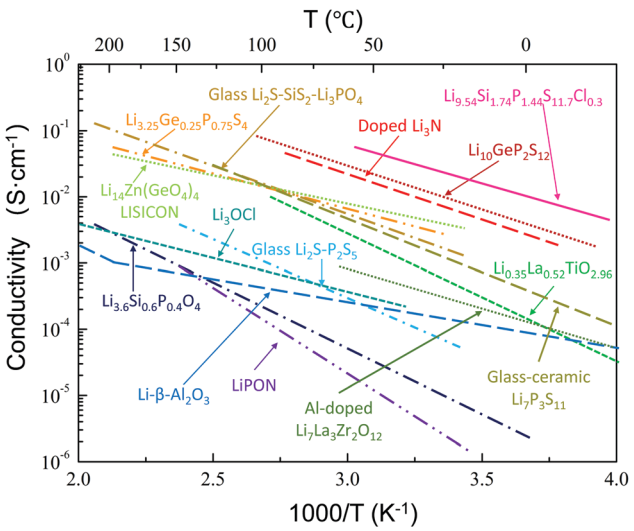

Fig. 1 Ion conductivity of several well-known solid lithium ion conductors, including glass and crystalline conductors. The data are taken from ref. 41–52. Reproduced with permission from ref. 41, 44, 51. Copyright (1978, 1993, 2017), Elsevier. Reproduced with permission from ref. 42. Copyright (2001), The Electrochemical Society. Reproduced with permission from ref. 43, 48. Copyright (2005, 2011), Wiley. Reproduced with permission from ref. 45, 46. Copyright (2011, 2016), Springer Nature. Reproduced with permission from ref. 47, 49, 50, 52. Copyright (2002, 2012, 2016), American Chemical Society.

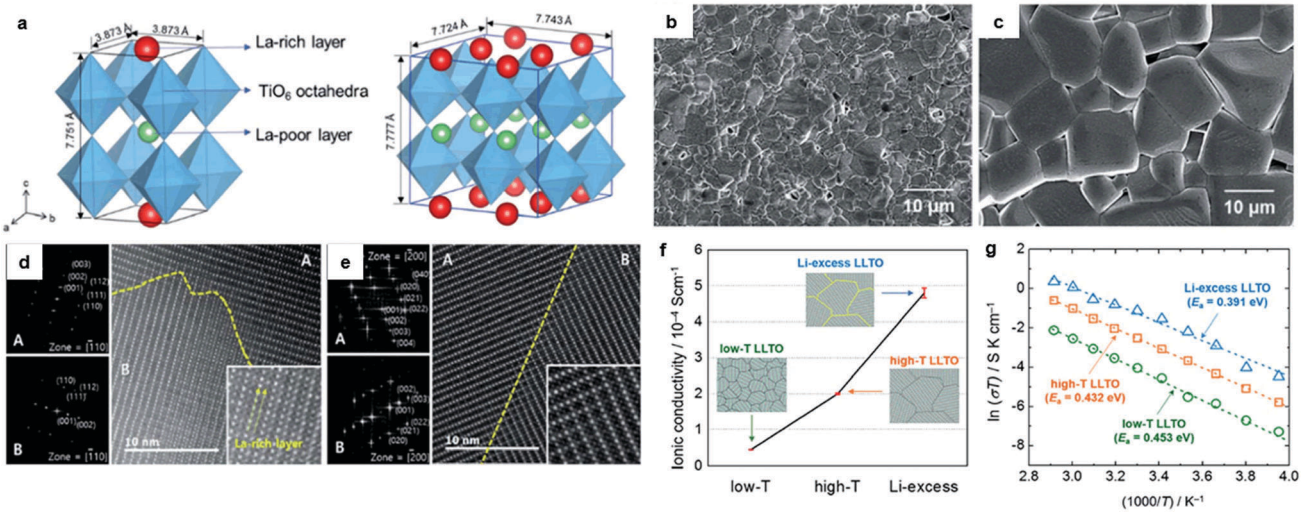

Fig. 2 (a) A schematic of the crystal structures of LLTOs: a tetragonal structure (left) and orthorhombic structure (right). FESEM micrographs of LLTOs sintered at different temperatures; (b) low-*T* LLTO (1200 °C) and (c) high-*T* LLTO (1400 °C). HRTEM images combined with SAEDs of (d) low-*T* LLTO and (e) high-*T* LLTO (magnified images are given in the inset): (f) a comparison of Li^+ conductivities along with schematics of the domain microstructures of the LLTO electrolytes: low-*T* LLTO, high-*T* LLTO and Li-excess LLTO. (g) Arrhenius plots of the boundary conductivities for low-*T* LLTO, high-*T* LLTO and Li-excess LLTO measured over a temperature range of 20 °C to 70 °C. The activation energy (E_a) values calculated are indicated.[90] Reproduced with permission from ref. 90. Copyright (2017), the Royal Society of Chemistry.

protect another solid electrolyte.[59] Single crystals of Li–β″-Al_2O_3 also show excellent conductivity (3×10^{-3} S cm^{-1}) at room temperature.[55,56] However, this phase is unlikely to be used in practical applications, since it is extremely hygroscopic and difficult to prepare dry.[55,56] Following this early work on Li solid electrolytes, several classes of materials were developed. In the following we will discuss the most important inorganic crystalline Li ion conductors. These can be classified as $Li_{3x}La_{2/3-x}\square_{1/3-2x}TiO_3$ (LLTO, perovskite),[50] Li_3OCl (anti-perovskite),[60] $Li_{14}ZnGe_4O_{16}$ (LiSICON),[51] $Li_{1.3}Ti_{1.7}Al_{0.3}(PO_4)_3$ (NaSICON type),[52] $Li_7La_3Zr_2O_{12}$ (garnet),[22] Thio-LiSICON,[61] Li_6PS_5X (X = Cl, Br, I), argyrodites,[62] and $Li_{10}MP_2S_{12}$, (M = Ge, Sn).[45,63]

2.1.1 Oxide based lithium ion conductors

2.1.1.1 Perovskite type conductors. $Li_{3x}La_{2/3-x}\square_{1/3-2x}TiO_3$ (LLTO, $0.04 < x < 0.17$) and its variants have attracted much interest because of their high bulk ion conductivities ($\sim 10^{-3}$ S cm^{-1}),[50] negligible electronic conductivities under normal conditions,[64] and wide electrochemical windows (reported to be greater than 8 V). LLTO has a perovskite (ABO_3) structure, with the A-sites partially occupied by Li or La. The A-site cations are not randomly distributed, but are ordered to form alternately stacked La-rich (La1) and La-poor (La2) layers along the *c* axis.[65–70] Previous studies have shown that the Li-ion conducting behavior in the grain interior is highly dependent on the crystal structure, composition (*e.g.*, A-site vacancy concentration, the degree of A site cation ordering, and dopants) and structural distortions.[65–70] Li-ion jump events occur only when adjacent vacant A-site cavities are available.[21] The Li-poor ($0.03 \leq x < 0.1$) compositions are reported to show orthorhombic symmetry (Fig. 2a), with high La occupancy in the La-rich layer (Fig. 2d) and anti-phase tilted TiO_6 octahedra along the *b* axis;[65–70] while in Li-rich ($0.1 \leq x < 0.167$) compositions, the symmetry becomes tetragonal[70] (Fig. 2a) and the degree of La ordering decreases as the Li^+ content increases (Fig. 2e). The dimension of the Li^+ trajectory is determined by the Li^+ ion concentration and the A-site vacancy. In the Li-poor LLTO, the La-rich layer acts as a barrier to Li^+ diffusion in the [001] direction because of the high La occupancy (~ 0.95) and low vacancy concentration (~ 0.05). The 2D Li ion pathways are thus predominantly confined within the La-poor layer.[67] On the other hand, Li-rich LLTO has relatively low La occupation (0.65)[71] and a higher concentration of vacancies and Li ions in the La-rich layer. In the latter, the Li migration between alternating La1 and La2 layers becomes possible, resulting in 3D conduction, at least within certain regions.

To further improve the conductivity, efforts have been made to substitute the A-site La^{3+} (ref. 72 and 73) and/or B-site Ti^{4+}.[74–77] However, only the substitution of Sr^{2+},[72] Ba^{2+},[78] and Nd^{3+} (ref. 79) for La^{3+} and the partial substitution of Al^{3+} (ref. 74–76) or Ge^{4+} (ref. 77) for Ti^{4+} offer improvement in the bulk conductivity, which is nonetheless marginal.

Earlier studies also found the total conductivity of LLTOs is governed by ion transfer across the grain boundary (GB). The latter conductivities are reported to be in the order of 10^{-4}–10^{-5} S cm^{-1}, which is about 1–2 orders of magnitudes lower than that of the bulk. Scrutiny through high-resolution transmission electron microscopy (HRTEM) reveals LLTOs have complex microstructures: domains with different crystal orientations and periodicities are observed. The relationship between conductivity and microstructures (*e.g.*, density, domain size, atomistic structure, and composition of the domain boundaries)[70,80–89] were recently examined. The heat-treatment temperature affects the domain size, with a higher sintering temperature leading to a larger domain size and higher domain boundary conductivity (see Fig. 2b–f).[90] Scanning transmission electron microscopy (STEM) verified the existence of a large fraction of

90° domain boundaries, which was proven by DFT calculations to be detrimental to ion transfer.[89] Their elimination is predicted to increase the conductivity by about three orders of magnitude.[89] As shown in Fig. 2f and g, higher conductivity is also achieved when the Li concentration at the boundaries increases.

The origin of the poor grain boundary conductivity in LLTO was explored by Nan's group.[88] STEM/EELS analysis (Fig. 3a–g) revealed that dramatic structural deviations and chemical variations from the bulk framework can be observed at most grain boundaries. The grain boundary resembled more of a Ti–O binary phase, devoid of La^{3+} and more importantly, of the charge carrier Li^+; Fig. 3h schematically depicts the atomic configuration of the grain boundary and the Li site distribution. This mechanism explains previous observations that the introduction of Li ion conducting intergranular phases (Li_2O, LiF, Li_3BO_3, Li_4SiO_4, LLZO) may increase the grain boundary conductivity, if the new interface between the perovskite grains and the second phase does not act as a new barrier for Li migration.[84,91] Adding inert oxides, *e.g.* SiO_2 and Al_2O_3 as flux agents can also improve the conductivity of LLTO.[92–94] In the LLTO/SiO_2 composite, SiO_2 accommodates Li from LLTO grains to form an amorphous lithium silicate which greatly enhances the grain boundary conductivity.[92] Similarly, the addition of Al_2O_3 formed $LiAl_5O_8$ leads to a boost in both the bulk and grain boundary conductivity.[93]

2.1.1.2 Anti-perovskite type conductors. Inspired by high temperature ion-conducting perovskites such as (Na, K)MgF_3,[95,96] $KZnF_3$,[95,96] and $CsPbF_3$,[97] a new and promising family of "structurally-inverted" anti-perovskites, Li_3OX (X = Cl^-, Br^-, I^-, or a mixture of halides), was reported.[47,60,98] The anti-perovskite compounds have the same space group and similar structure as conventional perovskites (cubic, $Pm\bar{3}m$) but with inverted cation and anion sublattices and, hence, charges. In one representation of the Li_3OX anti-perovskites, X^- ions occupy the corner sites of the cube, O^{2-} ions occupy the body-centered site, and Li-ions form octahedra around the oxygen (Fig. 4a).[60] As noted by Ceder's group, this arrangement of Li ions in a bcc sublattice is optimal for fast ion conduction.[99] A conductivity of 8.5×10^{-5} S cm^{-1} (ref. 47) is exhibited by Li_3OCl at room temperature.

The anti-perovskites can be structurally tailored through chemical substitution, either by replacing Cl^- with larger Br^- or I^- anions or by substituting divalent cations for Li, to give rise to an ion conductivity above 10^{-3} S cm^{-1}.[60,98,100] For example, the mixed halide compound $Li_3OCl_{0.5}Br_{0.5}$ presents an improved conductivity of 1.94×10^{-3} S cm^{-1}, (Fig. 4b).[47] Cation-substituted $Li_{3-2x}M_xOX$ glassy electrolytes (M = Ca, Mg, or Ba) were prepared by Braga *et al.*,[60] and an unusually high ion conductivity of 2.5×10^{-2} S cm^{-1} at 25 °C was reported for $Li_{3-2x}Ba_xClO$ (x = 0.005). We note, however, that these results have not yet been reproduced to our knowledge, due to incomplete information on the synthesis. It has also been reported that these materials exhibit low electronic conductivity (10^{-9}–10^{-7} S cm^{-1}),[60] an apparently wide electrochemical window (>5 V,[60,98,100] *i.e.*, beyond the oxidation of Cl^-), good thermal stabilities up to *ca.* 550 K,[47,60] and more importantly, stability against Li metal,[60] but they are highly sensitive to moisture.

The Li^+ ion transport mechanism in the anti-perovskites is also under intensive debate. Based on DFT calculations, Zhang *et al.*[98] and Emly *et al.*[100] found that anti-perovskites such as Li_3OCl, Li_3OBr, and their mixed compounds are thermodynamically metastable. A transition at ~150 °C was predicted,

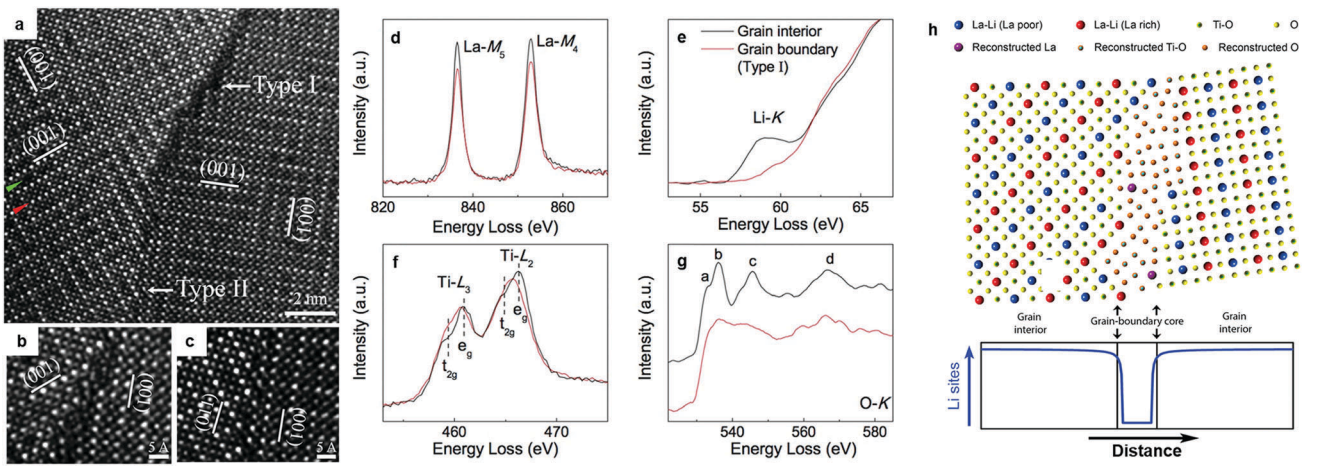

Fig. 3 (a) HAADF-STEM image of a GB exhibiting both dark- and normal-contrast regions, labelled as Type I and Type II, respectively. Within the grains, a row of atomic columns for a La-poor layer and one for a La-rich layer were indicated by green and red arrows on the left-hand side of the image, respectively. The (001) planes of the alternating La-rich/La-poor layers (arbitrarily designated as (001) planes in image) of different regions in the grain were marked to highlight the existence of nanodomains; (b) further magnified Type I GB feature; (c) further magnified Type II GB feature; (d) schematic of the atomic configuration of the Type I GB based on the HAADF-STEM images and EELS analysis, along with an illustration of the Li site distribution across the Type I GB. EELS data of (e) La-$M_{4,5}$, (f) Li-K, (g) Ti-$L_{2,3}$, and (h) O-K edges for the Type I GB and the bulk. The spectra were normalized to the integrated intensity of the Ti-$L_{2,3}$ edge. The normalized O-K edge of the bulk was shifted vertically for clarification.[88] Reproduced with permission from ref. 88. Copyright (2014), the Royal Society of Chemistry.

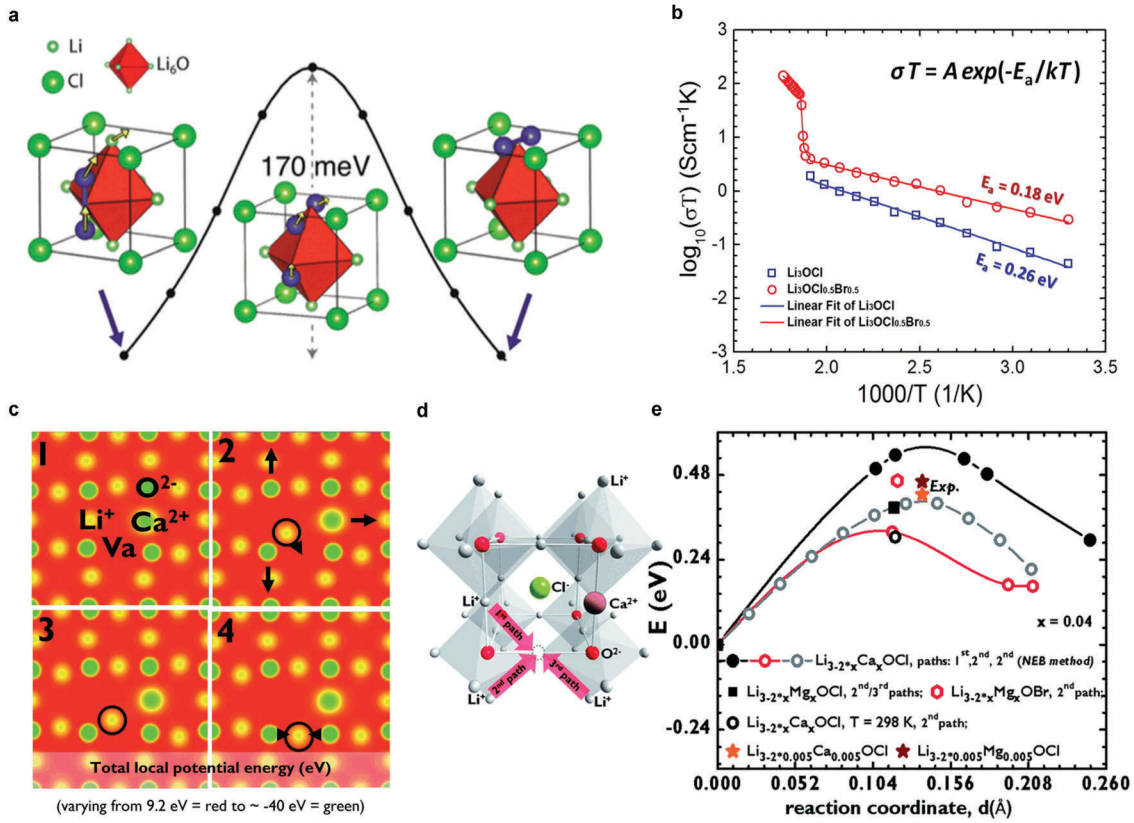

Fig. 4 (a) Low-barrier migration pathway for a neutral Li split interstitial in Li_3OCl. The barriers range from 145 to 175 meV depending on the charge state of the interstitial (neutral or +1) and host material (Li_3OBr or Li_3OCl);[47] (b) Arrhenius plots of $\log(\sigma T)$ *versus* $1/T$ for Li_3OCl and $Li_3OCl_{0.5}Br_{0.5}$ anti-perovskites, including E_a;[47] Reproduced with permission from ref. 47. Copyright (2012) American Chemical Society. (c) Li^+ diffusion and corresponding lattice dynamics, showing how the lattice adjusts during diffusion from 1 → 4; (d) alternative representation of the crystal structure of Li_3OCl highlighting the formation of a vacancy and three different paths for Li^+ diffusion upon Ca^{2+}-doping; (e) activation energies for different paths in (d), dopants and temperatures calculated by DFT-GGA and the Nudged Elastic Band (NEB) method compared with the experimental values obtained in the solid-like (Arrhenius) regime for $Li_{3-2x0.005}M_{0.005}OCl$ (M = Ca, Mg, Ba).[60] Elastic Band (NEB) method compared with the experimental values obtained in the solid-like (Arrhenius) regime for $Li_{3-2x0.005}M_{0.005}OCl$ (M = Ca, Mg, Ba).[60] Reproduced with permission from ref. 60. Copyright (2014), The Royal Society of Chemistry.

which was later deduced to be the glass transition. MD simulations[98] showed that anti-perovskites with perfect crystal structures are poor Li-ion conductors whereas Li vacancies and structural disorder promote Li-ion diffusion by reducing activation energy barriers. Emly *et al.*[100] proposed a collective hop-migration mechanism involving Li interstitial dumbbells with a barrier of only 0.17 eV (Fig. 4a), which was approximately 50% lower than that of vacancy driven migration. However, the high ion conductivity of lithium anti-perovskites could not be explained by this mechanism, because of the high formation energy of Li interstitial defects.[100] Later, Mouta *et al.*[101] employed classical atomistic simulation computations to calculate the concentration of Li vacancies and interstitials in Li_3OCl. Vacancies created by Schottky defects were predicted to be the charge carriers in Li_3OCl, since the concentration of interstitials (*i.e.*, Frenkel defects) was 6 orders of magnitude lower due to the very high energy required for their formation. Although the vacancy migration energy (0.30 eV, above room temperature) is larger than that driven by interstitial migration (0.133 eV), the former mechanism likely dominates ion conduction because of the significantly higher concentration of vacancies. However, in LiCl-deficient materials, the opposite was proposed to be likely true due to charge compensating mechanisms. DFT calculations were also performed to understand the role of aliovalent cation doping. Four snapshots of the Ca-doped structure during Li hopping suggest that the lattice dynamics cause further disorder (Fig. 4c). Doping with higher valent cations, *i.e.*, Ca^{2+}, Mg^{2+}, Ba^{2+}, creates Li vacancies in the cation sublattice and lowers the activation energy for Li ion conduction (Fig. 4d and e).[60] The deleterious role of resistive grain boundaries on the ion conductivity of polycrystalline Li_3OCl is suggested in a recent theoretical study (namely, the grain boundaries exhibit about one order of magnitude lower conductivity than the bulk).[102]

Recently, Li *et al.*[103] suggested that the as-prepared "Li_3OX" might be Li_2OHX rather Li_3OX. They reported that replacing some of the OH^- by F^- was possible. The obtained $Li_2(OH)_{0.9}F_{0.1}Cl$ was claimed to be stable on contact with Li metal with an apparent electrochemical window extending to 9 V *versus* Li^+/Li.[103] In addition, Braga *et al.*[104,105] reported that the existence

of H^+ was beneficial for the formation of an amorphous glassy phase, and a very high ion conductivity of more than 10^{-2} S cm^{-1} was reported – again the synthesis was not well described, and reproduction of the results is required.

2.1.1.3 NaSICON-type conductors. NaSICON (Na Super Ion CONductors) type electrolytes with the general formula $Na_{1+x}Zr_2Si_{2-x}P_xO_{12}$ ($0 \leq x \leq 3$) were first reported in 1976 by Goodenough and Hong.[106,107] They are derived from $NaZr_2(PO_4)_3$ by partial substitution of Si for P with excess Na to balance the negative charge. Their Li analogues, $LiM_2(PO_4)_3$ (M = Zr, Ti, Hf, Ge, or Sn),[108–117] are effectively isostructural.

The NaSICON framework is constituted by a rigid $M_2(PO_4)^{3-}$ skeleton, which is linked by MO_6 octahedra and PO_4 tetrahedra sharing O atoms (Fig. 5a).[118] For the $LiM_2(PO_4)_3$ (M = Ti, Ge) series, rhombohedral symmetry ($R\bar{3}c$) was confirmed using X-ray and neutron diffraction,[112,113] while for compositions with larger tetravalent cations such as $LiM_2(PO_4)_3$ (M = Zr, Hf, or Sn), a triclinic phase ($C\bar{1}$) of lower symmetry – induced by the displacement of Li ions – was also reported at low temperature.[114–116] In the rhombohedral phase, two crystallographic sites are possible for Li ions: M_1 (6b) sites, surrounded by six oxygens, and M_2 (18e) sites, which are located between two M_1 positions with 10-fold oxygen coordination. In triclinic phases, the structural distortion drives Li cations to the more stable intermediate M_{12} sites, which are located midway between M_1 and M_2 sites in 4-fold-oxygen coordination.[115,116]

Among the widely studied $LiM_2(PO_4)_3$ (M = Zr, Ge, Ti, or Hf) materials, $LiTi_2(PO_4)_3$ offers the most suitable lattice size for Li ion conduction.[119] However, $LiTi_2(PO_4)_3$ pellets obtained by a conventional sintering process showed very high porosity (34%).[120] Even the relative densities of hot-pressed ceramics were only ~95%, resulting in a low room temperature conductivity of 2×10^{-7} S cm^{-1}.[121] The partial substitution of Ti^{4+}

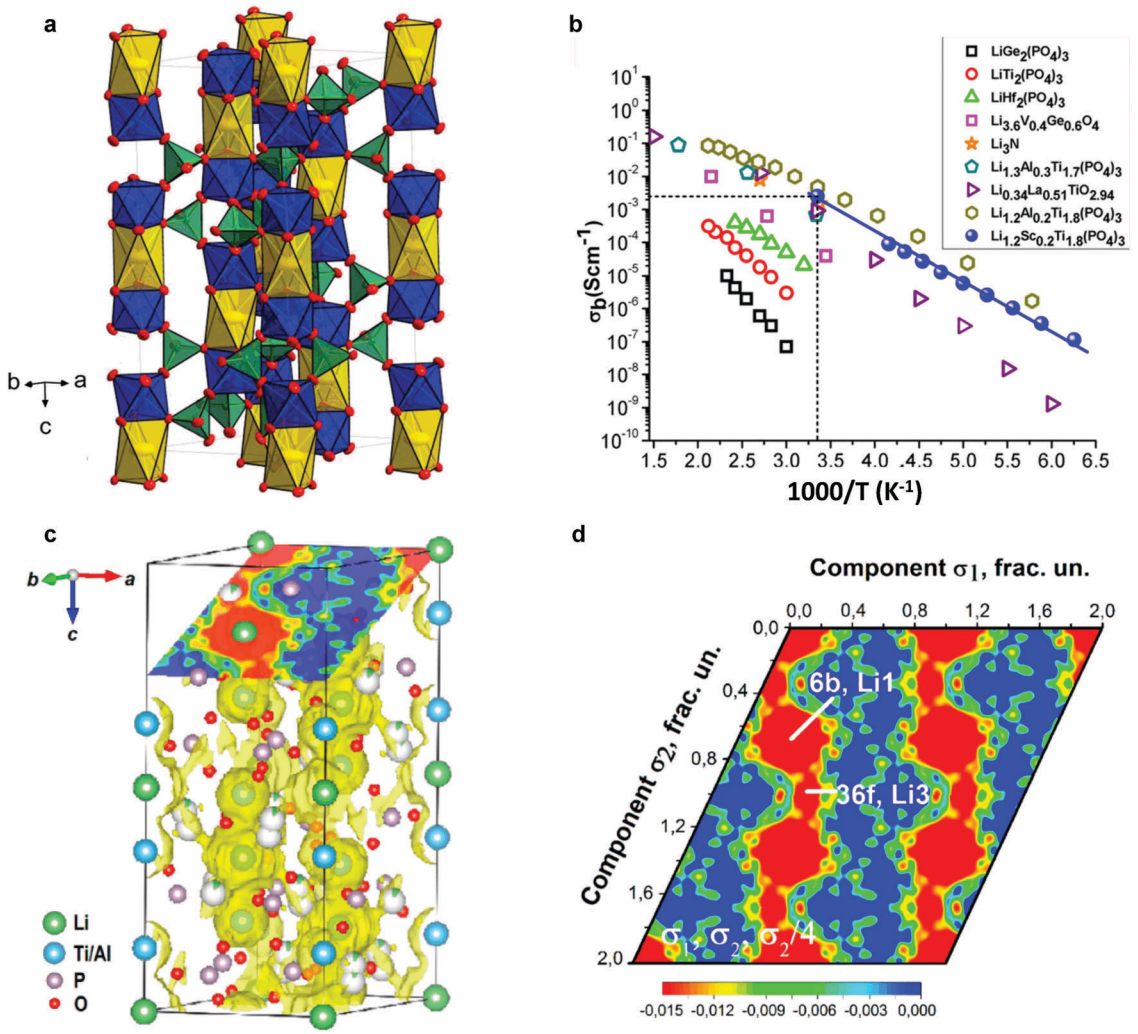

Fig. 5 (a) Unit cell (space group $R\bar{3}c$) of $LiTi_2(PO_4)_3$. Yellow elongated octahedra (M_1/6b) are occupied by Li^+; blue octahedra (12c) are occupied by Ti^{4+}; and green tetrahedra are occupied by P^{5+} (18e); O^{2-} is located at the corners of the polyhedra (small red circles, two Wyckoff positions 36f).[118] (b) Ion conductivity of NaSICON structured Li ion solid electrolytes.[134] (c) MEM-reconstructed negative nuclear density maps.[52] (d) Sections of bond-valence mismatch and negative nuclear densities $Li_{1.3}Al_{0.3}Ti_{1.7}(PO_4)_3$.[52] Reproduced with permission from ref. 52, 118, 134. Copyright (2016, 2017) American Chemical Society.

by trivalent cations, such as Al^{3+}, Sc^{3+}, Ga^{3+}, Fe^{3+}, In^{3+}, and Cr^{3+} in $Li_{1+x}R_xTi_{2-x}(PO_4)_3$ materials, improves ion conductivity.[122–131] In particular, a high lithium conductivity at room temperature, 7×10^{-4} S cm^{-1} was reported in the case of $Li_{1.3}R_{0.3}Ti_{1.7}(PO_4)_3$ (R = Al^{3+}), abbreviated as LATP.[123] Similar effects caused by trivalent cation doping at M sites are also observed in the $LiGe_2(PO_4)_3$ phase and an ion conductivity of 2.4×10^{-4} S cm^{-1} can be achieved in well-known $Li_{1+x}Al_xGe_{2-x}(PO_4)_3$, abbreviated as LAGP.[132] The incorporation of trivalent cations influences the conductivity by increasing the concentration of mobile ions in the framework, as well as by invoking additional interstitial migration with lower activation energy.[133]

Besides the bulk conductivity, the grain boundary conductivity was also augmented by the greater densification of the pellet allowed by R^{3+} substitution. The conductivities of these compositions are shown in Fig. 5b.[134]

In $LiTi_2(PO_4)_3$, Li ions tend to preferentially occupy the M_1 sites (0, 0, 0) in the space group $R\bar{3}c$,[113,114] as recently confirmed by single crystal X-ray diffraction analysis.[118] A combination of NPD and synchrotron-based high-resolution powder diffraction revealed that the partial replacement of Ti^{4+} by Al^{3+} in LATP causes Li ions to occupy an additional interstitial position, a Li_3 site (36f), that is located between two adjacent Li1 sites. Li diffusion preferentially occurs between two adjacent Li positions through this Li_3 site, forming a Li1–Li3–Li3–Li1 zigzag chains in three dimensions (Fig. 5c and d).[52]

Another effective strategy to improve the conductivity of $LiM_2(PO_4)_3$ is by addition of a second lithium compound such as Li_2O,[119,135] $LiNO_3$,[136] Li_3PO_4,[137] $Li_4P_2O_7$,[135] Li_3BO_3[137] or LiF,[138] which acts as a flux at grain boundaries, generating higher density ceramics with improved conductivities. For example, when 20% Li_2O is incorporated in $LiTi_2(PO_4)_3$, the conductivity can be improved to 5×10^{-4} S cm^{-1}.[119,135]

Superionic conducting glass-ceramics (lithium–aluminum–titanium–phosphate (LATP) and lithium–aluminum–germanium–phosphate (LAGP)) were first reported by the Ohara company[139,140] and subsequently by other researchers.[141–146] An extremely high conductivity of 5.08×10^{-3} S cm^{-1} at 27 °C, much higher than that of the crystalline analogue, can be obtained by optimizing the heat-treatment conditions.[144] The presence of dielectric phases (Li_2O and $AlPO_4$) – unavoidable by-products that form during the sintering process of these glass-ceramics which mainly segregate at the grain boundary – have been detected and identified.[141–144,146] $AlPO_4$ could either block or increase the conductivity, depending on its concentration and crystallite size.[145]

2.1.1.4 Garnet type conductors. Ideal garnets have the general formula $A_3B_2M_3O_{12}$ (A = Ca^{2+}, Mg^{2+}, or Fe^{2+}; B = Al^{3+}, Cr^{3+}, Fe^{3+}, or Ga^{3+}; M = Si^{4+} or Ge^{4+}) and crystallize in the space group $Ia\bar{3}d$, in which A, B, and M are filled with eight-, six-, and four-coordinated cation sites in a 3 : 2 : 3 ratio, respectively. Li garnets of the general formula $Li_3Ln_3Te_2O_{12}$ (Ln = Y^{3+}, Pr^{3+}, Nd^{3+}, or Sm^{3+}–Lu^{3+}) follow this stoichiometry, with Ln and Te occupying the eight- and six-coordinated sites, respectively, and Li fully occupying tetrahedral sites (24d). Li-ion conducting garnets attracted significant interest after the first report of $Li_5La_3M_2O_{12}$ (M = Nb or Ta) by Thangadurai *et al.*,[147] in which an ion conductivity of $\sim 10^{-6}$ S cm^{-1} was achieved at 25 °C. The Ta members were reported to be surprisingly chemically stable to reaction with molten Li or moisture, and a wide electrochemical window was reported.[147] Subsequently, the conductivity of $Li_5La_3Nb_2O_{12}$ was optimized by partial substitution of La^{3+} by K^+ (ref. 148) and partial substitution of Nb^{5+} with either In^{3+} (ref. 148) or Y^{3+}.[149] As the tetrahedral M site can not accommodate all five Li cations, excess Li cations occupy the six-coordinate sites (the octahedral or trigonal prismatic sites), which are empty in the original garnet structure. Garnets containing five to seven Li atoms per formula unit are referred to as Li-stuffed, or Li-rich garnets.

Thangadurai *et al.* demonstrated that partial substitution at the La site by divalent alkaline earth ions generates a new class of garnet-like structures, $Li_6ALa_2M_2O_{12}$ (A = Ca^{2+}, Sr^{2+}, or Ba^{2+}; M = Nb^{5+} or Ta^{5+}),[150,151] among which $Li_6BaLa_2Ta_2O_{12}$ exhibited the highest conductivity of 4×10^{-5} S cm^{-1} at 22 °C and the lowest activation energy of 0.4 eV.[151] Aside from the niobate/tantalate garnets mentioned above, antimony-containing garnets $Li_5Ln_3Sb_2O_{12}$ (Ln = La, Pr, Nd, or Sm). were also investigated.[152,153] Moreover, M can be replaced by tetravalent cations to generate Li-rich garnets such as $Li_7La_3M_2O_{12}$ (M = Zr, Sn, or Hf).[154–157]

Within the garnet family, cubic $Li_7La_3Zr_2O_{12}$ (LLZO), first reported by Murugan *et al.*,[154] is considered the most attractive candidate for solid electrolytes owing to its high room temperature conductivity ($>10^{-4}$ S cm^{-1}), high chemical stability against Li, and a wide electrochemical potential window. It is moisture-sensitive, however. In cubic LLZO (space group: $Ia\bar{3}d$), Li ions are disordered over the tetrahedral 24d Li(1), octahedral 48g and 96h Li(2) sites (Fig. 6a).[158] LLZO also exists in a more thermodynamically stable tetragonal phase ($I4_1/acd$). It exhibits a conductivity that is one to two orders of magnitude lower than that of the cubic phase because of the fully ordered arrangement of Li ions at the tetrahedral 8a sites and octahedral 16f and 32g sites.[159] Therefore, major efforts have been focused on using substitution strategies to stabilize the highly conductive cubic phase through a reduction in Li content and/or an increase in the Li vacancy concentration. The substituent Al^{3+} – either intentionally added or unintentionally introduced from alumina crucibles – was first found to be effective.[49,160–163] Stabilization originates from the increased Li sublattice disorder owing to Li vacancies created *via* aliovalent substitution of Li^+ by Al^{3+}.[164] However, the site preference (the 24d tetrahedral or 48g/96h octahedral Li sites) for Al^{3+} ions in the framework remains ambiguous.[49,160–163,165,166] Düvel *et al.*[49] found that with an increase in Al content (above 0.2–0.24 moles per LLZO formula unit), Al^{3+} ions occupy non-Li cation sites. The addition of Al^{3+} or Si^{4+} aids the sintering process, leading to a densification of the obtained ceramics and an improvement in the Li ion conductivity (6.8×10^{-4} S cm^{-1}).[167,168] This was attributed to an effective reduction of grain boundary resistance through the formation of nano-crystalline $LiAlSiO_4$ in the grain boundaries.[168]

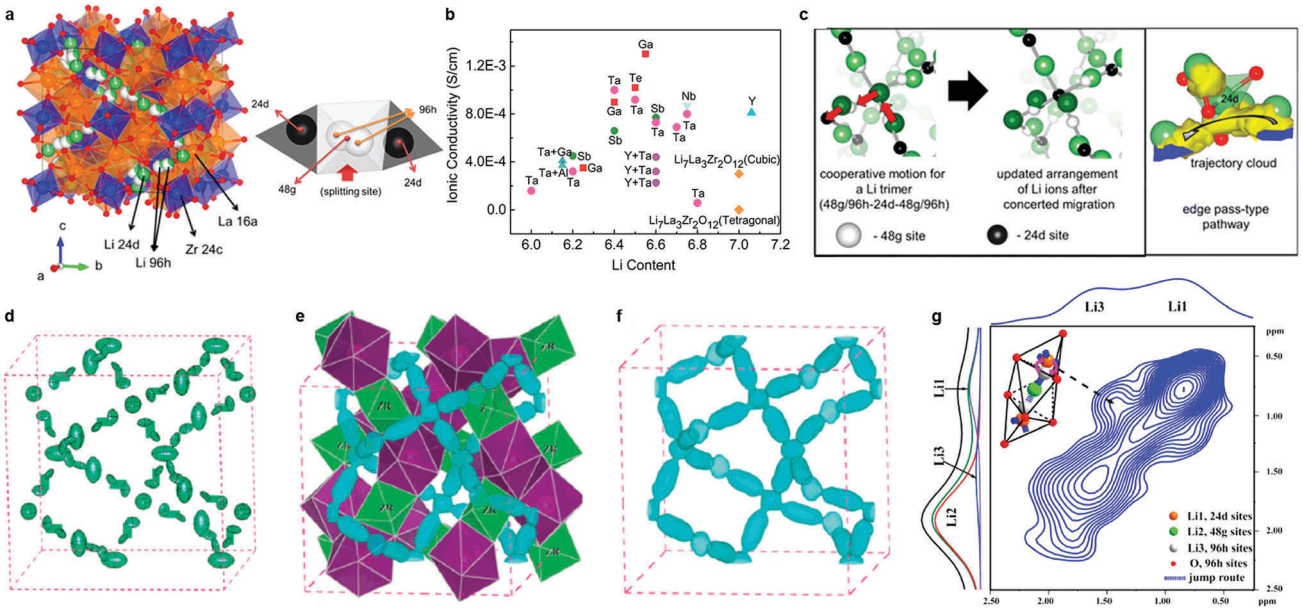

Fig. 6 (a) Crystal structure of cubic-type LLZO ($Ia\bar{3}d$), and Li environment. The center of the tetrahedral Li_1 sites are the 24d sites, and the center of the octahedral Li_2 sites are the 48g sites. Meanwhile, positions slightly displaced from the 48g sites and near the face (but still inside the Li_2 octahedron) are the 96h sites.[158] (b) Conductivities of doped LLZO.[147–151,154,156,157,168,169,171,175–178,181,183–186] (c) Snapshots of Li ions' mobility from the MD simulation and enlarged view of the selected Li atoms showing the tetrahedral edge pass according to the trajectory cloud.[158] (d) Anisotropic harmonic lithium vibrations in c-$^{7}Li_7La_3Zr_2O_{12}$ shown as green thermal ellipsoids obtained from Rietveld analysis of room-temperature neutron diffraction data.[197] (e) Nuclear distribution of lithium calculated by MEM from neutron powder diffraction data obtained at 600 °C; three-dimensional ^{7}Li nuclear-density data shown as blue contours (equivalue 0.15 fm Å^{-3} of the negative portion of the coherent nuclear scattering density distribution). The green octahedra represent ZrO_6 and the purple dodecahedra represent LaO_8 units.[197] Reproduced with permission from ref. 197. Copyright (2012), The Royal Society of Chemistry. (f) The distribution of lithium calculated by MEM from neutron powder diffraction data obtained at 400 and 600 °C, respectively, and three-dimensional Li nuclear-density data shown as blue contours (equivalue 0.15 fm Å^{-3} of the negative portion of the coherent nuclear scattering density distribution).[197] (g) ^{6}Li–^{6}Li exchange spectra of $Li_{7-2x-3y}Al_yLa_3Zr_{2-x}W_xO_{12}$ (x = 0.5) sintered at 1150 °C for 12 h.[179] Reproduced with permission from ref. 158, 179. Copyright (2013, 2015) American Chemical Society.

The aliovalent substitution of Li^+ by Ga^{3+} (ref. 169–172) has the same stabilizing effect. By sintering the ceramic in a dry O_2 atmosphere, an optimum conductivity of 1.3 × 10^{-3} S cm^{-1} (ref. 171) at 24 °C was achieved, although the Ga^{3+} distribution in the LLZO lattice was difficult to determine.[171,173,174] Other supervalent dopants for Zr^{4+} sites (Sb^{5+}, Nb^{5+}, Ta^{5+}, Te^{6+}, and W^{6+} (ref. 175–179)) have also been employed, resulting in some remarkable improvements in conductivity. The highest conductivities of *ca.* 1.0 × 10^{-3} S cm^{-1} at room temperature were achieved for Ta-doping,[177] and Te-doping.[178] Lower conductivity was reported for simultaneous substitution of Al at Li^+ site, Y^{3+}, Ba^{2+} at La^{3+} site, and/or Ta^{5+}, Sb^{5+}, Te^{6+} at Zr^{4+} sites, however.[180–182] The conductivities of these compounds and other garnet oxides are listed in Table 1 and Fig. 6b.[147–151,154,156,157,168,169,171,175–178,181,183–186] While it was believed that "accidental" Al^{3+} substitution on the Li^+ site from crucible contamination was actually responsible for stabilizing the cubic phase in many cases,[163,187] recently it was confirmed that Ta-substituted cubic LLZO exhibits high ion conductivity in the absence of any Al^{3+}.[188,189] Approximately 0.4–0.5 Li vacancies per formula unit are required to stabilize the cubic polymorph of LLZO.[188,189]

Many X-ray and neutron diffraction studies have been geared towards determining the crystal structure and the Li environment in garnet type electrolytes. However, the phase stability and the ion transport mechanism are still controversial,[190–192] due to the limitations of these techniques in determining the exact Li occupancy on the tetrahedral and octahedral sites. Using neutron diffraction, Cussen *et al.*[193] confirmed that $Li_5La_3M_2O_{12}$ (M = Nb or Ta) crystallized in the $Ia\bar{3}d$ space group with Li distributed over the tetrahedral and distorted octahedral sites. They also investigated the relationship between ion conductivity and Li site occupation in $Li_3Ln_3Te_2O_{12}$ (Ln = Y, Pr, Nd, or Sm–Lu).[186] Li ions were found to exclusively occupy the tetrahedral (24d) sites. Given that $Li_3Nd_3Te_2O_{12}$ exhibits a extremely low conductivity ($\sim 10^{-5}$ S cm^{-1} at 600 °C) and very high activation energy (1.22 eV), it was deduced that the Li ions at the tetrahedral sites play no direct role in facile ion mobility. Later, the exact location and dynamics of Li ions in $Li_5La_3Nb_2O_{12}$ were investigated using solid-state nuclear magnetic resonance (NMR).[194] Indeed, the octahedrally coordinated Li cations were revealed to be the only mobile species. Neutron diffraction studies were also performed on $Li_{5+x}Ba_xLa_{3-x}Ta_2O_{12}$ ($0 < x < 1.6$) by Cussen *et al.*[195] They found that as the Li content increases, the tetrahedral site occupancy is reduced whereas the fraction of Li in octahedral site increases. This results in a shift in the Li environment from primarily tetrahedral (at $x = 0$) to octahedral (at $x = 1.6$). Since the tetrahedra and octahedra are connected by a shared face, simultaneous occupation of adjacent polyhedral sites inevitably leads to reduced Li–Li distances and displacement of Li away from the shared faces. The electrostatic

Table 1 Conductivity and activation energy of garnet-type electrolytes[147–151,154,156,157,168,169,171,175–178,181,183–186]

Composition	Conductivity (S cm^{-1})	Temperature (°C)	E_a (eV)	Ref.
$Li_3Nd_3Te_2O_{12}$ (850 °C)	1×10^{-5}	600	1.22	186
$Li_5La_3Nb_2O_{12}$ (950 °C)	1×10^{-5}	22	0.43	147
$Li_5La_3Ta_2O_{12}$ (950 °C)	1.2×10^{-6}	25	0.56	147
$Li_{5.5}La_{2.75}K_{0.25}Nb_2O_{12}$ (950 °C)	6.0×10^{-5}	50	0.49	148
$Li_{5.5}La_3Nb_{1.75}In_{0.25}O_{12}$ (950 °C)	1.8×10^{-4}	50	0.51	148
$Li_{6.5}La_3Nb_{1.25}Y_{0.75}O_{12}$ (1000 °C)	10^{-4}	24	—	149
$Li_6La_3Nb_{1.5}Y_{0.5}O_{12}$ (1000 °C)	10^{-4}	24	—	149
$Li_6CaLa_2Nb_2O_{12}$ (900 °C)	1.6×10^{-6}	22	0.55	150
$Li_6SrLa_2Nb_2O_{12}$ (900 °C)	4.2×10^{-6}	22	0.5	150
$Li_6BaLa_2Nb_2O_{12}$ (900 °C)	6.0×10^{-6}	22	0.44	150
$Li_6SrLa_2Ta_2O_{12}$ (900 °C)	7.0×10^{-6}	22	0.5	151
$Li_6BaLa_2Ta_2O_{12}$ (900 °C)	4×10^{-5}	22	0.40	151
$Li_7La_3Zr_2O_{12}$ (1230 °C, cubic)	3.0×10^{-4}	25	0.31	154
$Li_7La_3Zr_2O_{12}$ (980 °C, tetragonal)	1.63×10^{-6}	27	0.54	159
$Li_7La_3Sn_2O_{12}$ (900 °C, tetragonal)	2.6×10^{-8}	85	0.79	156
$Li_7La_3Hf_2O_{12}$ (1000 °C, tetragonal)	3.17×10^{-7}	27	0.53	157
$Li_7La_3Zr_2O_{12}$ (1.7 wt% Al, 0.1 wt% Si, 1125 °C)	6.8×10^{-4}	25	—	168
$Li_7La_3Zr_{1.89}Al_{0.15}O_{12}$ (1150 °C)	3.4×10^{-4}	25	0.33	183
$Li_{7.06}La_3Y_{0.06}Zr_{1.94}O_{12}$ (1200 °C)	8.1×10^{-4}	25	0.26	184
$Li_{6.25}La_3Zr_2Ga_{0.25}O_{12}$	3.5×10^{-4}	RT	—	169
$Li_{6.55}La_3Zr_2Ga_{0.15}O_{12}$ (1085 °C, O_2)	1.3×10^{-3}	24	0.30	171
$Li_{6.4}La_3Zr_2Ga_{0.2}O_{12}$ (1085 °C)	9.0×10^{-4}	24	—	171
$Li_{6.8}La_3Zr_{1.8}Sb_{0.2}O_{12}$ (1100 °C)	5.9×10^{-5}	30	0.39	175
$Li_{6.6}La_3Zr_{1.6}Sb_{0.4}O_{12}$ (1100 °C)	7.7×10^{-4}	30	0.34	175
$Li_{6.4}La_3Zr_{1.4}Sb_{0.6}O_{12}$ (1100 °C)	6.6×10^{-4}	30	0.36	175
$Li_{6.2}La_3Zr_{1.2}Sb_{0.8}O_{12}$ (1100 °C)	4.5×10^{-4}	30	0.37	175
$Li_6La_3ZrSbO_{12}$ (1100 °C)	2.6×10^{-4}	30	0.38	175
$Li_{6.75}La_3Zr_{1.75}Nb_{0.25}O_{12}$ (1200 °C)	8.0×10^{-4}	25	0.31	176
$Li_{6.8}La_3Zr_{1.8}Ta_{0.2}O_{12}$ (1230 °C)	2.8×10^{-4}	25	—	177
$Li_{6.6}La_3Zr_{1.6}Ta_{0.4}O_{12}$ (1230 °C)	7.3×10^{-4}	25	—	177
$Li_{6.5}La_3Zr_{1.5}Ta_{0.5}O_{12}$ (1230 °C)	9.2×10^{-4}	25	—	177
$Li_{6.4}La_3Zr_{1.4}Ta_{0.6}O_{12}$ (1230 °C)	1.0×10^{-3}	25	0.35	177
$Li_{6.2}La_3Zr_{1.2}Ta_{0.8}O_{12}$ (1230 °C)	3.2×10^{-4}	25	—	177
$Li_6La_3ZrTaO_{12}$ (1230 °C)	1.6×10^{-4}	25	—	177
$Li_{6.7}La_3Zr_{1.7}Ta_{0.3}O_{12}$ (900 °C)	6.9×10^{-4}	25	0.36	177
$Li_{6.75}La_3Zr_{1.75}Ta_{0.25}O_{12}$ (1000 °C)	8.7×10^{-4}	25	0.22	185
$Li_{6.5}La_3Zr_{1.75}Te_{0.25}O_{12}$ (1100 °C)	1.02×10^{-3}	30	0.39	178
$Li_{6.15}La_3Zr_{1.75}Ta_{0.25}Al_{0.2}O_{12}$ (1000 °C)	3.7×10^{-4}	25	0.30	185
$Li_{6.15}La_3Zr_{1.75}Ta_{0.25}Ga_{0.2}O_{12}$ (1000 °C)	4.1×10^{-4}	25	0.27	185
$Li_{6.6}La_{2.875}Y_{0.125}Zr_{1.6}Ta_{0.4}O_{12}$ (1200 °C)	3.17×10^{-4}	27	0.35	181
$Li_{6.6}La_{2.75}Y_{0.25}Zr_{1.6}Ta_{0.4}O_{12}$ (1200 °C)	4.36×10^{-4}	27	0.34	181
$Li_{6.6}La_{2.5}Y_{0.5}Zr_{1.6}Ta_{0.4}O_{12}$ (1200 °C)	2.26×10^{-4}	27	0.39	181

repulsion associated with this arrangement leads to the high mobility of Li^+ in these materials.

Several simulations combined with experiments have been performed to explore the Li ion diffusion mechanism. Using the nudged elastic band (NEB) method, Xu *et al.* found that in the Li-stuffed garnet, Li^+ ions can migrate between tetrahedral and octahedral sites,[196] although only limited insights can be gained from NEB since it reflects the local migration behavior. On the other hand, MD simulations evaluate the Li ion hopping events, and quantitatively assess the collective migration behavior. As shown in Fig. 6b, MD simulations indicate a concerted migration mechanism in cubic LLZO, indicative of a complex cooperative mechanism.[158] The Li diffusion pathways in LLZO and the evolution of Li motion with temperature were also investigated by high-temperature neutron diffraction techniques combined with the maximum-entropy method (MEM).[197] Temperature-driven dynamic Li-ion displacements exhibited a 3D diffusion pathway constituted by an interlocking network of 24d–96h–48g–96h–24d site segments (Fig. 6d–f), indicating that Li ions diffuse through the tetrahedral 24d sites, consistent with the results of Xu *et al.*[196] NMR results[179] also show evidence of ion exchange between the 24d and 96h sites (Fig. 6g) and the bulk conductivity is found to be limited by the Li mobility at the 24d sites.

2.1.2 Sulfide based lithium ion conductors

2.1.2.1 Thio-LiSICONs. Thio-LiSICONs were first developed by Kanno *et al.*[42,61] by replacing oxide ions in LiSICON with larger and more polarizable S^{2-} anions. The high polarizability of S^{2-} weakens interactions of Li^+ with the anionic sub-lattice, leading to higher Li-ion conductivity in sulfides than in their oxide analogues. Sulfide electrolytes are also highly ductile and exhibit a lower grain boundary resistance than oxides. As a consequence, excellent contact with electrode materials can be realized by simple cold-pressing, making the fabrication of bulk solid-state batteries more convenient.[198,199]

The thio-LiSICON family contains a very wide range of solid solutions with the general formula $Li_xM_{1-y}M'_yS_4$ (M = Si or Ge; M′ = P, Al, Zn, Ga, or Sb), that exhibit ion conductivities ranging from 10^{-7}–10^{-3} S cm^{-1},[61,200,201] amongst which $Li_{4-x}Ge_{1-x}P_xS_4$ exhibits the highest conductivity (2.2×10^{-3} S cm^{-1}).[42]

Table 2 Conductivity of thio-LiSICON electrolytes and other typical sulfide crystallites[45,46,61,63,205–209]

Composition	Conductivity (S cm^{-1})	Temperature (°C)	Ref.
Li_4GeS_4	2.0×10^{-7}	25	61
$Li_{3.9}Zn_{0.05}GeS_4$	3.0×10^{-7}	25	61
$Li_{4.275}Ge_{0.61}Ga_{0.25}S_4$	6.5×10^{-5}	25	61
$Li_{3.25}Ge_{0.25}P_{0.75}S_4$	2.2×10^{-3}	25	42
$Li_{3.4}Si_{0.4}P_{0.6}S_4$	6.4×10^{-4}	25	200
$Li_{4.8}Si_{0.2}Al_{0.8}S_4$	2.3×10^{-7}	25	200
$Li_{2.2}Zn_{0.1}Zr_{0.9}S_3$	1.2×10^{-4}	30	202
γ-Li_3PS_4 (crystal)	3.0×10^{-7}	25	203
β-Li_3PS_4 (nanoporous)	1.6×10^{-4}	25	201
Li_2SiS_3	2.0×10^{-6}	25	204
Li_4SiS_4	5.0×10^{-8}	25	204
$Li_6P_2S_4$	1.6×10^{-10}	25	207
$Li_7P_3S_{11}$	3.2×10^{-3}	25	205
Li_4SnS_4	7.0×10^{-5}	20	206
$Li_{10}GeP_2S_{12}$	1.2×10^{-2}	27	45
$Li_{10}SnP_2S_{12}$	4.0×10^{-3}	27	63
$Li_{10}SiP_2S_{12}$	2.3×10^{-3}	27	208
$Li_{10}Ge_{0.95}Si_{0.05}P_2S_{12}$	8.6×10^{-3}	25	209
$Li_{9.54}Si_{1.74}P_{1.44}S_{11.7}Cl_{0.3}$	2.5×10^{-2}	25	46

The conductivities of thio-LiSICON electrolytes and other typical crystalline sulfides such as Li_3PS_4, Li_4SiS_4, Li_4SnS_4, Li_2SiS_3, $Li_4P_2S_6$ as well as meta-stable $Li_7P_3S_{11}$ are listed in Table 2.[46,201–209] The role of the different structural building units ($P_2S_7^{4-}$ or PS_4^{3-}) in the conductivity of glass and crystalline lithium thiophosphates (LPS) phases has recently been clarified by monitoring *in situ* crystallization and phase evolution in this class of material.[210,211] Glasses with only *ortho*-thiophosphate units show the highest lithium ion conductivity, the lowest activation energy and favorable thermal resistance towards decomposition, while glasses in which the major PS_4^{3-} building units are linked by P–S–P bonds cleave at elevated temperatures to form sulfur and $Li_4P_2S_6$, thereby losing their contribution to lithium ion conduction.

2.1.2.2 The LGPS family. In 2011, Kanno's group discovered a new sulfide – $Li_{10}GeP_2S_{12}$ (LGPS) – that exhibits an extremely high conductivity of 1.2×10^{-2} S cm^{-1},[45] which is comparable to or higher than that of liquid organic electrolytes currently used in commercially available Li-ion batteries. Unfortunately, $Li_{10}GeP_2S_{12}$ shows a limited electrochemical window,[212] and poor interfacial stability against Li metal.[213] In addition, the low abundance and high cost of Ge restricts its application in batteries. Substitutions of Ge^{4+} with Si^{4+} or Sn^{4+} (ref. 63, 208, 209, 214 and 215) generate $Li_{10}MP_2S_{12}$ (M = Si^{4+}, Sn^{4+}) (either experimentally (Sn^{4+}) or theoretically (Si)) and $Li_{10+\delta}M_{1+\delta}P_{2-\delta}S_{12}$ (M = Si^{4+}, Sn^{4+})[216] with high ion conductivity, which varied as a function of M, with the Si and Sn systems showing lower conductivity than Ge. While the substitution with smaller Si^{4+} leads to a lower conductivity due to narrower diffusion pathways, the structural reasons behind the reduction in conductivity upon moving from Ge^{4+} to larger Sn^{4+} were not well understood. The structure–property relationships governing this behavior was employed by Zeier's group[217] employing a combination of speed of sound measurements and electrochemical impedance spectroscopy (EIS). It was shown that increasing the Sn^{4+} fraction in $Li_{10}Ge_{1-x}Sn_xP_2S_{12}$ leads to a more tight structural bottleneck along the diffusion channels in the *z*-direction, and concurrent increase in the lattice softness, which causes stronger local ionic bonding interactions between Li^+ and S^{2-}, and therefore an increased activation barrier.[217] A different composition, $Li_{11}Si_2PS_{12}$, shows a conductivity of 2×10^{-2} S cm^{-1} at room temperature as inferred from NMR diffusivity data. This represents a very high value for solid Li ion conductors; however the phase can only be accessed under pressure.[215]

The tetragonal structure of LGPS (space group *P*42/*nmc* (137)) in Kanno's report[45] was determined from powder diffraction and Rietveld refinement. The reported framework is composed of GeS_4/PS_4 tetrahedra, LiS_4 tetrahedra and LiS_6 octahedra. The tetrahedrally coordinated Li1 (16h) and Li3 (8f) sites form a 1D tetrahedral chain along the *c*-axis while the octahedrally coordinated Li2 position between these chains was assumed to be inactive for ion conduction.[45] MD simulation performed by Mo *et al.*[11] supported this highly anisotropic diffusivity in the LGPS structure. Careful examination of the isosurface from long MD simulation by Adams *et al.*[218] suggested the existence of an additional site at (0, 0, 0.22) (marked as Li4, Fig. 7a and b). Single crystal structure analysis identified a similar Li4 site at (0, 0, 0.251(2)) with an occupancy of 0.81(7) and rather large anisotropic displacement parameters similar to the Li1 and Li3 positions.[219] The thermal ellipsoid of the Li4 site is aligned perpendicular to the *c*-axis, and provides an extra diffusion pathway connecting the channels along the *c*-axis formed by Li1 and Li3.[219] A recent neutron diffraction study combined with nuclear density maps verified the quasi-isotropic lithium diffusion in LGPS and three most prominent pathways for lithium transport, namely, along the ⟨001⟩ direction (Li3–[Li1–Li1]–Li3) and along ⟨110⟩ (*i.e.*, at *z* = 0, 1/4, 1/2, 3/4; Li4–[Li1–Li1]–Li4 and Li3–[Li2–Li2]–Li3, Fig. 7c and d) are identified.[220] This reconciles the theoretical findings by Adams *et al.*, namely the hops between the Li3 and Li2 pathways along the ⟨110⟩ direction significantly contribute to the overall conductivity (Fig. 7f), along with the previously identified lithium migration channels along the ⟨001⟩ direction (Fig. 7e).[218] Their calculations also suggested increasing occupancy in the Li4 site with increasing temperature (Fig. 7g) and its role in connecting Li4–Li1 thus enabling a 3D network for Li ion migration.[218]

Very recently, a remarkably high conductivity (2.5×10^{-2} S cm^{-1} at 25 °C) was reported again by Kanno's group[46] for a new sulfide material, $Li_{9.54}Si_{1.74}P_{1.44}S_{11.7}Cl_{0.3}$ (Fig. 8a and b) whose structure is related to LGPS. This is the highest value reported to date for Li ion conductors. The anisotropic thermal displacement and nuclear density distribution of Li suggest a three-dimensional (3D) migration pathway (Fig. 8c), in agreement with previous studies.[220] Another LGPS-related composition, $Li_{9.6}P_3S_{12}$,[46] exhibits a lower conductivity (1.2×10^{-3} S cm^{-1} at 25 °C), but was claimed to be stable in a window of 0–5 V. Both new compositions were not prepared in a phase-pure state, however, and contain significant fractions of other ion-conductive phases. Nonetheless, all-solid-state batteries using these new materials set a record in demonstrating high specific power and long cycle life.[46]

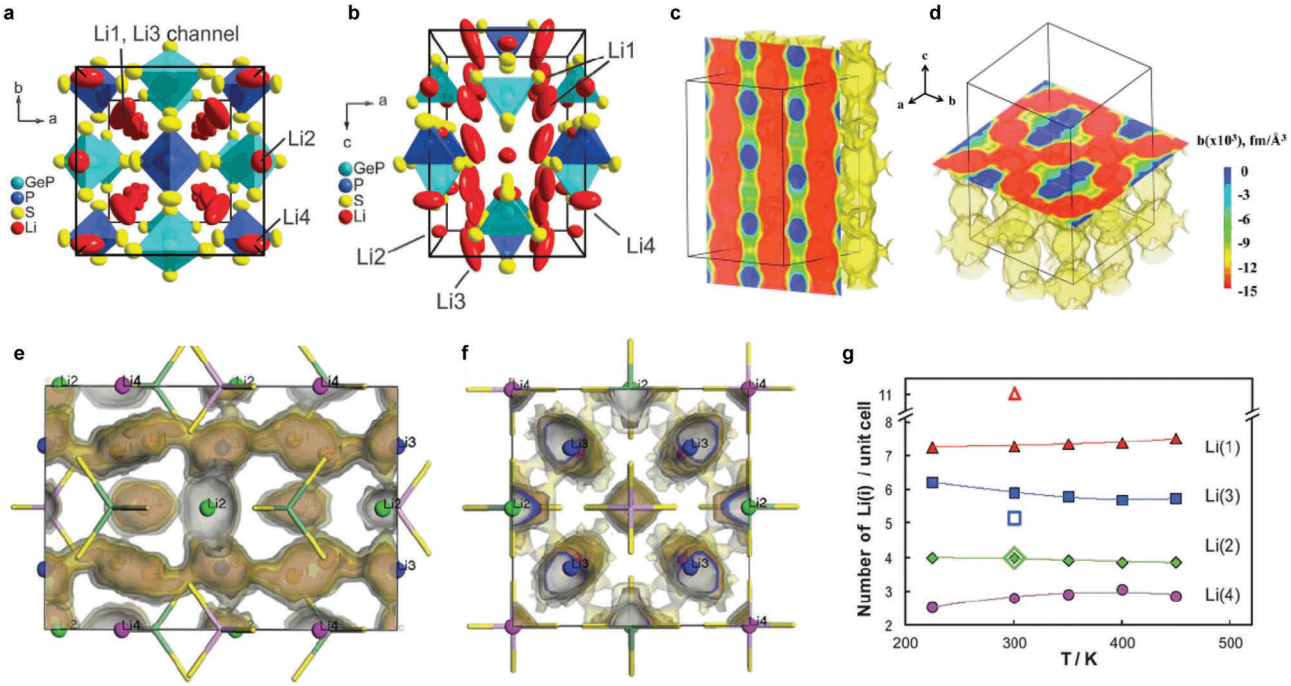

Fig. 7 (a and b) Unit cell of tetragonal $Li_{10}GeP_2S_{12}$ with thermal ellipsoids (p = 0.8);[219] Reproduced with permission from ref. 219. Copyright (2013) the Royal Society of Chemistry. (c) MEM reconstructed negative nuclear density maps in $Li_{10}GeP_2S_{12}$ (surface threshold −0.015 fm Å^{-3}, cell grid 256 × 256 × 512) and slices in (c) (011) and (d) (001) planes, respectively; (d) shows the diffusion tunnels within $Li_{10}GeP_2S_{12}$ along the ⟨001⟩ direction, whereas the Li distribution along ⟨110⟩ can be seen in (d);[220] Reproduced with permission from ref. 220. Copyright (2016) American Chemical Society. (e and f) Li distribution from a 10 ns *NVT* MD simulation of a 3 × 3 × 2 supercell at T = 300 K projected into a single unit cell (shown (e) along [100] and (f) along [001]). Regions of highest Li density (darkest isosurface) coincide with the 4 Li sites, the easiest path for transport (lighter isosurface) corresponds to the Li(3)–Li(1) channels along [001]. The lightest isosurface reveals a significant probability for hops Li(3)–Li(2) establishing a 3D network of pathways. With a lower probability, Li(4) sites are attached to this pathway network (not shown);[218] (g) temperature dependence of Li distribution on the four Li sites identified by MD simulations (filled symbols). The corresponding open symbols refer to the neutron refinements by Kanno's group,[45] who distributed the 20 Li per unit cell onto Li(1), Li(2) and Li(3) sites only.[218] Reproduced with permission from ref. 218. Copyright (2012) the Royal Society of Chemistry.

2.1.2.3 Argyrodite type. The addition of halides to thiophosphates can increase the conductivity of quasi-binary or quasi-ternary systems. Outstanding examples are the halogen-substituted argyrodites Li_6PS_5X (X = Cl, Br, I).[62] The "parent" argyrodite of Li_7PS_6 crystallizes both in a cubic high temperature (HT) phase and an orthorhombic low temperature phase. The partial substitution of sulfur by halogen anions can stabilize the cubic HT phase at room temperature[221,222] and results in a good conductivity of $\sim 10^{-3}$ S cm^{-1}.[223]

Fig. 9a shows the unit cell of Li_6PS_5X. The framework of the lattice is built-up by PS_4^{3-} anions that are centered at the 4b sites, with the remaining sulfur occupying the 4a and 4c sites.[224] Upon substitution of sulfur with halogens, sulfur constituting the PS_4 groups are not replaced but instead, halogens occupy the 4a or 4c sites. The Li^+ ions are located at the 48h and 24g Wyckoff sites, with the 24g sites acting as the transition state between hops from 48h to 48h. Twelve 48h sites surround each 4c site, and form a cagelike structure depicted in Fig. 9b.[224] Li diffusion occurs through three different jump processes: the 48h–24g–48h, which is termed a doublet jump; and the 48h–48h jumps within the cage, and between cages, which are deemed the intracage and intercage jump, respectively.[222,224] MD simulations show that the low jump rate of intracage jumps limit the macroscopic diffusion, as shown in the trajectory and jump events in Fig. 9c and d.[222] With the replacement of sulfur by a halogen, Li vacancies are introduced *via* charge compensation. The halogen distribution determines the distribution of Li vacancies and thus the local Li ion diffusivity. I^- ions only occupy the 4a site, whereas Cl^- (or Br^-) show disorder over the 4a sites (inside the cage) and 4c sites (outside the cage). The disorder of halogen ions over the 4a and 4c site was confirmed responsible for the high conductivity in Li_6PS_5Cl and Li_6PS_5Br; in contrast the I^- derivative lacks disorder and hence the conductivity is orders of magnitude lower.[222] The effect of an increase of Li^+ concentration and the lattice parameters on the ion conductivity was demonstrated by substitution of P^{5+} with Si^{4+}, showing that the conductivity can be improved to 2×10^{-3} S cm^{-1}.[225]

2.1.2.4 Other new thiophosphates. A few new Li-ion thiophosphate conductors have been recently reported that are not strictly related to the above. One is the very simple compound Li_4PS_4I, discovered utilizing a solvent-based synthesis approach. It exhibits a new structure and a room temperature ion conductivity of about 10^{-4} S cm^{-1}.[226] Previously identified as $Li_7P_2S_8I$, the structure is distantly related to the argryodites, and comprises Li ions and isolated PS_4^{3-} tetrahedra arranged in layers perpendicular to the *c*-axis that are held apart by I^- ions.

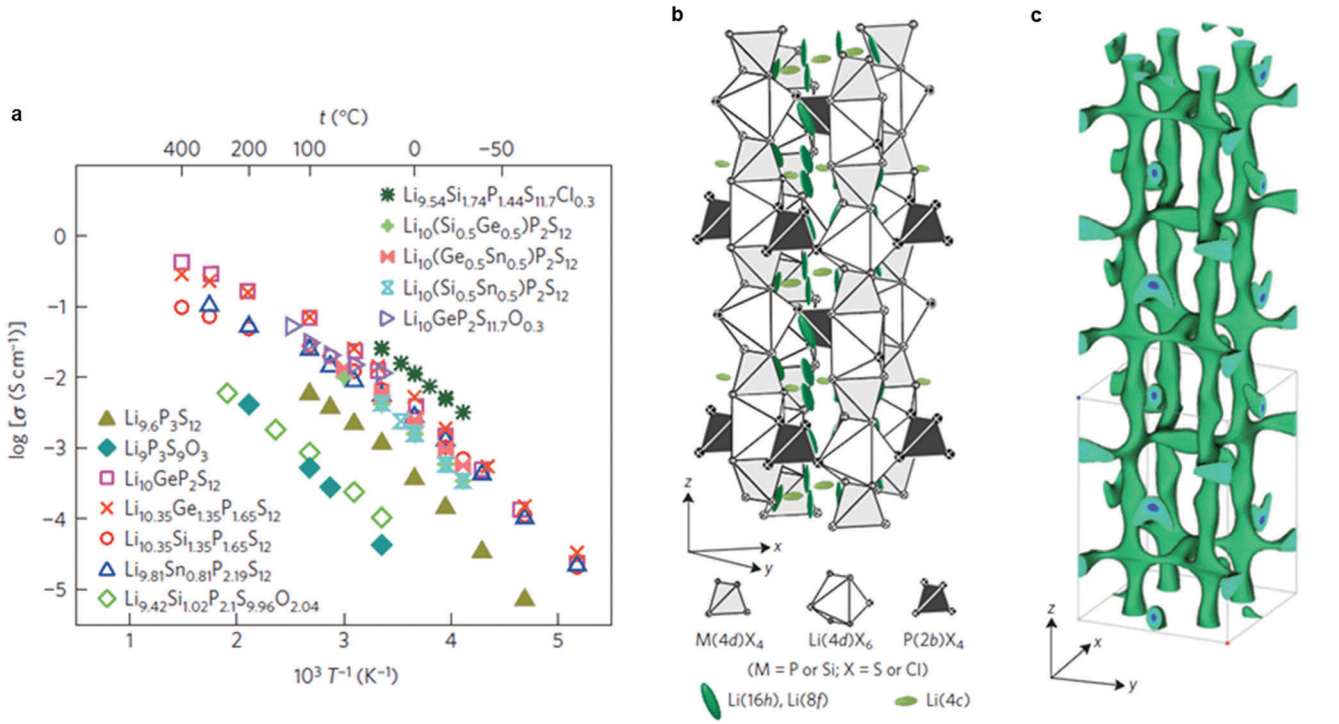

Fig. 8 (a) Arrhenius conductivity plots for the LGPS family, $Li_{9.6}P_3S_{12}$ and $Li_{9.54}Si_{1.74}P_{1.44}S_{11.7}Cl_{0.3}$. (b) Crystal structure of $Li_{9.54}Si_{1.74}P_{1.44}S_{11.7}Cl_{0.3}$. The thermal ellipsoids are drawn with a 50% probability. The framework structure consists of 1D polyhedral chains (edge-sharing $M(4d)X_4$ and $Li(4d)X_6$) connected by $P(2b)X_4$ tetrahedra. Lithium is located on the 16h, 8f and 4c sites. (c) Nuclear distribution of Li atoms in $Li_{9.54}Si_{1.74}P_{1.44}S_{11.7}Cl_{0.3}$ at 25 °C, calculated using the maximum entropy method at the iso-surface level of −0.06 fm Å^{-3}.[46] Reproduced with permission from ref. 46. Copyright (2016), Springer Nature.

Recent calculations give hope that an even higher conductivity $>10^{-2}$ S cm^{-1} may be achieved.[227] The first experimental elucidation of fast lithium ion conductors in the $Li_{1+2x}Zn_{1-x}PS_4$ (LZPS; $x < 0.5$) solid solution whose existence (and conductivity) had only been predicted by theory[228] has also been recently reported.[229] The presence of excess interstitial Li ions in the structure – resulting from the partial substitution of Zn in the parent phase, $LiZnPS_4$ – was identified by combined neutron and synchrotron X-ray powder diffraction studies and correlated with ion conductivity upon increasing the Li/Zn ratio. While the ion conductivity of the parent phase was found to be higher than predicted by theory, conductivities of the solid solution series as high as 1.3×10^{-4} S cm^{-1}, were still two orders of magnitude lower than computation suggested. This was ascribed to the fact that although substoichiometric phases close to those targeted were successfully synthesized, all "defect compositions" were in fact highly metastable. As a result, amorphous and potentially less conductive materials formed as side-products in the grain boundaries may have precluded realization of the true crystalline conductivity.

2.1.2.5 Layered sulfides. A series of fast-conducting sulfide solid electrolytes have recently been identified in the solid solution system $Li_{3x}[Li_xSn_{1-x}S_2]$. The Li-rich prototype with $x = 0.33$, Li_2SnS_3, crystallizes in the layered Na_2IrO_3 structure type (space group $C2/c$), where Li is distributed both in and between Li/Sn-ordered honeycomb sulfide layers according to $Li[Li_{0.33}Sn_{0.67}S_2]$.[230] Brant *et al.* reported Li_2SnS_3 to be a fast Li ion conductor with a room temperature conductivity of 1.5×10^{-5} S cm^{-1} and a conductivity of 1.6×10^{-3} S cm^{-1} at 100 °C.[231] In the Li-depleted version, $Li_2Sn_2S_5$ – with a Li distribution corresponding to $Li_{0.6}[Li_{0.2}Sn_{0.8}S_2]$ ($x = 0.2$) – only 60% of the interlayer gallery Li sites are occupied, thus giving rise to more facile Li diffusion in the *ab*-plane as compared to Li_2SnS_3.[232] In addition, the Li diffusion pathway in $Li_2Sn_2S_5$ involves hops between face-sharing octahedral (O) and tetrahedral (T) Li sites (O–T–O), rather than pure O–O trajectories as in Li_2SnS_3. This pathway is expected to reduce the activation energy for Li diffusion (0.17 eV for $Li_2Sn_2S_5$ as measured by ^{7}Li T_1 relaxation time measurements *vs.* 0.59 eV for Li_2SnS_3, determined from impedance spectroscopy). Indeed, Li^+ diffusivities on the order of 10^{-7} cm^2 s^{-1} were obtained for $Li_2Sn_2S_5$ by pulsed field gradient (PFG) NMR, corresponding to a bulk conductivity of $\sigma_{NMR} = 9.3 \times 10^{-3}$ S cm^{-1}. Polarization measurements and impedance spectroscopy reveal a grain boundary limited conductivity of 1.2×10^{-4} S cm^{-1} and a bulk conductivity that was extrapolated to be two orders of magnitude larger (1.5×10^{-2} S cm^{-1}), in agreement with the PFG NMR measurements.

3. Sodium ion conductors

Sodium-ion batteries (NIBs) have been extensively studied in recent years as candidates for large-scale energy storage,

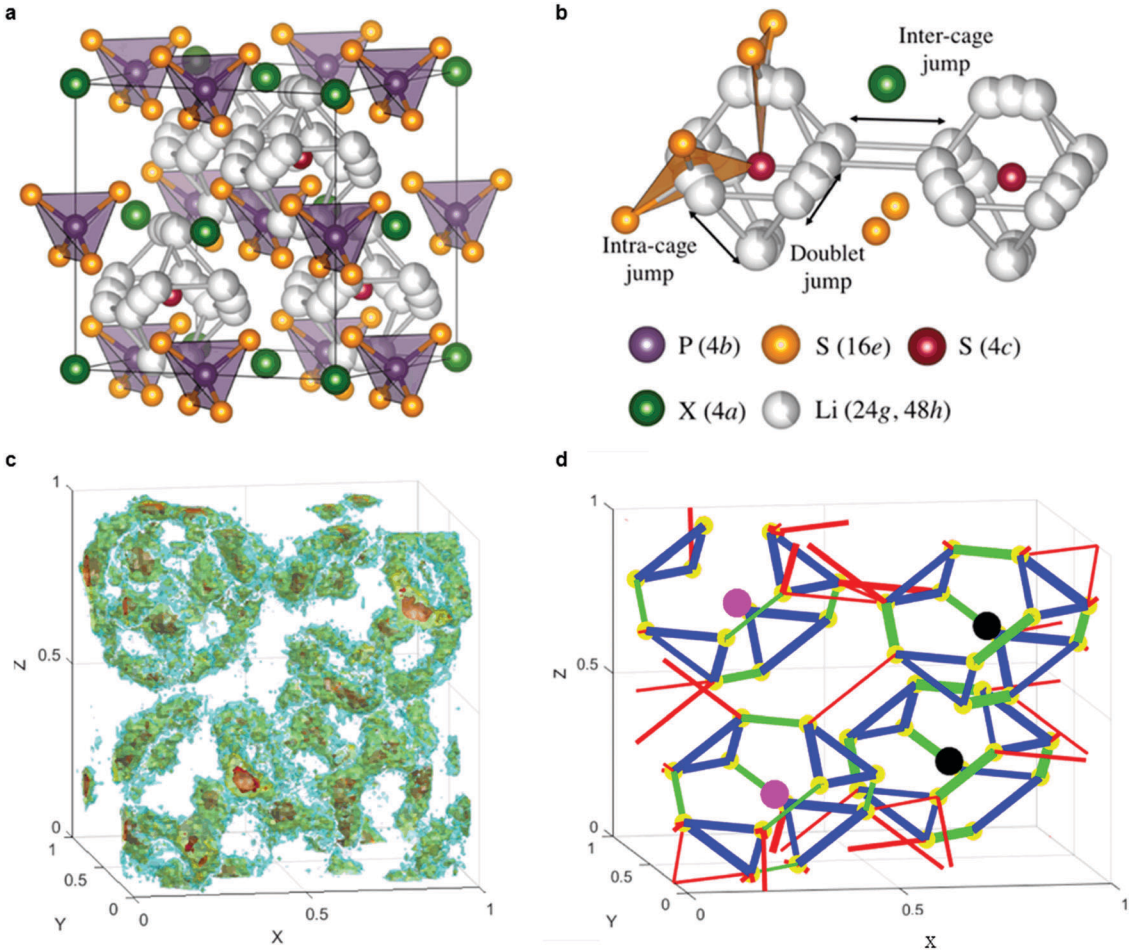

Fig. 9 (a) Crystal structures of Li_6PS_5X with X = Cl, Br, I. In the ordered structure, X-anions form a cubic close-packed lattice with PS_4^{3-} tetrahedra in the octahedral sites and the free S^{2-} (Wyckoff 4c) in half of the tetrahedral holes.[224] (b) The free S^{2-} anions and the corner of the PS_4^{3-} tetrahedra form Frank–Kasper polyhedra, which enclose two different Li positions. The Li positions form localized cages in which multiple jump processes are possible. Jumps between the lithium positions (48h–24g–48h, doublet jump), intracage jumps (48h–48h), and intercage jumps can occur.[224] (c) Li-ion density in Li_6PS_5Cl unit cell during MD simulations at 450 K.[222] (d) Jump statistics from the MD simulations of Li_6PS_5Cl at 450 K. The lines represent three types of Li-ion jumps; green for doublet, blue for intracage, and red for intercage;[222] thicker lines represent larger jump rates. The colored spheres indicate S at 4c (black), Cl at site 4c (pink) and Li-ion sites (48h) (yellow).[222] Reproduced with permission from ref. 222, 224. Copyright (2016, 2017) American Chemical Society.

because of the high abundance and low cost of sodium.[233–235] Similar to LIBs, NIBs also face safety concerns associated with the liquid organic electrolytes contained in the batteries. The pursuit of higher safety, lower cost and longer cycle life batteries renders the development of all-solid-state sodium batteries and sodium ion solid electrolytes highly desirable. In this section, different types of inorganic solid sodium ion conductors are described to give a global view of the solid-state sodium ion conductors available to date.

3.1 Na–β″-Al_2O_3

Na-β″-Al_2O_3 ceramics are well-known fast Na^+ ion conductors and are widely used as solid electrolytes for Na–S and Na–metal chloride batteries.[236] Owing to its high ion conductivity (0.2–0.4 S cm^{-1} at 300 °C), Na-β″-Al_2O_3 is considered as one of the best solid electrolytes for solid-state sodium batteries.[236] However, its extremely high sintering temperature (1200–1500 °C) limits its application. The development, applications as well as the challenges of Na-β″-Al_2O_3 in high temperature Na batteries have been reviewed by Rojo's group.[236]

3.2 NaSICON-type sodium ion conductors

NaSICON-type Li conductors were introduced in Section 2.1.5; in this part, NaSICON-type Na-ion conductors will be reviewed. NaSICONs derive from $NaZr_2(PO_4)_3$ by partial substitution of Si for P, yielding the general formula $Na_{1+x}Zr_2Si_xP_{3-x}O_{12}$ ($0 \leq x \leq 3$). The optimum total ion conductivity is obtained when $x \approx 2$, *i.e.* $Na_3Zr_2Si_2PO_{12}$ (6.7×10^{-4} S cm^{-1} at 25 °C and 0.2 S cm^{-1} at 300 °C).[107,237] The prominent ion conductivity of this system is due to the high mobility of Na ions throughout the open three-dimensional (3-D) framework, which is created by corner-sharing SiO_4/PO_4 tetrahedra and ZrO_6 octahedra *via* common oxygen atoms. Apart from its excellent ion conductivity, NaSICON ceramics are reported to show low thermal expansion, and are thus suitable for use at medium or high temperature. The open

framework of NaSICON allows a wide range of chemical substitutions, for example, the Zr^{4+} site can be occupied by a variety of di, tri, tetravalent and pentavalent cations, and the Si/P site can be substituted by Ge^{4+} or As^{4+}.[238,239]

The efforts at chemical substitution have shown some success in improving the conductivity. For example, Hf-substituted NaSICON – $Na_{3.2}Hf_2(SiO_4)_{2.2}(PO_4)_{0.8}$ – exhibits a much higher ion conductivity than its Zr analogue (2.3×10^{-3} S cm^{-1} at room temperature).[240] Unfortunately, Hf is a rare metal and in limited supply. Takahashi *et al.* investigated the effects of divalent (Mg^{2+}, Zn^{2+}), trivalent (Y^{3+}), tetravalent (Ti^{4+}, Sn^{4+}), and pentavalent dopants (V^{5+}, Nb^{5+}, Ta^{5+}) on the electrical conductivity and density of NaSICON.[241] All of these result in well-sintered, dense ceramics and enhanced electrical conductivity at high temperature, but the conductivity at low temperature was not reported. However, these doped systems are mixed conductors and only for Mg-doped and Nb-doped systems can the electronic conductivity be neglected. NaSICON ceramics are often not monophasic but are accompanied by a glassy phase.[242] The glassy phase generally comprises sodium, phosphate or silicate and the doping element,[241–243] as demonstrated in the Mg^{2+},[241] Co^{2+},[241] Ce^{4+},[243] Yb^{3+} (ref. 243) and Gd^{3+} doped[243] NaSICON systems. In addition, monoclinic zirconia is easily formed from the liquid phase during the sintering.[243–247] Some studies found that the doping and sintering conditions also affect the microstructure and the nature of grain boundaries, and hence influence the conductivity.[248]

Recently, a high ion conductivity of 4.0×10^{-3} S cm^{-1} at room temperature was reported for Sc-doped NaSICON, which is the highest value amongst the reported NaSICON-type conductors.[249] Based on a range of ion conductivity and structural data of NaSICON-type materials, Guin *et al.*[250] concluded that the highest ion conductivity was obtained when the Na content approximates 3.3 mol of Na per formula unit and the mean size of the M cations is close to 0.72 Å. In addition, the monoclinic-to-rhombohedral phase transition temperature was found to be influenced by doping. Jolley *et al.*[251] found that aliovalent substitution of Zr^{4+} stabilized the higher symmetry rhombohedral phase of NaSICON, among which Y^{3+} substitution resulted in the lowest phase transition temperature and the smallest lattice distortion.

Zhang *et al.* proposed a self-forming strategy to develop composite solid electrolytes with high ion conductivity, which was demonstrated by modifying NaSICON with La^{3+}.[252] For example, in the case of La^{3+}, its very limited solubility in the NaSICON framework ultimately results in separation of $Na_3La(PO_4)_2$ as a second phase, which mediates both the composition of the bulk and the grain boundary, leading to improved conductivity (3.4×10^{-3} S cm^{-1} at 25 °C). This strategy can be extended to design other fast ion conductors. Extensive studies of the stability of NaSICON with respect to metallic Na have been conducted.[253,254] Unfortunately, especially when phosphorus is present, NaSICONs are not stable at 300 °C in contact with molten sodium, but at lower temperatures (100 °C) no reaction is seen.[253,254]

3.3 Sulfide based sodium ion conductors

As in the case of Li, sodium thiophosphate materials have attracted much attention in recent years because of their relatively high ion conductivity, negligible grain boundary resistance and good ductility.[45,255] Nonetheless, there are much fewer Na superionic conductors compared to Li sulfides, and their room temperature ion conductivities remain low. Exploration of highly conductive sulfide-based sodium ion conductors is eagerly underway.

An exciting milestone in the development of Na ion conductors was the stabilization of the high-temperature cubic phase of Na_3PS_4 (c-Na_3PS_4, space group: $I\bar{4}3m$) by crystallization from the glassy state, which exhibited high Na^+-ion conductivity (2×10^{-4} S cm^{-1}).[198] The conductivity was subsequently improved to 4.6×10^{-4} S cm^{-1} by using high purity (>99%) Na_2S as a precursor. This achievement for c-Na_3PS_4 ignited a resurgence of interest in sodium thiophosphates, given that the tetragonal phase of Na_3PS_4 (t-Na_3PS_4, space group: $P\bar{4}2_1c$) exhibits a conductivity one order of magnitude lower.[256] The substantial difference in the ion conduction properties was initially assumed to imply that fast ion conduction is causally related to the symmetry of Na_3PS_4. Fig. 10a shows the average cubic and tetragonal Na_3PS_4 crystal structures along the *b*-axis.[257] Only small structural differences exist between the two polymorphs of Na_3PS_4, mostly in the Na cation distribution, the orientation of the PS_4^{3-} tetrahedral, and the lattice dimensions.

Nevertheless, despite the experimental discrepancy between the cubic and tetragonal phases, theoretical calculations indicated, in fact, that both pristine c-Na_3PS_4 and t-Na_3PS_4 structures exhibit extremely poor and similar ion conductivity.[258] Systematic investigations of the synthesis parameters for Na_3PS_4 under different conditions (*e.g.*, temperature, nature of the reaction vessel, mass of the precursors) revealed that reaction of the precursors with the reaction vessels produced different polymorphs.[259] These results suggest that the stabilization of metastable c-Na_3PS_4 can not be explained only by an entropy contribution, but is more likely induced by the precursors reacting with the silica reaction tubes. Elements from the tubes may be incorporated into the structure of Na_3PS_4 or alternatively, off-stoichiometry may be induced in the structure by consumption of some precursors *via* the reaction with the tubes. The latter is more likely,[259] considering that aliovalent doping (*e.g.*, the replacement of P^{5+} with Si^{4+}) appears to be not energetically favorable.[258]

New efforts have been made to uncover the origin of the enhanced ion conductivity in cubic Na_3PS_4, and to determine if the difference in the transport behaviour between the cubic and tetragonal phases arises from structural differences, microstructural variations, or disparities in the defect concentration. Rietveld and pair distribution function (PDF) analyses were performed to probe the average and local structures of Na_3PS_4 prepared through two different synthetic routes (ball-milling and high temperature synthesis).[257] While Rietveld analysis indeed points to the average structure of Na_3PS_4 prepared through ball-milling and high temperature routes being cubic and tetragonal, respectively, PDF analyses showed that both Na_3PS_4 compounds exhibit the same tetragonal structural motif on the local scale (Fig. 10b). EIS suggests that the high ionic conductivity of "c"-Na_3PS_4 is not related to the crystal structure, but rather the defects induced by the harsh ball-milling conditions.[257]

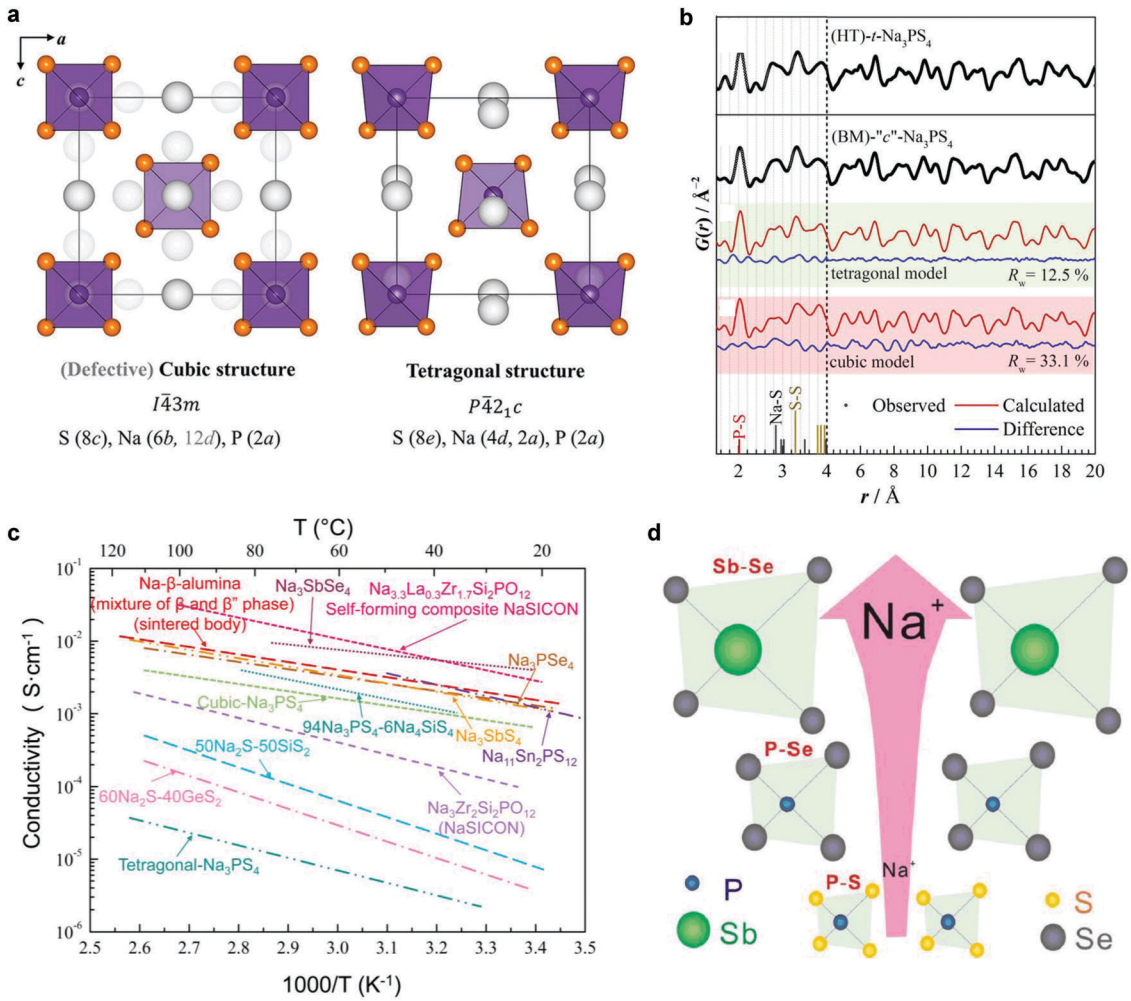

Fig. 10 (a) Crystal structure of cubic and tetragonal Na_3PS_4 projected in the (010) plane. The perfectly cubic phase (*i.e.*, no occupancy of the 12d positions) shows PS_4^{3-} tetrahedra in a body centered lattice. In the tetragonal modification, a minor rotation of the tetrahedra leads to a splitting of the Na positions and an elongation of the *c*-lattice parameter;[257] (b) experimentally obtained *G*(*r*) data for (a) HT-t-Na_3PS_4 and BM-"c"-Na_3PS_4 showing that there is no significant difference in the local structure. BM-"c"-Na_3PS_4 was fitted using a tetragonal model, shaded in green and a cubic model shaded in red. Experimental data are shown as black points. The red line denotes the calculated pattern, and the difference profile is shown in blue.[257] Reproduced with permission from ref. 257. Copyright (2018) American Chemical Society. (c) Temperature-dependent ionic conductivities of various Na^+ ion solid electrolytes, including both oxides and sulfides.[198,252,256,261,262,265–270] Reproduced with permission from ref. 198, 265. Copyright (2012, 2017), Springer Nature. Reproduced with permission from ref. 252, 261, 262. Copyright (2015, 2016), Wiley. Reproduced with permission from ref. 256, 268, 269, 270. Copyright (1980, 1981, 1992, 2012), Elsevier. Reproduced with permission from ref. 266, 267. Copyright (2014, 2018), Royal Society of Chemistry. (d) Schematic diagram of Na ion diffusion in Na_3PS_4 and related phases.[265]

Although stoichiometric Na_3PX_4 (X = S, Se) compounds were determined to be poor Na ion conductors, theoretical work also suggested that reasonably high conductivity can be realized with the introduction of Na^+ interstitials or Na vacancies that induce disorder.[258,260] A computational study on the effect of aliovalent doping of M^{4+} (M = Si, Ge, Sn) for P^{5+} in c-Na_3PS_4 predicted a conductivity of 1.66×10^{-3} S cm^{-1} for 6.25% Si-doped Na_3PS_4, in very good agreement with the reported experimental value of 7.4×10^{-4} S cm^{-1}. Remarkably, Sn^{4+} doping at the same concentration contributed to a much higher predicted conductivity of 1.07×10^{-2} S cm^{-1} even though the dopant formation energy is higher than the Si^{4+} dopant.[258] These studies prove that the presence of defects are essential to enable fast Na-ion diffusion in Na_3PX_4.

Anion substitution with Se^{2-} – larger than S^{2-} – is another strategy to improve conductivity. Due to its higher polarizability, the replacement of Se^{2-} for S^{2-} expands the lattice and weakens the binding energy between the mobile cations and anion framework. Cubic Na_3PSe_4 with a conductivity of 1.16×10^{-3} S cm^{-1} and a low activation energy of 0.21 eV was first reported by Zhang *et al.*[261] They also reported vacancy-containing tetragonal Na_3SbS_4 with a very high conductivity of 3×10^{-3} S cm^{-1} formed by substituting Sb^{5+} for P^{5+} in Na_3PS_4.[262–264] Na_3SbS_4 was reported to be stable in dry air,[262] as rationalized by hard and soft acid and base (HSAB) theory. Very surprisingly (and questionably), Na_3SbS_4 is reported to show good compatibility with metallic Na, and to be electrochemically inert up to 5 V based on cyclic voltammetry (CV) measurements.

Nonetheless, although CV is a valuable technique, it is not sufficient to assess stability of an SE since it is too fast to detect slow decomposition reactions in ASSBs. Recently, Zhang's group successfully synthesized Sb- and Se-substituted Na_3SbSe_4 with a high conductivity of 3.7×10^{-3} S cm^{-1} and low activation energy of 0.19 eV.[265] The conductivity of these compositions and the schematic illustration of anion and cation size on Na ion transport are shown in Fig. 10c and d, respectively.[198,252,256,261,262,265–270]

The Na version of LGPS represents another class of sulfide conductors. $Na_{10}GeP_2S_{12}$ (NGPS) was computationally predicted to have a conductivity of 4.7×10^{-3} S cm^{-1} by Kandagal *et al.*[271] Richards *et al.*[272] subsequently predicted an increase in the Na^+ diffusivity and a decrease in activation energy in the series Sn < Ge < Si for $Na_{10}MP_2S_{12}$ (M = Si, Ge, Sn). They reported the composition $Na_{10}SnP_2S_{12}$ with an experimental conductivity of 4×10^{-4} S cm^{-1},[272] but the structure was not disclosed. MD simulations suggested it is a 1D ion conductor, with chains of NaS_4 tetrahedra linked along the *c*-axis providing facile diffusion. Later, Hayashi's group reported a glass-ceramic with a nominal composition of "$Na_{10}GeP_2S_{12}$" that showed a conductivity of 2.4×10^{-5} S cm^{-1} and a XRD pattern similar to the simulated "$Na_{10}SnP_2S_{12}$". However, the structure was again not resolved.[272] Very recently, the targeted synthesis of stoichiometric $Na_{11}Sn_2PS_{12}$ as a polycrystalline powder provided a pure phase material that exhibits a very high conductivity of 1.4×10^{-3} S $\times$ cm^{-1} and low activation energy of 0.24 eV.[267] The structure of the new phase, $Na_{11}Sn_2PS_{12}$ was solved from single crystal X-ray diffraction (Fig. 11a and b). In contrast to the LGPS (or NGPS) structure type, the Na^+ ions occupy only octahedral sites and the Na ion conductivity is completely three dimensional as demonstrated by AIMD simulations (Fig. 11c–e).[267] Vital to ion conduction in this 3D percolating network is the disorder of the Na^+ ions over the almost-fully occupied and partially occupied sites that alternate in all crystallographic directions. Low energy Na^+-ion hopping is favored by the equi-energetic octahedral sites, and spacious iso-energetic pathways for transport. Experimental measurement of ion conductivity and activation barrier for Na-ion mobility closely matched that from AIMD simulation (0.20 eV), with the E_a being the lowest reported for a sodium thiophosphate in the literature to date. Following this publication, the same phase was also reported elsewhere, with a higher conductivity (3.7×10^{-3} S cm^{-1}) but also with an unusually higher activation energy (0.39 eV).[273]

4. Ion conduction mechanism and principles to design fast ion conductors

4.1 Mechanism of ion conduction

Understanding the ion transport mechanism is critical to guide the design of fast ion conductors. The conventional knowledge of ion transport in solid materials is based on the classic diffusion model which depicts ion diffusion as the hopping of an individual ion from one lattice site to its adjacent vacant site, which is termed "direct-hopping" (Fig. 12a).

The ion conductivity of solid materials is closely related to crystal structure and is governed by the ion concentration (n), activation energy (E_a), and the mobility of mobile ion carrier (μ):

$$\sigma = nq\mu \quad \text{and} \quad \mu \propto \exp(-E_a/k_BT)$$

where q is the charge of the mobile ions, E_a is the activation energy, and k_B is the Boltzmann constant.

A low activation energy and high concentration of mobile ion carrier species (vacancies or interstitials) are necessary to obtain high conductivity. The underlying crystal framework

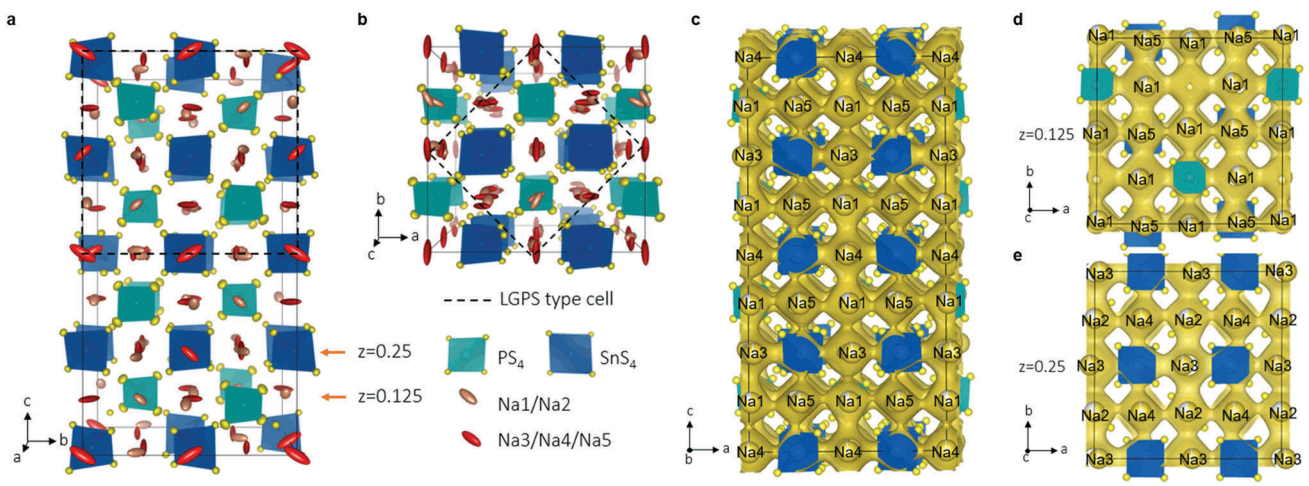

Fig. 11 Structure of $Na_{11}Sn_2PS_{12}$ from single crystal data. (a) The framework showing ordering of the SnS_4 (dark blue) and PS_4 (light blue) tetrahedra; yellow spheres are S; and rose/red ellipsoids are sodium ions. The Na(1)/Na(2) ions (sites with fractional occupancy) are represented by pink ellipsoids and the Na(3)/Na(4)/Na(5) ions (almost fully occupied sites) are shown as red ellipsoids; (b) the small tetragonal cell ($a' \times a' \times c'$) equivalent to $Li_{10}GeP_2S_{12}$ is related to the actual tetragonal cell ($a \times a \times c$) of $Na_{11}Sn_2PS_{12}$ as follows: $a = a'\sqrt{2}$; $c = 2c'$; Na-ion probability density isosurface (yellow) obtained from *ab initio* molecular dynamics (AIMD) studies at 1050 K for 40 ps, showing the nature of the 3D Na^+ ion conduction paths: (c) sodium diffusion along the c axis involves a pathway along –Na(4)–Na(1)–Na(3)–Na(1)– chains; the Na-ion probability density obtained from the AIMD Na-ion trajectories in the *ab* plane shows the pathways at (d) z = 0.125 and (e) z = 0.25.[267] Reproduced with permission from ref. 267. Copyright (2018), Royal Society of Chemistry.

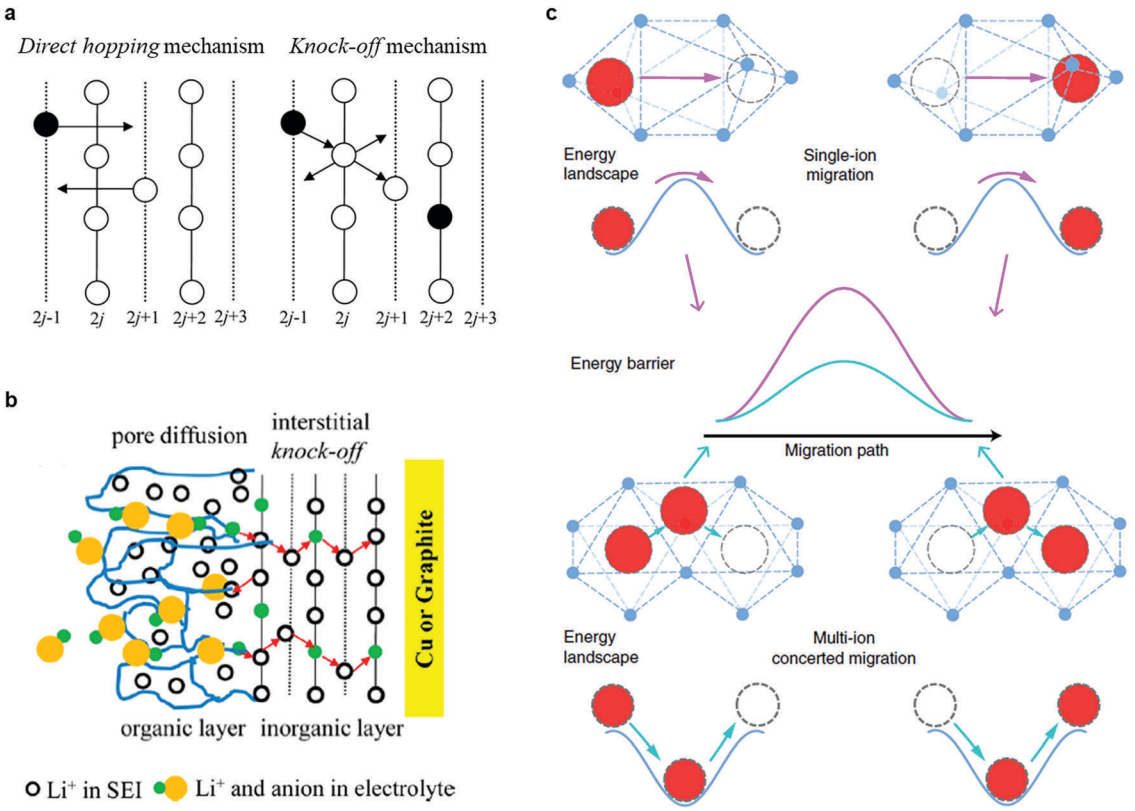

Fig. 12 (a) Schematic illustration of the direct hop mechanism and knock-off mechanism; (b) schematic drawing of pore diffusion in the porous organic layer of SEI and knock-off diffusion in the dense inorganic layer of SEI (Li_2CO_3).[275] The open circles represent the Li^+ already in the SEI. In the porous organic layer, the blue solid lines denote channels through which Li^+ in the electrolyte (green filled circles) transports with anions (yellow filled circles) *via* pore diffusion. The red arrows denote that only Li^+ can diffuse in the dense inorganic layer *via* the knock-off mechanism;[275] Reproduced with permission from ref. 275. Copyright (2012) American Chemical Society. (c) Schematic illustration of single-ion migration *versus* multi-ion concerted migration. For single-ion migration (upper insets), the migration energy barrier is the same as the barrier of the energy landscape. In contrast, the concerted migration of multiple ions (lower insets) has a lower energy barrier as a result of strong ion–ion interactions and unique mobile ion configuration in super-ion conductors.[274] Reproduced with permission from ref. 274. Copyright (2017), Springer Nature.

determines the energy landscape of ion migration, while the energy barrier depends on the highest energy of the energy landscape along the decisive migration pathway (saddle-point). For the same crystal framework, similar migration barriers were predicted according to the classic diffusion model, which failed to explain the significantly lower activation energy barriers and abrupt increase in ion conductivity observed at certain doped composition (*e.g.*, doped LLZO and NaSICON).[274]

Besides the classical "direct hopping" mechanism, another conduction mechanism was also proposed. Using DFT calculations, Shi *et al.*[275] predicted that the dominant intrinsic defect in Li_2CO_3, Li_i^+, prefers to diffuse through a correlated migration mechanism (Fig. 12b and c), as opposed to the direct hop mechanism. Later, they also found that in β-Li_3PS_4, the correlated migration of Li_i^+ along [010] has the lowest migration barrier.[276] The correlated mechanism is in fact the same as the later proposed "concerted mechanism" or "collective mechanism". The lower migration barrier of the concerted mechanism compared to the conventional direct hop mechanism was also reported in Li_3OX (X = Cl, Br),[100] doped Li_3PO_4,[277] and LLZO.[158] Recently, Mo's group[274] surveyed ion diffusion in a series of fast ion conductors, including $Li_7P_3S_{11}$, β-Li_3PS_4, LiSICON, LLTO, revealing that the mobile ions occupying the high-energy sites can activate concerted migration with a reduced diffusion barrier. Strong ion–ion Coulomb interactions in the unique mobile-ion configuration with high-energy site occupancy are key for achieving low-barrier concerted migration in these solid ion conductors. During the concerted migration of multiple ions, the ions located at the high energy sites migrate downhill, and cancel out a fraction of the energy barrier caused by the uphill-climbing ions. This explains why the super-ionic conduction in doped LLZO and NaSICON is activated at certain compositions with increased alkali ion concentration, and provides a simple strategy to design fast ion conductors: inserting mobile ions into high energy sites to trigger concerted migration with a lower energy barrier.

4.2 Principles to design fast ion conductors

In general, certain structural prerequisites should be satisfied in order to ensure fast ion conduction in solid materials: (1) as ion transport proceeds locally by thermally activated jumps between adjacent sites (local energy minima), jumps need to be connected in "conduction channels" that allow long range transport. These conduction channels should have a suitable

geometry that enables direct passage of the mobile ions but obviates energetically high transition states. While narrow bottlenecks obviously restrict mobility, passages that are too wide also impair motion. For example, the β″-Al_2O_3 and NaSICON structures are more suitable for Na ions, and exhibit higher conduction for Na than Li ions. This may seem counter-intuitive, but results from the interplay between polarizing effect and polarizability. (2) Materials with face-sharing polyhedra, as opposed to edge-sharing, have favorable ion mobility since the bottleneck in the face-shared case is larger. Thus, ion channels with high mobility are easily formed when face-sharing polyhedra are connected throughout the structure of the SE.[99] (3) Different alkali ion sites along the transport path should ideally have similar potential energies with low migration barriers for ion transport between adjacent sites.[278] (4) Structural disorder and hence "partial" vacancies or interstitials in the mobile ion sub-lattice are necessary.[279] Compounds that exhibit only small concentrations of well defined vacancies or interstitials, formed by either Frenkel or Schottky-type defect formation reactions, are usually poor room temperature electrolytes, as the defect formation enthalpy is then included in the activation energy of ion conductivity. (5) The anion sub-lattice arrangement is also paramount for the diffusion of ions as recently highlighted.[99] (6) High polarizability of the anion sub-lattice is advantageous for good cation mobility. Numerous sulfide, thiophosphate, and iodide materials show higher conductivity than oxides for this reason. The important role of the polarizability of the anion sublattice has recently been highlighted using lithium superionic argyrodites Li_6PS_5X (X = Cl, Br, I) and sodium superionic $Na_3PS_{4-x}Se_x$ as examples: softer bonds lower the activation barrier but simultaneously decrease the prefactor of the moving ions.[224,280] In fact, the softer lattice is associated with smaller attempt frequencies, and thus, a smaller pre-factor.[279] This explains some old empirical rules connecting prefactors and activation energies, and suggest that design rules for SEs need to consider both the energy landscape (activation barriers) and the phonon spectrum (attempt frequencies).[224,279,280] (7) General thermodynamic arguments have led to – at least in simple structures – a powerful search strategy that is based on the correlation between charge carrier concentrations and melting points (also Tammann's rule[281]) that has been elucidated by Maier's group.[282]

Ceder's group proposed (geometric) design principles for superionic conductors and suggested that a body-centered cubic-like (bcc) anion framework allows the Li^+ ions to migrate within a network of interconnected tetrahedral sites with a lower activation barrier than other close-packed frameworks and is most desirable for achieving high ionic conductivity.[99] This feature was verified in recently discovered highly conducting materials such as $Li_{10}GeP_2S_{12}$[220] and $Li_7P_3S_{11}$,[210] whose sulfide sub-lattices match a bcc lattice very closely (note α-AgI is a prototype bcc structure and an excellent SE[283]). Poorer conductors such as Li_2S have a fcc sulfide sublattice, while Li_4GeS_4, Li_3PS_4 and thio-LiSICON have a hcp sulfide sublattice. This can be readily explained by considering that for all the sulfide sublattices, tetrahedral sites are energetically most stable for Li^+ ions. In the bcc sulfide sublattice, the Li^+ ion migrates with an extremely low barrier of 0.15 eV along the path connecting two face-sharing tetrahedral sites (Fig. 13a). In the fcc lattice, Li^+ ions migrating between two tetrahedral sites have to pass through an intermediate octahedral site, which makes the energy barrier much higher (Fig. 13b). The same situation exists in the *a*–*b* plane of the hcp lattice (Fig. 13c). The frameworks of some structures cannot be closely matched to either a bcc, fcc or hcp sublattice, but accommodate a network composed entirely of tetrahedral sites for the mobile cations, in which cation migration through the percolating face-shared tetrahedral sites also shows low activation energy. Such frameworks can be found in argyrodite-type Li_6PS_5Cl[224] and cubic-Na_3PS_4.[198] Li_4PS_4I is another example, where PS_4^{3-} and I^- ions together form a bbc anion sublattice.[226]

Additionally, it is worth noting that more efforts are needed to reduce the grain boundary resistance for crystalline materials, especially oxides. In heterogeneous systems, the contribution of interfaces determines the overall conducting property. The research on synergistic ion conduction effects in heterogeneous systems originated from the discovery of solid–solid composite electrolytes (typically formed by uniformly admixing fine oxide particles in an ion conducting matrix, *e.g.*, LiI:Al_2O_3 or CaF_2:SiO_2) which show an anomalously high conductivity in comparison with pure phases[284] due to increased carrier contributions.[285] The space charge concept was introduced to interpret the adsorption effect of one type of ion on an insulating surface along with the significance of boundary layers with regard to ionic conduction. There is the possibility of excess storage in nano-composite materials due to the space charge effects.

This composite concept proved powerful for increasing carrier concentrations but not mobilities. In Section 2.1.1.1 we briefly mentioned LLT composites in which the admixture of SiO_2 or Al_2O_3 decreased the grain boundary resistance by affecting the grain boundary structure directly. The conductivity of glass-ceramic electrolytes is influenced by the interface between them.[286] The existence of a fast ion conduction interfacial regime between the glassy and crystalline phases was verified by Schirmeisen *et al.*[287] A general explanation for these anomalies relies on space charge models that consider the depletion or accumulation of lithium vacancy point defects as a consequence of the defects at the interface.

Solid–liquid composite systems such as soggy-sand electrolytes[288,289] or ion-exchange polymers[290,291] deserve a brief mention in this context as they can offer excellent compromises between electrical properties (high conductivities and high Li-transference numbers) and mechanical properties (malleability, flexibility and good contact to electrode particles) that are difficult to achieve with pure solid phases. Similarly, enhanced conductivity with a percolation behavior has also been observed in these heterogeneous systems.[288]

Another very interesting synergistic coupling between $Li_{6.75}La_3Zr_{1.75}Ta_{0.25}O_{12}$ (LLZTO) ceramics and poly(vinylidene fluoride) (PVDF) polymer electrolyte was reported by Nan's group.[292] A combination of experiments and DFT calculations

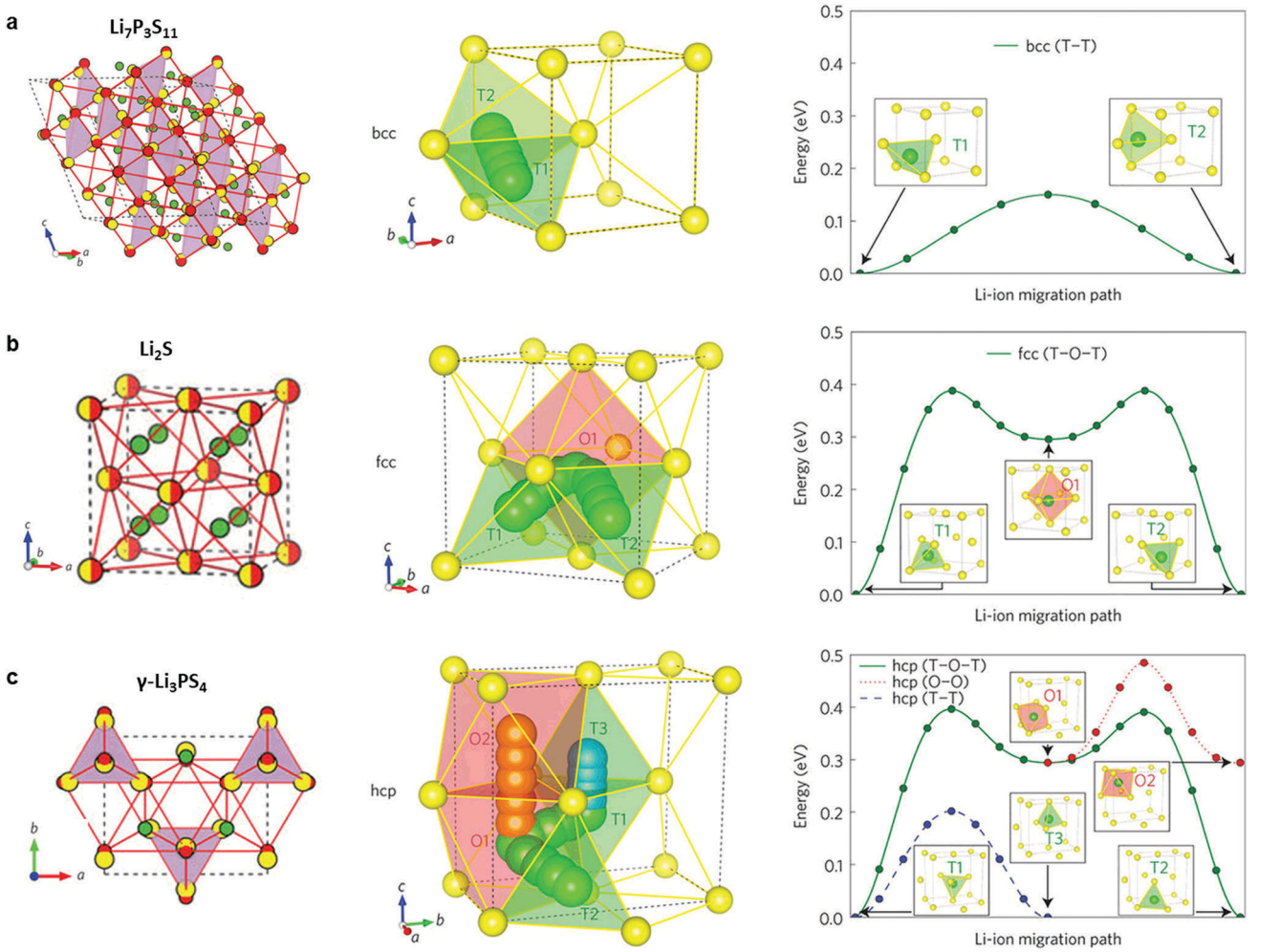

Fig. 13 (a–e) Crystal structure of the Li-ion conductors: (a) $Li_7P_3S_{11}$, (b) Li_2S; (c) γ-Li_3PS_4. The Li ions, partially occupied Li^+ sites, S^{2-} anion, PS_4 tetrahedra and GeS_4 tetrahedra (partially occupied in $Li_{10}GeP_2S_{12}$) are coloured green, green-white, yellow, purple and blue, respectively. In both $Li_{10}GeP_2S_{12}$ and $Li_7P_3S_{11}$, the sulfur anion sublattice can be closely mapped to a bcc framework (red circles connected by red lines). In Li_2S, the anion sublattice is an exact fcc matrix (yellow-red circles). The anion sublattices in γ-Li_3PS_4 and Li_4GeS_4 are closely matched to a hcp framework.[99] Reproduced with permission from ref. 99. Copyright (2015), Springer Nature.

imply that the La atom of LLZTO could complex with the N atom and C═O group of solvent molecules such as *N*,*N*-dimethylformamide, along with electrons enriched at the N atom, which behaves like a Lewis base and induces the chemical dehydrofluorination of the PVDF skeleton. Partially modified PVDF chains activate the interactions between the PVDF matrix, lithium salt, and LLZTO fillers, hence leading to significantly improved conductivity.[293]

5. Evaluation of the electrochemical stability of SEs

Although significant progress has been made in the search for solid electrolytes with high ion conductivity, there are still many fundamental challenges impeding the commercialization of solid-state batteries.[7,294] Most notably, these include chemical/electrochemical stability and resistance at the interface between the solid electrolytes and electrode materials. The properties of the SE/electrode interface – at both the positive and negative sides – are of vital importance to the function of the ASSBs.

Although some fast-ion conducting solid electrolytes (mainly sulfides, thiophosphates and their derivatives, *e.g.*, $Li_{10}GeP_2S_{12}$, $Li_7P_3S_{11}$, Li_6PS_5Cl) show promising conductivity comparable to – or even higher than – liquid electrolytes, the ASSBs assembled with these SEs typically exhibit inferior electrochemical performance than their liquid-cell counterparts. The sluggish charge-transfer across the SE/electrode interface caused by high interfacial resistance is usually the limiting factor for the poor cell kinetics.[7] The origins of the interfacial resistance are nested in one or more factors: poor physical interfacial contact;[295] mechanical failure of the contact with volume variation;[296] formation of lithium/sodium-depleted space-charge layers due to the large chemical potential difference between SE and electrode materials;[297] and degradation at the interface that is caused by mutual diffusion of elements and/or reactivity that results in

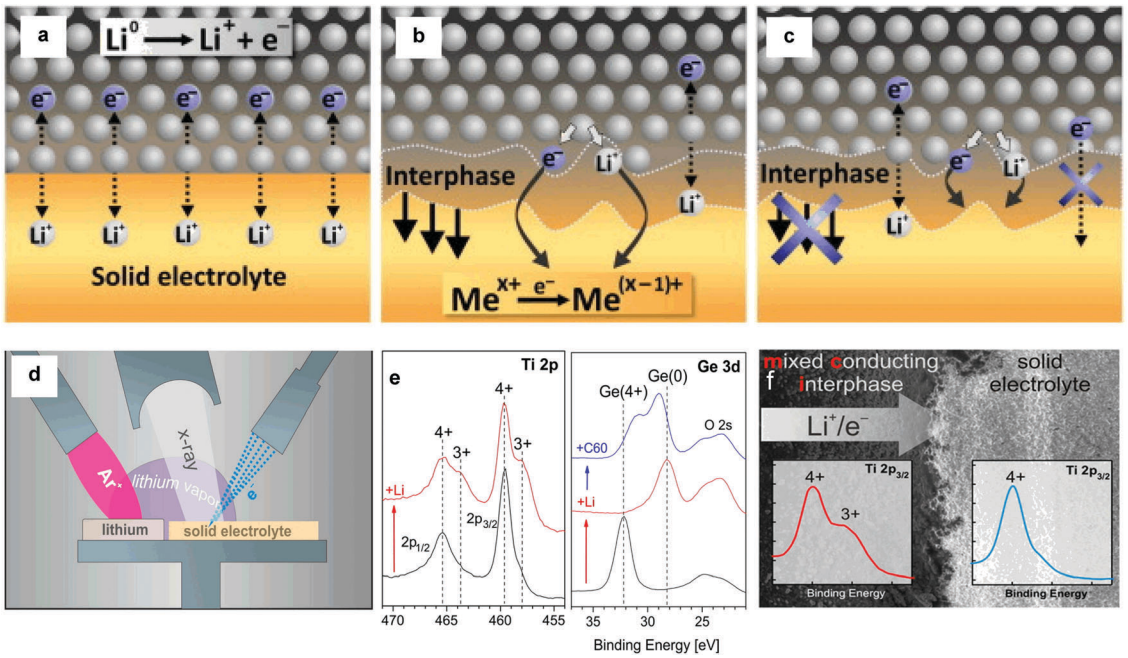

Fig. 14 Types of interfaces between lithium metal and a solid lithium ion conductor. (a) Non-reactive and thermodynamically stable interface. (b) reactive and mixed conducting interphase (MCI). (c) Reactive and metastable solid–electrolyte interphase (SEI).[299] Reproduced with permission from ref. 299. Copyright (2015), Elsevier. (d) *In situ* lithiation of solid electrolytes during XPS surface analysis. The argon ion gun is used to sputter from a lithium metal foil placed in the vicinity of the sample of interest. (e) XPS detail spectra of an LATP and LAGP sample before (bottom, black line) and after lithiation (middle, red line). (f) SEM cross-section image of a LATGP sample after approximately 12 h contact with lithium metal. The white arrow indicates the chemical diffusion of lithium into the material.[300] Reproduced with permission from ref. 300. Copyright (2013), American Chemical Society.

formation of an interphase.[298] Interphase formation may be ascribed[299] to several different sources. One is the reduction (at the negative electrode) or oxidation of SEs (at the positive electrode) due to the intrinsic thermodynamic instability of the SEs. SEs are often claimed to exhibit excellent stability based on wide electrochemical windows of 0–5 V or even higher that are typically derived from relatively fast CV measurements on the Li/SE/inert blocking electrode. These experiments do not reflect the practical battery situation as they are too fast to detect slow decomposition reactions at the interfaces. A second source is reactions between the SE and the electrode materials caused by the chemical instability between these two layers. Finally, interphases can be formed *in situ* by electrochemical reactions of the SE/electrode interface during charge/discharge processes. These three reaction types are different at the positive and negative electrodes, and are explained in more detail below.

At the negative electrode, three different types of interfaces can be distinguished in the Li metal/SE contact, as schematically presented in Fig. 14a: (1) a thermodynamically stable interface; (2) a mixed conducting (growing) interphase (MCI); (3) and a metastable (non-growing) interphase (SEI).[299] The properties of these three interfaces influence the charge transfer kinetics differently. In the first case, Li metal and the SE in contact are *a priori* in thermodynamic equilibrium and metal ion transfer and associated relaxation steps will be rate-limiting. In the second and third cases, Li metal and the SE are thermodynamically unstable when in contact, and the reaction products control the transport properties of the interphase. As shown in Fig. 14b, a mixed conducting interphase forms and grows "into" the bulk of the SE material, if the formed products possess sufficient partial electronic and ion conductivity, resulting in the destruction of the electrolyte and eventual self-discharge of the battery. On the other hand, a stable interphase may form if the reaction products are ion-conducting but electronically insulating or if the electronic conductivity is fairly low (Fig. 14c). The decomposition products inhibit continuous decomposition, acting as SEIs. While such interphases are inevitably formed, they are extremely difficult to monitor because of their thickness and the sparse techniques that are available to explore their buried nature. High resolution transmission electron microscopy studies – an obvious first choice – can in fact result in extensive beam damage, occluding the subject of investigation. Both surface science and theory have proven more insightful in predicting and identifying the interphase. In particular, *in situ* XPS (Fig. 14d), in combination with EIS has been shown to be a powerful tool to investigate the compatibility of SEs with lithium metal.[213,299,300]

DFT calculations suggest that most Li–SEs are thermodynamically unstable against lithium metal as expected.[10,301] Sulfides show a significantly narrower thermodynamic stability window than oxide-based SEs.[301] The reduction products of thiophosphates at the Li interface are predicted to include Li_3P and Li_2S, and for those SE materials containing Ge, Cl, and I, a Li–Ge alloy, LiCl and LiI are formed, respectively. Theory[11] and XPS results[302] both show that LGPS is reduced at 0–1.7 V

and oxidized at 2–2.5 V. The final decomposition products in equilibrium with Li metal are $Li_{15}Ge_4$, Li_3P and Li_2S. These data are in contrast to the originally reported 0–5 V electrochemical window from CV measurement.[45] The electrochemical stability window of SEs is overestimated by CV method because of the slow kinetics of the decomposition reactions due to the limited contact area between the SE and the inert blocking electrode.[303] However, in practical bulk ASSBs, the reduction/oxidation kinetics of SE in the composite electrode is greatly accelerated, owing to the much larger contact area between the SE and electronic conductive additives that are poised at the electrode potential. Along the same lines, even though LiPON is reduced at 0.69 V according to theory, it was thought to be stable in contact with lithium metal; however, *in situ* XPS reveals that it actually reacts with lithium metal to form Li_3PO_4, Li_3P, Li_3N and Li_2O.[304] Similarly, Ge-containing oxide materials $Li_{1.5}Al_{0.5}Ge_{1.5}(PO_4)_3$ (LAGP) and $Li_{3.5}Zn_{0.25}GeO_4$ (LiSICON), are reduced at 2.7 V and 1.4 V, respectively, in agreement with *in situ* XPS experimental studies[18,305,306] (see Fig. 14e and f). In their calculations, Mo *et al.* found that in Ti containing oxide-based SE materials (*i.e.*, LLTO and LATP), Ti^{4+} is reduced to $Ti^{(3-x)+}$ at low potentials, again consistent with the results of *in situ* XPS (see Fig. 14e and f).[299,300] We note that a new method using a Li/SE/SE-carbon cell has been proposed to identify the intrinsic electrochemical stability window of SE materials. The viability of this method was confirmed by the examination of the reduction and oxidation of LGPS and LLZO by a combination of *in situ* XPS and DFT calculations.[303] Among all the oxides investigated, garnet type SEs, in particular, LLZO, exhibit the best resistance to Li reduction.

However, LiPON, as well as sulfides such as Li_3PS_4, and $Li_7P_2S_8I$ (which appears to be better described as Li_4PS_4I),[226] are practically found to be compatible with Li metal. This is due to kinetic factors: the interphase that is formed passivates the SE and mitigates continued reaction. For example, the decomposition products of LiPON, Li_3PS_4, and $Li_7P_2S_8I$ are Li_2O, Li_2S, Li_3P, Li_3N, and LiI, which are all electronically insulating, and thermodynamically stable against Li reduction. The electrochemical potential of Li^+ is constant across the interface. However, due to the poor electronic conductivity of the interphase, the electrochemical potential of the electronic carrier decreases abruptly from the anode to the SE. Therefore, the Li chemical potential (the sum of $\tilde{\mu}_{Li^+}$ and $\tilde{\mu}_{e^-}$) decreases in the interphase layer from the anode to the SE and is within the electrochemical window of the SE. As a result, the decomposition of the SE has no thermodynamic driving force to continue into the bulk and the SE materials are stabilized by the reduction interphase layer. This is the case illustrated by Fig. 14c, above. In contrast, passivation is not possible when the interphase layer is electronically and ionically conductive. The decomposition interphases of Ge-containing LAGP and LiSICON with Li metal, or Ti-containing LLTO and LATP are mixed electronic and ion conductors (see above), which leads to continuous decomposition of the SEs. Thus, the reduction reaction advances into the bulk of the SE (Fig. 14b and g). In the case of sodium SEs much less work has been reported, but in principle sodium SEs exhibit the same thermodynamic instability against Na metal. Janek's group has recently proven the stability of Na-β″-Al_2O_3 against Na metal and the instability of Na_3PS_4 in a combined XPS and impedance study.[307]

The electrochemical stability of many Li-ion solid electrolytes against oxidation with respect to cathode materials has also been investigated by DFT calculations,[10,301] showing that many Li–SEs are thermodynamically unstable at high voltages (Fig. 15a).[10,301] While some oxide-based SEs show a higher reduction potential than sulfides, they also exhibit a much higher oxidation potential, up to 4 V and higher; particularly, NaSICON type materials (*i.e.*, LATP and LAGP) are thermodynamically stable up to 4.2 V. In reality, an even higher nominal oxidation threshold of >5 V is exhibited due to the sluggish kinetics of oxidation and the electronically insulating properties of the decomposition products, which give rise to a significant overpotential. In the case of sulfides, a lower oxidation potential is predicted by calculations, namely, the oxidation of Li_6PS_5Cl and LGPS starts at 2.0 V and 2.15 V, respectively, and Li_3PS_4 exhibits a similar oxidation potential of 2.31 V. Both calculations[308] and experiments[309] show thermodynamically unstability of the interface between sulfide SEs and LCO. The formation of electronically conductive cobalt sulfides are detrimental to the stability of the interface. With the carbon additive in sulfide-based SSBs, the electrochemical decomposition reactions of sulfide SEs at the cathode/SE interface is facilitated by transferring the low chemical potential of lithium in the charged state deeper into the SE and extending the decomposition region.[310] The accumulation of highly oxidized sulfur species at the interface causes a large charge transfer resistance and thereby capacity fading (Fig. 15b).[310] Furthermore, considerable redox activity of sulfide SEs in contact with cathode active materials presents more critical issues at the interface.[311] This sulfide SEs oxidation is verified to occur predominantly in close proximity to the current collector. The thickness of the formed degradation layer is determined by the cut-off voltage and the associated potential drop at the interface between the current collector and the SE.[311]

Fortunately, the better oxidation stability of oxides has enabled engineering of the interface between fast-ion conducting thiophosphate-based solid electrolytes, and positive electrode materials such as lithium transition metal oxides. The reaction between the SE and cathode is hence ameliorated by surface coatings that protect the SE material. Calculations demonstrate that commonly used coating layer materials, including $Li_4Ti_5O_{12}$,[312,313] $LiTaO_3$,[314] $LiNbO_3$,[315,316] Li_2SiO_3,[317] Li_3PO_4,[318] are stable between 2 and 4 V and show low electronic conductivity in this voltage domain (Fig. 15c).[308] These coating materials for cathode materials can act as artificial SEIs to passivate the their surface and extend the electrochemical window, as illustrated in Fig. 15d. The large interfacial resistance that would otherwise arise from solid–solid contact is thus mitigated, contributing to excellent performance of ASSBs.[46]

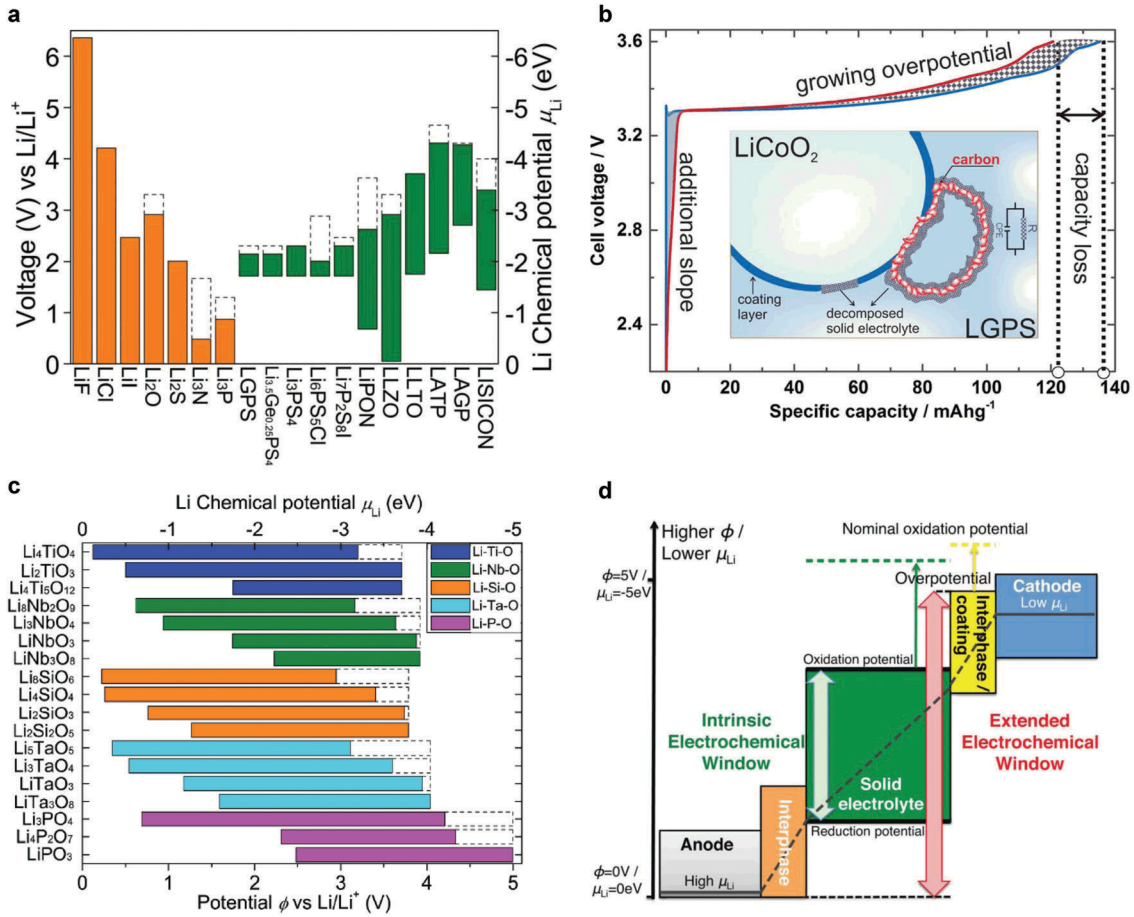

Fig. 15 (a) Electrochemical window (solid color bar) of solid electrolyte and other materials. The oxidation potential to fully delithiate the material is marked by the dashed line.[301] (b) Direct comparison of the first charge curves of carbon-free (blue) and carbon-containing (red) SSBs and a schematic representation of situations that occur on the cathode/SE interface of the SSB during charge processes (insertion). The presence of carbon leads to an additional slope during the first charge. Compared to the case without carbon, a growing overpotential directly results in capacity loss. The presence of carbon facilitates oxidation processes by providing sufficient electronic percolation paths toward the current collector.[310] (c) Electrochemical window of the proposed and previously demonstrated coating layer materials applied between SEs and cathode materials. The dashed line marks the equilibrium voltage to fully delithiate the materials.[308] Reproduced with permission from ref. 308. Copyright (2016), the Royal Society of Chemistry. (d) Schematic diagram illustrating the electrochemical window (color bars) and the Li chemical potential profile (black line) in the solid-state Li-ion battery. The profile of the chemical potential is schematic in this plot and may not be linear. The high μ_{Li} in the anode (silver) and low μ_{Li} in the cathode (blue) are beyond the stability window of the solid electrolyte (green). The observed nominal electrochemical window is extended by the overpotential (dashed line) and by the interphases (orange and yellow), which account for the gap of μ_{Li} between the solid electrolyte and electrodes across the interfaces.[301] Reproduced with permission from ref. 301, 310. Copyright (2015, 2017), American Chemical Society.

6. Conclusions and future prospects for solid electrolytes and solid state batteries

To realize high performance solid-state batteries, solid electrolytes with high Li/Na ion conductivity, good chemical and electrochemical stability against cathode materials are required. If Li metal anodes need to be employed, SEs need also to be stable against reduction or have to be protected by a suitable protecting film. The total conductivity of oxide-based ceramics is highly dependent on the sintering conditions, the dopants, the density of the samples, and the nature of the grain boundaries. Alkali thiophosphate-based conductors show high conductivities ranging from 10^{-3} to 10^{-2} S cm^{-1} even for cold-pressed pellets. However, they must be handled under an ultra-dry atmosphere since most of them are prone to hydrolysis because of their hygroscopic nature. Oxides are typically unstable in contact with Li metal and exhibit slightly lower ion conductivities than sulfides, but are more stable in air and easier to handle. A severe disadvantage of oxide crystalline conductors is their large grain boundary resistance, which is often several orders of magnitude higher than bulk values. Further efforts are needed to decrease this contribution. It should be noted that oxide or phosphate conductors should not contain elements that are easily reduced when in contact with a Li metal anode, such as Ti or Ge. Garnet conductors exhibit both excellent conductivities and high chemical stability, and thus they are thought to be one of the most promising oxide crystalline Li ion conductors. Nevertheless, the preparation of thin-films is necessary to reduce the total ohmic

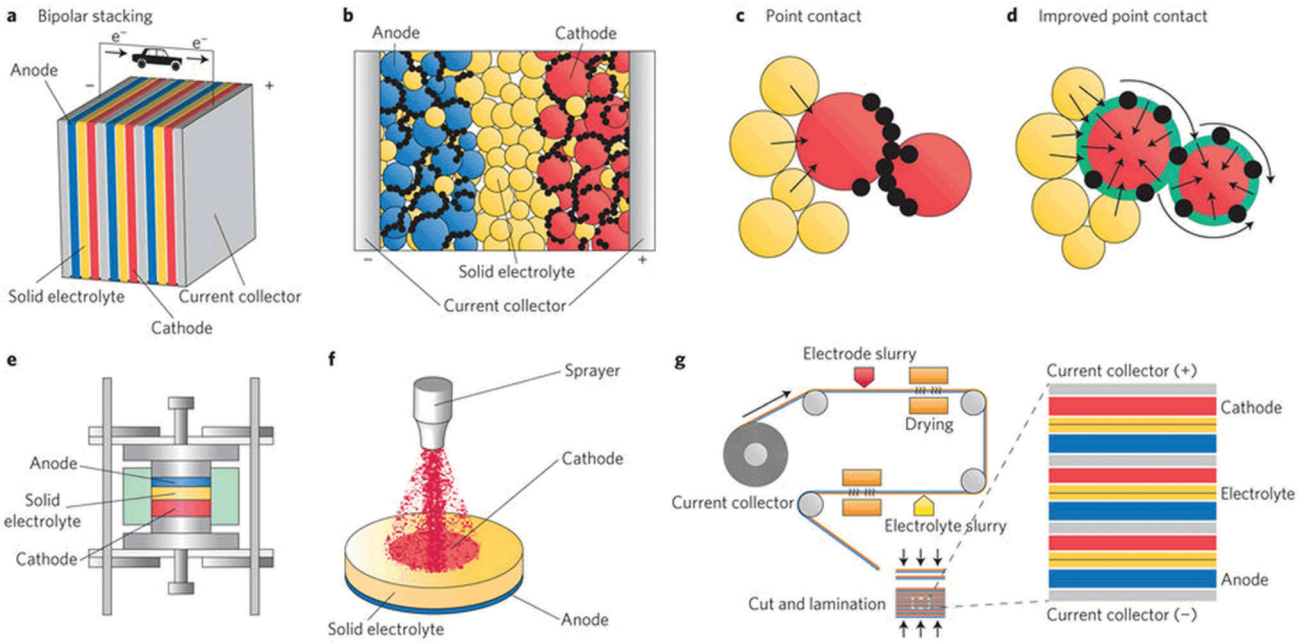

Fig. 16 Configurations of solid-state batteries and fabrication processes for performance improvement. (a) In a bipolar configuration, the electrode materials are coated on the two sides of the current collector, reducing the weight and volume of the battery package. (b) A typical solid-state battery consists of a cathode, an anode and a solid electrolyte. (c) A zoomed-in image of the contact between the electrolyte (yellow spheres) and the electrode (red spheres), which is limited in a typical solid-state battery. The black spheres represent carbon black and the black arrows indicate the Li^+ migration pathway. (d) By putting a mixed conducting network coating (green) on the surface of electrode materials, the electrolyte–electrode contact is enhanced. (e) A powder pressing process for fabricating solid-state batteries. (f) A pasting route analogous to that used in solid oxide fuel cell fabrication. (g) A wet coating process for fabricating solid-state batteries. The electrode slurry is fed into a coating machine and spread on a current collector followed by a drying process and another electrolyte coating process. The obtained electrodes are cut and laminated together to make the solid-state batteries.[319] Reproduced with permission from ref. 319. Copyright (2016), Springer Nature.

resistance of these oxide electrolytes, and ceramic processing of garnets requires high temperatures.

Although the search for solid electrolytes has experienced a recent upsurge, the development of ASSBs is still in its infancy. Compared with conventional liquid batteries, ASSBs can be stacked within a single package by alternating SE and bipolar electrodes (Fig. 16a),[319] thus reducing the weight and volume of the package and increasing the energy density. However, some challenges still remain in the development of ASSBs: the instability of most SE in contact with Li/Na metal; the large interfacial resistance between SE and electrode materials mostly because of the limited contact area (Fig. 16b and c); and the incompatibility between SE and electrodes. The challenges and requirements for the large-scale production of all-solid-state lithium ion and lithium metal batteries are evaluated in a recent review.[320]

To effectively utilize active materials and achieve good rate performance, appropriate techniques are needed to increase the electrode–electrolyte contact area and reduce the interfacial resistance between the electrodes and electrolyte, and allow for sufficient mechanical flexibility during charge/discharge. The mechanochemical preparation of nanocomposite electrodes and the surface modification of active material particles using electrolyte thin-films are effective strategies for achieving a favorable contact between the electrodes and electrolytes and enhancing the energy density of bulk solid-state batteries.[319] One other possible strategy is to form a mixed conducting network into the active material, so as to achieve fast electron conduction and create Li^+ ion transport channels. This conducting network could be an amorphous material or a wetting agent such as a non-flammable ionic liquid (indicated in green in Fig. 16d). As demonstrated in a recent paper, improved interface kinetics can be realized by adding a very small amount of ionic liquid ($PP_{13}FSI$) at the cathode side of the solid-state battery.[252] These solid-state batteries exhibit excellent cycling performance (10 000 cycles at room temperature without capacity decay) and rate capability. Another possible solution is to develop hybrid electrolytes that combine inorganic electrolyte and polymer electrolytes to assemble a flexible all-solid-state battery, as demonstrated by Nan's group.[292,321–323] Obvious solutions that are not fully explored are solid–liquid composites.[288,289]

Another challenge associated with ASSBs is the thickness of the SE layer and the electrode layer, which is determined by the fabrication technology. Well-known cold pressing methods (Fig. 16e), largely used for sulfide based ASSBs, will limit energy density and are difficult to scale up for practical applications. One strategy to reduce the electrode thickness is to spray cathode and anode materials on both sides of the electrolyte (Fig. 16f) by adding small amount of a wetting agent. Another approach is to employ a wet coating process that is widely used in commercial production of conventional batteries (Fig. 16g). This approach has the advantages of controllability of the layer thickness and the scalability, and has been employed to fabricate solid polymer batteries.[324]

Future research should focus on the understanding of interfacial reactions and developing strategies to solve the incompatibility and instability of SE and electrode materials, as well as developing approaches to protect the electrodes and reduce the large resistance of the interface. It is also especially necessary to develop highly scalable methods for SE synthesis.

Conflicts of interest

There are no conflicts to declare.

Acknowledgements

This work was supported by the National Key Technologies R&D Program, China (2016YFB0901500), the National Natural Science Foundation of China (51788104, 51725206 and 51421002). J. J. acknowledges financial support by BMBF within the project ''BenchBatt''. L. F. N. thanks BASF and NSERC for financial support. B. V. L. acknowledges financial support by the BMBF (project ''StickLis''), the Nanosystems Initiative Munich (NIM) and the Max Planck Society. M. A. is indebted to CIC Energigune, Spain, for support. Open Access funding provided by the Max Planck Society.

References

1 M. Armand and J.-M. Tarascon, *Nature*, 2008, **451**, 652–657.
2 B. Dunn, H. Kamath and J.-M. Tarascon, *Science*, 2011, **334**, 928–935.
3 J. B. Goodenough and Y. Kim, *Chem. Mater.*, 2009, **22**, 587–603.
4 J. B. Goodenough, *J. Solid State Electrochem.*, 2012, **16**, 2019–2029.
5 S. Chandrashekar, N. M. Trease, H. J. Chang, L.-S. Du, C. P. Grey and A. Jerschow, *Nat. Mater.*, 2012, **11**, 311–315.
6 W. Xu, J. Wang, F. Ding, X. Chen, E. Nasybulin, Y. Zhang and J.-G. Zhang, *Energy Environ. Sci.*, 2014, **7**, 513–537.
7 J. Janek and W. G. Zeier, *Nat. Mater.*, 2016, **1**, 16141.
8 J. Vetter, P. Novák, M. Wagner, C. Veit, K.-C. Möller, J. Besenhard, M. Winter, M. Wohlfahrt-Mehrens, C. Vogler and A. Hammouche, *J. Power Sources*, 2005, **147**, 269–281.
9 N. J. Dudney, *Lithium batteries*, 2003, ch. 20, pp. 624–642.
10 J. Zhu, X. Hea and Y. Mo, *J. Mater. Chem. A*, 2016, **4**, 3253–3266.
11 Y. Mo, S. P. Ong and G. Ceder, *Chem. Mater.*, 2011, **24**, 15–17.
12 W. Zhang, D. Schröder, T. Arlt, I. Manke, R. Koerver, R. Pinedo, D. A. Weber, J. Sann, W. G. Zeier and J. Janek, *J. Mater. Chem. A*, 2017, **5**, 9929–9936.
13 W. Zhang, D. A. Weber, H. Weigand, T. Arlt, I. Manke, D. Schröder, R. Koerver, T. Leichtweiß, P. Hartmann, W. G. Zeier and J. Janek, *ACS Appl. Mater. Interfaces*, 2017, **9**, 17835–17845.
14 R. Koerver, I. Aygun, T. Leichtweiß, C. Dietrich, W. Zhang, J. Binder, P. Hartmann, W. G. Zeier and J. Janek, *Chem. Mater.*, 2017, **29**, 5574–5582.
15 J. F. Oudenhoven, L. Baggetto and P. H. Notten, *Adv. Energy Mater.*, 2011, **1**, 10–33.
16 K. Xu, *Chem. Rev.*, 2004, **104**, 4303–4418.
17 H. Zhai, P. Xu, M. Ning, Q. Cheng, J. Mandal and Y. Yang, *Nano Lett.*, 2017, **17**, 3182–3187.
18 P. Knauth, *Solid State Ionics*, 2009, **180**, 911–916.
19 J. C. Bachman, S. Muy, A. Grimaud, H.-H. Chang, N. Pour, S. F. Lux, O. Paschos, F. Maglia, S. Lupart, P. Lamp, L. Giordano and Y. Shao-Horn, *Chem. Rev.*, 2015, **116**, 140–162.
20 R. Chen, W. Qu, X. Guo, L. Li and F. Wu, *Mater. Horiz.*, 2016, **3**, 487–516.
21 S. Stramare, V. Thangadurai and W. Weppner, *Chem. Mater.*, 2003, **15**, 3974–3990.
22 V. Thangadurai, S. Narayanan and D. Pinzaru, *Chem. Soc. Rev.*, 2014, **43**, 4714–4727.
23 B. V. Lotsch and J. Maier, *J. Electroceram.*, 2017, **38**, 128–141.
24 Z. Wang, J. Z. Lee, H. L. Xin, L. Han, N. Grillon, D. Guy-Bouyssou, E. Bouyssou, M. Proust and Y. S. Meng, *J. Power Sources*, 2016, **324**, 342–348.
25 Y. Tian, T. Shi, W. D. Richards, J. Li, J. C. Kim, S.-H. Bo and G. Ceder, *Energy Environ. Sci.*, 2017, **10**, 1150–1166.
26 J. Bates, N. Dudney, G. Gruzalski, R. Zuhr, A. Choudhury, C. Luck and J. Robertson, *Solid State Ionics*, 1992, **53**, 647–654.
27 Y. Hamon, A. Douard, F. Sabary, C. Marcel, P. Vinatier, B. Pecquenard and A. Levasseur, *Solid State Ionics*, 2006, **177**, 257–261.
28 S. Jacke, J. Song, L. Dimesso, J. Brötz, D. Becker and W. Jaegermann, *J. Power Sources*, 2011, **196**, 6911–6914.
29 J. Bates, N. Dudney, G. Gruzalski, R. Zuhr, A. Choudhury, C. Luck and J. Robertson, *J. Power Sources*, 1993, **43**, 103–110.
30 B. Fleutot, B. Pecquenard, H. Martinez, M. Letellier and A. Levasseur, *Solid State Ionics*, 2011, **186**, 29–36.
31 N. Suzuki, S. Shirai, N. Takahashi, T. Inaba and T. Shiga, *Solid State Ionics*, 2011, **191**, 49–54.
32 M. Baba, N. Kumagai, N. Fujita, K. Ohta, K. Nishidate, S. Komaba, H. Groult, D. Devilliers and B. Kaplan, *J. Power Sources*, 2001, **97**, 798–800.
33 B. Wang, J. Bates, F. Hart, B. Sales, R. Zuhr and J. Robertson, *J. Electrochem. Soc.*, 1996, **143**, 3203–3213.
34 M. Menetrier, C. Estournes, A. Levasseur and K. Rao, *Solid State Ionics*, 1992, **53**, 1208–1213.
35 R. Mercier, J.-P. Malugani, B. Fahys and G. Robert, *Solid State Ionics*, 1981, **5**, 663–666.
36 H. Wada, M. Menetrier, A. Levasseur and P. Hagenmuller, *Mater. Res. Bull.*, 1983, **18**, 189–193.
37 Y. Ren, Y. Shen, Y. Lin and C.-W. Nan, *Electrochem. Commun.*, 2015, **57**, 27–30.
38 F. Aguesse, W. Manalastas, L. Buannic, J. M. Lopez del Amo, G. Singh, A. Llordés and J. Kilner, *ACS Appl. Mater. Interfaces*, 2017, **9**, 3808–3816.
39 X. Xie, J. Xing, D. Hu, H. Gu, C. Chen and X. Guo, *ACS Appl. Mater. Interfaces*, 2018, **10**, 5978–5983.

40 Y. Seino, T. Ota, K. Takada, A. Hayashi and M. Tatsumisago, *Energy Environ. Sci.*, 2014, **7**, 627–631.
41 Y. Inaguma, C. Liquan, M. Itoh, T. Nakamura, T. Uchida, H. Ikuta and M. Wakihara, *Solid State Commun.*, 1993, **86**, 689–693.
42 R. Kanno and M. Murayama, *J. Electrochem. Soc.*, 2001, **148**, A742–A746.
43 F. Mizuno, A. Hayashi, K. Tadanaga and M. Tatsumisago, *Adv. Mater.*, 2005, **17**, 918–921.
44 K. Takada, N. Aotani and S. Kondo, *J. Power Sources*, 1993, **43**, 135–141.
45 N. Kamaya, K. Homma, Y. Yamakawa, M. Hirayama, R. Kanno, M. Yonemura, T. Kamiyama, Y. Kato, S. Hama and K. Kawamoto, *Nat. Mater.*, 2011, **10**, 682–686.
46 Y. Kato, S. Hori, T. Saito, K. Suzuki, M. Hirayama, A. Mitsui, M. Yonemura, H. Iba and R. Kanno, *Nat. Energy*, 2016, **1**, 16030.
47 Y. Zhao and L. L. Daemen, *J. Am. Chem. Soc.*, 2012, **134**, 15042–15047.
48 K. Minami, A. Hayashi and M. Tatsumisago, *J. Am. Ceram. Soc.*, 2011, **94**, 1779–1783.
49 A. Düvel, A. Kuhn, L. Robben, M. Wilkening and P. Heitjans, *J. Phys. Chem. C*, 2012, **116**, 15192–15202.
50 G. Adachi, N. Imanaka and S. Tamura, *Chem. Rev.*, 2002, **102**, 2405–2430.
51 H.-P. Hong, *Mater. Res. Bull.*, 1978, **13**, 117–124.
52 M. Monchak, T. Hupfer, A. Senyshyn, H. Boysen, D. Chernyshov, T. Hansen, K. G. Schell, E. C. Bucharsky, M. J. Hoffmann and H. Ehrenberg, *Inorg. Chem.*, 2016, **55**, 2941–2945.
53 C. R. Schlaikjer and C. C. Liang, *J. Electrochem. Soc.*, 1971, **118**, 1447–1450.
54 S. Shi, L. Xu, C. Ouyang, Z. Wang and L. Chen, *Ionics*, 2006, **12**, 343–347.
55 G. Adachi, N. Imanaka and H. Aono, *Adv. Mater.*, 1996, **8**, 127–135.
56 A. Robertson, A. West and A. Ritchie, *Solid State Ionics*, 1997, **104**, 1–11.
57 A. G. Belous, G. N. Novitskaya, S. V. Polyanetskaya and Y. I. Gornikov, *Russ. J. Inorg. Chem.*, 1987, **32**, 156–157.
58 M. Wu, Z. Wen, Y. Liu, X. Wang and L. Huang, *J. Power Sources*, 2011, **196**, 8091–8097.
59 S. J. Visco, Y. S. Nimon and B. D. Katz, US8778522 B2, 2014.
60 M. Braga, J. A. Ferreira, V. Stockhausen, J. Oliveira and A. El-Azab, *J. Mater. Chem. A*, 2014, **2**, 5470–5480.
61 R. Kanno, T. Hata, Y. Kawamoto and M. Irie, *Solid State Ionics*, 2000, **130**, 97–104.
62 H. J. Deiseroth, S. T. Kong, H. Eckert, J. Vannahme, C. Reiner, T. Zaiss and M. Schlosser, *Angew. Chem., Int. Ed.*, 2008, **47**, 755–758.
63 P. Bron, S. Johansson, K. Zick, J. r. Schmedt auf der Günne, S. Dehnen and B. Roling, *J. Am. Chem. Soc.*, 2013, **135**, 15694–15697.
64 O. Bohnke, C. Bohnke and J. Fourquet, *Solid State Ionics*, 1996, **91**, 21–31.
65 M. Abe and K. Uchino, *Mater. Res. Bull.*, 1974, **9**, 147–155.
66 Y. Inaguma, T. Katsumata, M. Itoh and Y. Morii, *J. Solid State Chem.*, 2002, **166**, 67–72.
67 M. Yashima, M. Itoh, Y. Inaguma and Y. Morii, *J. Am. Chem. Soc.*, 2005, **127**, 3491–3495.
68 J. Ibarra, A. Varez, C. León, J. Santamarıa, L. Torres-Martınez and J. Sanz, *Solid State Ionics*, 2000, **134**, 219–228.
69 Y. Zou and N. Inoue, *Ionics*, 2005, **11**, 333–342.
70 J. Fourquet, H. Duroy and M. Crosnier-Lopez, *J. Solid State Chem.*, 1996, **127**, 283–294.
71 Y. Inaguma, T. Katsumata, M. Itoh, Y. Morii and T. Tsurui, *Solid State Ionics*, 2006, **177**, 3037–3044.
72 A. Morata-Orrantia, S. García-Martín and M. Á. Alario-Franco, *Chem. Mater.*, 2003, **15**, 363–367.
73 O. Bohnke, C. Bohnke, J. Ould Sid'Ahmed, M. Crosnier-Lopez, H. Duroy, F. Le Berre and J. Fourquet, *Chem. Mater.*, 2001, **13**, 1593–1599.
74 L. He and H. Yoo, *Electrochim. Acta*, 2003, **48**, 1357–1366.
75 V. Thangadurai and W. Weppner, *Ionics*, 2000, **6**, 70–77.
76 A. Morata-Orrantia, S. García-Martín, E. Morán and M. Á. Alario-Franco, *Chem. Mater.*, 2002, **14**, 2871–2875.
77 H.-T. Chung, J.-G. Kim and H.-G. Kim, *Solid State Ionics*, 1998, **107**, 153–160.
78 A. Kishimoto, *Solid State Ionics*, 1998, **107**, 153–160.
79 T. Teranishi, M. Yamamoto, H. Hayashi and A. Kishimoto, *Solid State Ionics*, 2013, **243**, 18–21.
80 H. Kawai and J. Kuwano, *J. Electrochem. Soc.*, 1994, **141**, L78–L79.
81 Y. Harada, T. Ishigaki, H. Kawai and J. Kuwano, *Solid State Ionics*, 1998, **108**, 407–413.
82 M. Nakayama, T. Usui, Y. Uchimoto, M. Wakihara and M. Yamamoto, *J. Phys. Chem. B*, 2005, **109**, 4135–4143.
83 K.-Y. Yang, J.-W. Wang and K.-Z. Fung, *J. Alloys Compd.*, 2008, **458**, 415–424.
84 A. Mei, X.-L. Wang, J.-L. Lan, Y.-C. Feng, H.-X. Geng, Y.-H. Lin and C.-W. Nan, *Electrochim. Acta*, 2010, **55**, 2958–2963.
85 H. Geng, J. Lan, A. Mei, Y. Lin and C. Nan, *Electrochim. Acta*, 2011, **56**, 3406–3414.
86 X. Gao, C. A. Fisher, T. Kimura, Y. H. Ikuhara, H. Moriwake, A. Kuwabara, H. Oki, T. Tojigamori, R. Huang and Y. Ikuhara, *Chem. Mater.*, 2013, **25**, 1607–1614.
87 X. Gao, C. A. Fisher, T. Kimura, Y. H. Ikuhara, A. Kuwabara, H. Moriwake, H. Oki, T. Tojigamori, K. Kohama and Y. Ikuhara, *J. Mater. Chem. A*, 2014, **2**, 843–852.
88 C. Ma, K. Chen, C. Liang, C.-W. Nan, R. Ishikawa, K. More and M. Chi, *Energy Environ. Sci.*, 2014, **7**, 1638–1642.
89 H. Moriwake, X. Gao, A. Kuwabara, C. A. Fisher, T. Kimura, Y. H. Ikuhara, K. Kohama, T. Tojigamori and Y. Ikuhara, *J. Power Sources*, 2015, **276**, 203–207.
90 W. J. Kwon, H. Kim, K.-N. Jung, W. Cho, S. H. Kim, J.-W. Lee and M.-S. Park, *J. Mater. Chem. A*, 2017, **5**, 6257–6262.
91 K. Chen, M. Huang, Y. Shen, Y. Lin and C. Nan, *Solid State Ionics*, 2013, **235**, 8–13.
92 A. Mei, X.-L. Wang, Y.-C. Feng, S.-J. Zhao, G.-J. Li, H.-X. Geng, Y.-H. Lin and C.-W. Nan, *Solid State Ionics*, 2008, **179**, 2255–2259.

93 H. Zhang, X. Liu, Y. Qi and V. Liu, *J. Alloys Compd.*, 2013, **577**, 57–63.
94 Y. Deng, S.-J. Shang, A. Mei, Y.-H. Lin, L.-Y. Liu and C.-W. Nan, *J. Alloys Compd.*, 2009, **472**, 456–460.
95 A. Yoshiasa, D. Sakamoto, H. Okudera, M. Sugahara, K. i. Ota and A. Nakatsuka, *Z. Anorg. Allg. Chem.*, 2005, **631**, 502–506.
96 C. D. Martin, S. Chaudhur, C. P. Grey and J. B. Parise, *Am. Mineral.*, 2005, **90**, 1522–1533.
97 V. Bouznik, Y. N. Moskvich and V. N. Voronov, *Chem. Phys. Lett.*, 1976, **37**, 464–467.
98 Y. Zhang, Y. Zhao and C. Chen, *Phys. Rev. B: Condens. Matter Mater. Phys.*, 2013, **87**, 134303.
99 Y. Wang, W. D. Richards, S. P. Ong, L. J. Miara, J. C. Kim, Y. Mo and G. Ceder, *Nat. Mater.*, 2015, **14**, 1026–1031.
100 A. Emly, E. Kioupakis and A. Van der Ven, *Chem. Mater.*, 2013, **25**, 4663–4670.
101 R. Mouta, M. A. B. Melo, E. M. Diniz and C. W. A. Paschoal, *Chem. Mater.*, 2014, **26**, 7137–7144.
102 J. A. Dawson, P. Canepa, T. Famprikis, C. Masquelier and M. S. Islam, *J. Am. Chem. Soc.*, 2017, **140**, 362–368.
103 Y. Li, W. Zhou, S. Xin, S. Li, J. Zhu, X. Lu, Z. Cui, Q. Jia, J. Zhou, Y. Zhao and J. B. Goodenough, *Angew. Chem., Int. Ed.*, 2016, **55**, 9965–9968.
104 M. H. Braga, N. S. Grundish, A. J. Murchison and J. B. Goodenough, *Energy Environ. Sci.*, 2017, **10**, 331–336.
105 M. H. Braga, A. J. Murchison, J. A. Ferreira, P. Singh and J. B. Goodenough, *Energy Environ. Sci.*, 2016, **9**, 948–954.
106 J. Goodenough, H.-P. Hong and J. Kafalas, *Mater. Res. Bull.*, 1976, **11**, 203–220.
107 H.-P. Hong, *Mater. Res. Bull.*, 1976, **11**, 173–182.
108 K. Arbi, M. París and J. Sanz, *Dalton Trans.*, 2011, **40**, 10195–10202.
109 M. A. París and J. Sanz, *Phys. Rev. B: Condens. Matter Mater. Phys.*, 1997, **55**, 14270.
110 E. Morin, T. Le Mercier, M. Quarton, E. Losilla, M. Aranda and S. Bruque, *Powder Diffr.*, 1999, **14**, 53–60.
111 M. Weiss, D. A. Weber, A. Senyshyn, J. Janek and W. G. Zeier, *ACS Appl. Mater. Interfaces*, 2018, **10**, 10935–10944.
112 M. Alami, R. Brochu, J. Soubeyroux, P. Gravereau, G. Le Flem and P. Hagenmuller, *J. Solid State Chem.*, 1991, **90**, 185–193.
113 M. A. París, A. Martínez-Juárez, J. M. Rojo and J. Sanz, *J. Phys.: Condens. Matter*, 1996, **8**, 5355–5366.
114 E. R. Losilla, M. A. Aranda, M. Martínez-Lara and S. Bruque, *Chem. Mater.*, 1997, **9**, 1678–1685.
115 K. Arbi, S. Mandal, J. M. Rojo and J. Sanz, *Chem. Mater.*, 2002, **14**, 1091–1097.
116 M. Catti, S. Stramare and R. Ibberson, *Solid State Ionics*, 1999, **123**, 173–180.
117 Y. Zhang, K. Chen, Y. Shen, Y. Lin and C.-W. Nan, *Ceram. Int.*, 2017, **43**, S598–S602.
118 M. Giarola, A. Sanson, F. Tietz, S. Pristat, E. Dashjav, D. Rettenwander, G. n. J. Redhammer and G. Mariotto, *J. Phys. Chem. C*, 2017, **121**, 3697–3706.
119 H. Aono, E. Sugimoto, Y. Sadaoka, N. Imanaka and G. Adachi, *J. Electrochem. Soc.*, 1993, **140**, 1827–1833.
120 K. Thomas, G. Subba Rao, K. Radhakrishnan and B. Chowdari, *Mater. Res. Bull.*, 1989, **24**, 221–229.
121 R. Shannon, B. Taylor, A. English and T. Berzins, *Electrochim. Acta*, 1977, **22**, 783–796.
122 D. T. Qui, S. Hamdoune, J. Soubeyroux and E. Prince, *J. Solid State Chem.*, 1988, **72**, 309–315.
123 H. Aono, E. Sugimoto, Y. Sadaoka, N. Imanaka and G. y. Adachi, *J. Electrochem. Soc.*, 1990, **137**, 1023–1027.
124 K. Ado, Y. Saito, T. Asai, H. Kageyama and O. Nakamura, *Solid State Ionics*, 1992, **53**, 723–727.
125 A. Best, M. Forsyth and D. MacFarlane, *Solid State Ionics*, 2000, **136**, 339–344.
126 K. Arbi, M. Lazarraga, D. Ben Hassen Chehimi, M. Ayadi-Trabelsi, J. Rojo and J. Sanz, *Chem. Mater.*, 2004, **16**, 255–262.
127 T. Šalkus, M. Barre, A. Kežionis, E. Kazakevičius, O. Bohnke, A. Selskienė and A. Orliukas, *Solid State Ionics*, 2012, **225**, 615–619.
128 K. Arbi, M. Hoelzel, A. Kuhn, F. García-Alvarado and J. Sanz, *Inorg. Chem.*, 2013, **52**, 9290–9296.
129 M. Pérez-Estébanez, J. Isasi-Marín, D. Többens, A. Rivera-Calzada and C. León, *Solid State Ionics*, 2014, **266**, 1–8.
130 K. Arbi, R. Jimenez, T. Šalkus, A. Orliukas and J. Sanz, *Solid State Ionics*, 2015, **271**, 28–33.
131 C. Vinod Chandran, S. Pristat, E. Witt, F. Tietz and P. Heitjans, *J. Phys. Chem. C*, 2016, **120**, 8436–8442.
132 H. Aono, E. Sugimoto, Y. Sadaoka, N. Imanaka and G.-y. Adachi, *Bull. Chem. Soc. Jpn.*, 1992, **65**, 2200–2204.
133 B. Lang, B. Ziebarth and C. Elsässer, *Chem. Mater.*, 2015, **27**, 5040–5048.
134 R. Kahlaoui, K. Arbi, I. Sobrados, R. Jimenez, J. Sanz and R. Ternane, *Inorg. Chem.*, 2017, **56**, 1216–1224.
135 H. Aono, E. Sugimoto, Y. Sadaaka, N. Imanaka and G. Adachi, *J. Electrochem. Soc.*, 1989, **136**, 590–591.
136 Y. Kobayashi, M. Tabuchi and O. Nakamura, *J. Power Sources*, 1997, **68**, 407–411.
137 H. Aono, E. Sugimoto, Y. Sadaoka, N. Imanaka and G.-y. Adachi, *Solid State Ionics*, 1991, **47**, 257–264.
138 L. Xiong, Z. Ren, Y. Xu, S. Mao, P. Lei and M. Sun, *Solid State Ionics*, 2017, **309**, 22–26.
139 J. Fu, *Solid State Ionics*, 1997, **96**, 195–200.
140 J. Fu, *Solid State Ionics*, 1997, **104**, 191–194.
141 B. Chowdari, G. S. Rao and G. Lee, *Solid State Ionics*, 2000, **136**, 1067–1075.
142 J. S. Thokchom and B. Kumar, *Solid State Ionics*, 2006, **177**, 727–732.
143 J. S. Thokchom and B. Kumar, *J. Am. Ceram. Soc.*, 2007, **90**, 462–466.
144 J. S. Thokchom and B. Kumar, *J. Power Sources*, 2008, **185**, 480–485.
145 J. S. Thokchom and B. Kumar, *J. Power Sources*, 2010, **195**, 2870–2876.
146 C. R. Mariappan, C. Yada, F. Rosciano and B. Roling, *J. Power Sources*, 2011, **196**, 6456–6464.
147 V. Thangadurai, H. Kaack and W. J. Weppner, *J. Am. Ceram. Soc.*, 2003, **86**, 437–440.

148 V. Thangadurai and W. Weppner, *J. Solid State Chem.*, 2006, **179**, 974–984.
149 S. Narayanan, F. Ramezanipour and V. Thangadurai, *J. Phys. Chem. C*, 2012, **116**, 20154–20162.
150 V. Thangadurai and W. Weppner, *J. Am. Ceram. Soc.*, 2005, **88**, 411–418.
151 V. Thangadurai and W. Weppner, *Adv. Funct. Mater.*, 2005, **15**, 107–112.
152 J. Percival, E. Kendrick and P. Slater, *Mater. Res. Bull.*, 2008, **43**, 765–770.
153 J. Percival, E. Kendrick and P. Slater, *Solid State Ionics*, 2008, **179**, 1666–1669.
154 R. Murugan, V. Thangadurai and W. Weppner, *Angew. Chem., Int. Ed.*, 2007, **46**, 7778–7781.
155 J. Tan and A. Tiwari, *Electrochem. Solid-State Lett.*, 2011, **15**, A37–A39.
156 J. Percival, E. Kendrick, R. Smith and P. Slater, *Dalton Trans.*, 2009, 5177–5181.
157 J. Awaka, N. Kijima, K. Kataoka, H. Hayakawa, K.-i. Ohshima and J. Akimoto, *J. Solid State Chem.*, 2010, **183**, 180–185.
158 R. Jalem, Y. Yamamoto, H. Shiiba, M. Nakayama, H. Munakata, T. Kasuga and K. Kanamura, *Chem. Mater.*, 2013, **25**, 425–430.
159 J. Awaka, N. Kijima, H. Hayakawa and J. Akimoto, *J. Solid State Chem.*, 2009, **182**, 2046–2052.
160 H. Buschmann, J. Dölle, S. Berendts, A. Kuhn, P. Bottke, M. Wilkening, P. Heitjans, A. Senyshyn, H. Ehrenberg and A. Lotnyk, *Phys. Chem. Chem. Phys.*, 2011, **13**, 19378–19392.
161 C. A. Geiger, E. Alekseev, B. Lazic, M. Fisch, T. Armbruster, R. Langner, M. Fechtelkord, N. Kim, T. Pettke and W. Weppner, *Inorg. Chem.*, 2010, **50**, 1089–1097.
162 Y. Li, J.-T. Han, C.-A. Wang, S. C. Vogel, H. Xie, M. Xu and J. B. Goodenough, *J. Power Sources*, 2012, **209**, 278–281.
163 A. A. Hubaud, D. J. Schroeder, B. Key, B. J. Ingram, F. Dogan and J. T. Vaughey, *J. Mater. Chem. A*, 2013, **1**, 8813–8818.
164 E. Rangasamy, J. Wolfenstine and J. Sakamoto, *Solid State Ionics*, 2012, **206**, 28–32.
165 D. Rettenwander, P. Blaha, R. Laskowski, K. Schwarz, P. Bottke, M. Wilkening, C. A. Geiger and G. Amthauer, *Chem. Mater.*, 2014, **26**, 2617–2623.
166 N. Bernstein, M. Johannes and K. Hoang, *Phys. Rev. Lett.*, 2012, **109**, 205702.
167 M. Kotobuki, K. Kanamura, Y. Sato and T. Yoshida, *J. Power Sources*, 2011, **196**, 7750–7754.
168 S. Kumazaki, Y. Iriyama, K.-H. Kim, R. Murugan, K. Tanabe, K. Yamamoto, T. Hirayama and Z. Ogumi, *Electrochem. Commun.*, 2011, **13**, 509–512.
169 J. Wolfenstine, J. Ratchford, E. Rangasamy, J. Sakamoto and J. L. Allen, *Mater. Chem. Phys.*, 2012, **134**, 571–575.
170 R. Jalem, M. Rushton, W. Manalastas Jr, M. Nakayama, T. Kasuga, J. A. Kilner and R. W. Grimes, *Chem. Mater.*, 2015, **27**, 2821–2831.
171 C. Bernuy-Lopez, W. Manalastas Jr, J. M. Lopez del Amo, A. Aguadero, F. Aguesse and J. A. Kilner, *Chem. Mater.*, 2014, **26**, 3610–3617.
172 H. El Shinawi and J. Janek, *J. Power Sources*, 2013, **225**, 13–19.
173 M. Howard, O. Clemens, E. Kendrick, K. Knight, D. Apperley, P. Anderson and P. Slater, *Dalton Trans.*, 2012, **41**, 12048–12053.
174 D. Rettenwander, C. A. Geiger, M. Tribus, P. Tropper and G. Amthauer, *Inorg. Chem.*, 2014, **53**, 6264–6269.
175 S. Ramakumar, L. Satyanarayana, S. V. Manorama and R. Murugan, *Phys. Chem. Chem. Phys.*, 2013, **15**, 11327–11338.
176 S. Ohta, T. Kobayashi and T. Asaoka, *J. Power Sources*, 2011, **196**, 3342–3345.
177 Y. Li, J.-T. Han, C.-A. Wang, H. Xie and J. B. Goodenough, *J. Mater. Chem.*, 2012, **22**, 15357–15361.
178 C. Deviannapoorani, L. Dhivya, S. Ramakumar and R. Murugan, *J. Power Sources*, 2013, **240**, 18–25.
179 D. Wang, G. Zhong, W. K. Pang, Z. Guo, Y. Li, M. J. McDonald, R. Fu, J.-X. Mi and Y. Yang, *Chem. Mater.*, 2015, **27**, 6650–6659.
180 D. Wang, G. Zhong, O. Dolotko, Y. Li, M. J. McDonald, J. Mi, R. Fu and Y. Yang, *J. Mater. Chem. A*, 2014, **2**, 20271–20279.
181 L. Dhivya and R. Murugan, *ACS Appl. Mater. Interfaces*, 2014, **6**, 17606–17615.
182 X. Tong, V. Thangadurai and E. D. Wachsman, *Inorg. Chem.*, 2015, **54**, 3600–3607.
183 A. Raskovalov, E. Il'ina and B. Antonov, *J. Power Sources*, 2013, **238**, 48–52.
184 R. Murugan, S. Ramakumar and N. Janani, *Electrochem. Commun.*, 2011, **13**, 1373–1375.
185 Y. Wang and W. Lai, *Electrochem. Solid-State Lett.*, 2012, **15**, A68–A71.
186 M. P. O'Callaghan, D. R. Lynham, E. J. Cussen and G. Z. Chen, *Chem. Mater.*, 2006, **18**, 4681–4689.
187 R.-J. Chen, M. Huang, W.-Z. Huang, Y. Shen, Y.-H. Lin and C.-W. Nan, *Solid State Ionics*, 2014, **265**, 7–12.
188 T. Thompson, J. Wolfenstine, J. L. Allen, M. Johannes, A. Huq, I. N. David and J. Sakamoto, *J. Mater. Chem. A*, 2014, **2**, 13431–13436.
189 R. Inada, K. Kusakabe, T. Tanaka, S. Kudo and Y. Sakurai, *Solid State Ionics*, 2014, **262**, 568–572.
190 D. Mazza, *Mater. Lett.*, 1988, **7**, 205–207.
191 H. Hyooma and K. Hayashi, *Mater. Res. Bull.*, 1988, **23**, 1399–1407.
192 V. Thangadurai, S. Adams and W. Weppner, *Chem. Mater.*, 2004, **16**, 2998–3006.
193 E. J. Cussen, *Chem. Commun.*, 2006, 412–413.
194 L. van Wüllen, T. Echelmeyer, H.-W. Meyer and D. Wilmer, *Phys. Chem. Chem. Phys.*, 2007, **9**, 3298–3303.
195 M. P. O'Callaghan and E. J. Cussen, *Chem. Commun.*, 2007, 2048–2050.
196 M. Xu, M. S. Park, J. M. Lee, T. Y. Kim, Y. S. Park and E. Ma, *Phys. Rev. B: Condens. Matter Mater. Phys.*, 2012, **85**, 052301.
197 J. Han, J. Zhu, Y. Li, X. Yu, S. Wang, G. Wu, H. Xie, S. C. Vogel, F. Izumi and K. Momma, *Chem. Commun.*, 2012, **48**, 9840–9842.
198 A. Hayashi, K. Noi, A. Sakuda and M. Tatsumisago, *Nat. Commun.*, 2012, **3**, 856.

199 A. Hayashi, A. Sakuda and M. Tatsumisago, *Front. Energy Res.*, 2016, **4**, 25.
200 M. Murayama, R. Kanno, M. Irie, S. Ito, T. Hata, N. Sonoyama and Y. Kawamoto, *J. Solid State Chem.*, 2002, **168**, 140–148.
201 Z. Liu, W. Fu, E. A. Payzant, X. Yu, Z. Wu, N. J. Dudney, J. Kiggans, K. Hong, A. J. Rondinone and C. Liang, *J. Am. Chem. Soc.*, 2013, **135**, 975–978.
202 Z. Liu, F. Huang, J. Yang, B. Wang and J. Sun, *Solid State Ionics*, 2008, **179**, 1714–1716.
203 M. Tachez, J.-P. Malugani, R. Mercier and G. Robert, *Solid State Ionics*, 1984, **14**, 181–185.
204 B. T. Ahn and R. A. Huggins, *Mater. Res. Bull.*, 1989, **24**, 889–897.
205 H. Yamane, M. Shibata, Y. Shimane, T. Junke, Y. Seino, S. Adams, K. Minami, A. Hayashi and M. Tatsumisago, *Solid State Ionics*, 2007, **178**, 1163–1167.
206 T. Kaib, S. Haddadpour, M. Kapitein, P. Bron, C. Schröder, H. Eckert, B. Roling and S. Dehnen, *Chem. Mater.*, 2012, **24**, 2211–2219.
207 C. Dietrich, M. Sadowski, S. Sicolo, D. A. Weber, S. J. Sedlmaier, K. S. Weldert, S. Indris, K. Albe, J. Janek and W. G. Zeier, *Chem. Mater.*, 2016, **28**, 8764–8773.
208 J. M. Whiteley, J. H. Woo, E. Hu, K.-W. Nam and S.-H. Lee, *J. Electrochem. Soc.*, 2014, **161**, A1812–A1817.
209 Y. Kato, R. Saito, M. Sakano, A. Mitsui, M. Hirayama and R. Kanno, *J. Power Sources*, 2014, **271**, 60–64.
210 M. R. Busche, D. A. Weber, Y. Schneider, C. Dietrich, S. Wenzel, T. Leichtweiss, D. Schröder, W. Zhang, H. Weigand and D. Walter, *Chem. Mater.*, 2016, **28**, 6152–6165.
211 C. Dietrich, D. A. Weber, S. J. Sedlmaier, S. Indris, S. P. Culver, D. Walter, J. Janek and W. G. Zeier, *J. Mater. Chem. A*, 2017, **5**, 18111–18119.
212 Y. Kato, K. Kawamoto, R. Kanno and M. Hirayama, *Electrochemistry*, 2012, **80**, 749–751.
213 S. Wenzel, S. Randau, T. Leichtweiß, D. A. Weber, J. Sann, W. G. Zeier and J. Janek, *Chem. Mater.*, 2016, **28**, 2400–2407.
214 S. P. Ong, Y. Mo, W. D. Richards, L. Miara, H. S. Lee and G. Ceder, *Energy Environ. Sci.*, 2013, **6**, 148–156.
215 A. Kuhn, O. Gerbig, C. Zhu, F. Falkenberg, J. Maier and B. V. Lotsch, *Phys. Chem. Chem. Phys.*, 2014, **16**, 14669–14674.
216 Y. Sun, K. Suzuki, S. Hori, M. Hirayama and R. Kanno, *Chem. Mater.*, 2017, **29**, 5858–5864.
217 T. Krauskopf, S. P. Culver and W. G. Zeier, *Chem. Mater.*, 2018, **30**, 1791–1798.
218 S. Adams and R. P. Rao, *J. Mater. Chem.*, 2012, **22**, 7687–7691.
219 A. Kuhn, J. Köhler and B. V. Lotsch, *Phys. Chem. Chem. Phys.*, 2013, **15**, 11620–11622.
220 D. A. Weber, A. Senyshyn, K. S. Weldert, S. Wenzel, W. Zhang, R. Kaiser, S. Berendts, J. Janek and W. G. Zeier, *Chem. Mater.*, 2016, **28**, 5905–5915.
221 H. J. Deiseroth, J. Maier, K. Weichert, V. Nickel, S. T. Kong and C. Reiner, *Z. Anorg. Allg. Chem.*, 2011, **637**, 1287–1294.
222 N. J. de Klerk, I. Rosłoń and M. Wagemaker, *Chem. Mater.*, 2016, **28**, 7955–7963.
223 H. M. Chen, C. Maohua and S. Adams, *Phys. Chem. Chem. Phys.*, 2015, **17**, 16494–16506.
224 M. A. Kraft, S. P. Culver, M. Calderon, F. Böcher, T. Krauskopf, A. Senyshyn, C. Dietrich, A. Zevalkink, J. Janek and W. G. Zeier, *J. Am. Chem. Soc.*, 2017, **139**, 10909–10918.
225 N. Minafra, S. P. Culver, T. Krauskopf, A. Senyshyn and W. G. Zeier, *J. Mater. Chem. A*, 2018, **6**, 645–651.
226 S. J. Sedlmaier, S. Indris, C. Dietrich, M. Yavuz, C. Dräger, F. von Seggern, H. Sommer and J. Janek, *Chem. Mater.*, 2017, **29**, 1830–1835.
227 S. Sicolo, C. Kalcher, S. J. Sedlmaier, J. Janek and K. Albe, *Solid State Ionics*, 2018, **319**, 83–91.
228 W. D. Richards, Y. Wang, L. J. Miara, J. C. Kim and G. Ceder, *Energy Environ. Sci.*, 2016, **9**, 3272–3278.
229 K. Kaup, F. Lalere, A. Huq, A. Shyamsunder, T. Adermann, P. Hartmann and L. F. Nazar, *Chem. Mater.*, 2018, **30**, 592–596.
230 A. Kuhn, T. Holzmann, J. Nuss and B. V. Lotsch, *J. Mater. Chem. A*, 2014, **2**, 6100–6106.
231 J. A. Brant, D. M. Massi, N. Holzwarth, J. H. MacNeil, A. P. Douvalis, T. Bakas, S. W. Martin, M. D. Gross and J. A. Aitken, *Chem. Mater.*, 2014, **27**, 189–196.
232 T. Holzmann, L. Schoop, M. Ali, I. Moudrakovski, G. Gregori, J. Maier, R. Cava and B. Lotsch, *Energy Environ. Sci.*, 2016, **9**, 2578–2585.
233 H. Pan, Y.-S. Hu and L. Chen, *Energy Environ. Sci.*, 2013, **6**, 2338–2360.
234 L. Mu, S. Xu, Y. Li, Y. S. Hu, H. Li, L. Chen and X. Huang, *Adv. Mater.*, 2015, **27**, 6928–6933.
235 Y. Li, Y.-S. Hu, X. Qi, X. Rong, H. Li, X. Huang and L. Chen, *Energy Storage Materials*, 2016, **5**, 191–197.
236 K. B. Hueso, M. Armand and T. Rojo, *Energy Environ. Sci.*, 2013, **6**, 734–749.
237 J. B. Goodenough, H.-P. Hong and J. A. Kafalas, *Mater. Res. Bull.*, 1976, **11**, 203–220.
238 N. Anantharamulu, K. K. Rao, G. Rambabu, B. V. Kumar, V. Radha and M. Vithal, *J. Mater. Sci.*, 2011, **46**, 2821–2837.
239 K.-D. Kreuer, H. Kohler and J. Maier, *High Conductivity Solid Ionic Conductors: Recent Trends and Applications*, World Scientific, 1989, pp. 242–279.
240 E. Vogel, R. Cava and E. Rietman, *Solid State Ionics*, 1984, **14**, 1–6.
241 T. Takahashi, K. Kuwabara and M. Shibata, *Solid State Ionics*, 1980, **1**, 163–175.
242 F. Krok, D. Kony, J. Dygas, W. Jakubowski and W. Bogusz, *Solid State Ionics*, 1989, **36**, 251–254.
243 Z. Khakpour, *Electrochim. Acta*, 2016, **196**, 337–347.
244 A. Kuriakose, T. Wheat, A. Ahmad and J. Dirocco, *J. Am. Ceram. Soc.*, 1984, **67**, 179–183.
245 B. McEntire, R. Bartlett, G. Miller and R. Gordon, *J. Am. Ceram. Soc.*, 1983, **66**, 738–742.
246 J. S. Lee, C. M. Chang, Y. I. Lee, J. H. Lee and S. H. Hong, *J. Am. Ceram. Soc.*, 2004, **87**, 305–307.
247 R. Fuentes, F. Figueiredo, F. Marques and J. Franco, *Ionics*, 2002, **8**, 383–390.

248 S.-M. Lee, S.-T. Lee, D.-H. Lee, S.-H. Lee, S.-S. Han and S.-K. Lim, *J. Ceram. Process. Res.*, 2015, **16**, 49–53.
249 Q. Ma, M. Guin, S. Naqash, C.-L. Tsai, F. Tietz and O. Guillon, *Chem. Mater.*, 2016, **28**, 4821–4828.
250 M. Guin and F. Tietz, *J. Power Sources*, 2015, **273**, 1056–1064.
251 A. G. Jolley, D. D. Taylor, N. J. Schreiber and E. D. Wachsman, *J. Am. Ceram. Soc.*, 2015, **98**, 2902–2907.
252 Z. Zhang, Q. Zhang, J. Shi, Y. S. Chu, X. Yu, K. Xu, M. Ge, H. Yan, W. Li and L. Gu, *Adv. Energy Mater.*, 2017, **7**, 1101196.
253 U. Warhus, J. Maier and A. Rabenau, *J. Solid State Chem.*, 1988, **72**, 113–125.
254 K. Kreuer and U. Warhus, *Mater. Res. Bull.*, 1986, **21**, 357–363.
255 M. Tatsumisago, M. Nagao and A. Hayashi, *J. Asian Ceram. Soc.*, 2013, **1**, 17–25.
256 M. Jansen and U. Henseler, *J. Solid State Chem.*, 1992, **99**, 110–119.
257 T. Krauskopf, S. P. Culver and W. G. Zeier, *Inorg. Chem.*, 2018, **57**, 4739–4744.
258 Z. Zhu, I.-H. Chu, Z. Deng and S. P. Ong, *Chem. Mater.*, 2015, **27**, 8318–8325.
259 S.-H. Bo, Y. Wang and G. Ceder, *J. Mater. Chem. A*, 2016, **4**, 9044–9053.
260 I.-H. Chu, C. S. Kompella, H. Nguyen, Z. Zhu, S. Hy, Z. Deng, Y. S. Meng and S. P. Ong, *Sci. Rep.*, 2016, **6**, 33733.
261 L. Zhang, K. Yang, J. Mi, L. Lu, L. Zhao, L. Wang, Y. Li and H. Zeng, *Adv. Energy Mater.*, 2015, **5**, 1501294.
262 A. Banerjee, K. H. Park, J. W. Heo, Y. J. Nam, C. K. Moon, S. M. Oh, S. T. Hong and Y. S. Jung, *Angew. Chem., Int. Ed.*, 2016, **128**, 9786–9790.
263 H. Wang, Y. Chen, Z. D. Hood, G. Sahu, A. S. Pandian, J. K. Keum, K. An and C. Liang, *Angew. Chem., Int. Ed.*, 2016, **55**, 8551–8555.
264 L. Zhang, D. Zhang, K. Yang, X. Yan, L. Wang, J. Mi, B. Xu and Y. Li, *Adv. Sci.*, 2016, **3**, 1600089.
265 N. Wang, K. Yang, L. Zhang, X. Yan, L. Wang and B. Xu, *J. Mater. Sci.*, 2018, **53**, 1987–1994.
266 N. Tanibata, K. Noi, A. Hayashi and M. Tatsumisago, *RSC Adv.*, 2014, **4**, 17120–17123.
267 Z. Zhang, E. Ramos, F. Lalère, A. Assoud, K. Kaup, P. Hartman and L. F. Nazar, *Energy Environ. Sci.*, 2018, **11**, 87–93.
268 J. W. Fergus, *Solid State Ionics*, 2012, **227**, 102–112.
269 M. Ribes, B. Barrau and J. Souquet, *J. Non-Cryst. Solids*, 1980, **38**, 271–276.
270 S. Susman, L. Boehm, K. Volin and C. Delbecq, *Solid State Ionics*, 1981, **5**, 667–669.
271 V. S. Kandagal, M. D. Bharadwaj and U. V. Waghmare, *J. Mater. Chem. A*, 2015, **3**, 12992–12999.
272 W. D. Richards, T. Tsujimura, L. J. Miara, Y. Wang, J. C. Kim, S. P. Ong, I. Uechi, N. Suzuki and G. Ceder, *Nat. Commun.*, 2016, **7**, 11009.
273 M. Duchardt, U. Ruschewitz, S. Adams, S. Dehnen and B. Roling, *Angew. Chem., Int. Ed.*, 2018, **130**, 1365–1369.
274 X. He, Y. Zhu and Y. Mo, *Nat. Commun.*, 2017, **8**, 15893.
275 S. Shi, P. Lu, Z. Liu, Y. Qi, L. G. Hector Jr, H. Li and S. J. Harris, *J. Am. Chem. Soc.*, 2012, **134**, 15476–15487.
276 Y. Yang, Q. Wu, Y. Cui, Y. Chen, S. Shi, R.-Z. Wang and H. Yan, *ACS Appl. Mater. Interfaces*, 2016, **8**, 25229–25242.
277 Y. Deng, C. Eames, J.-N. l. Chotard, F. Lalère, V. Seznec, S. Emge, O. Pecher, C. P. Grey, C. Masquelier and M. S. Islam, *J. Am. Chem. Soc.*, 2015, **137**, 9136–9145.
278 J. B. Boyce and B. A. Huberman, *Phys. Rep.*, 1979, **51**, 189–265.
279 S. P. Culver, R. Koerver, T. Krauskopf and W. G. Zeier, *Chem. Mater.*, 2018, DOI: 10.1021/acs.chemmater.8b01293.
280 T. Krauskopf, C. Pompe, M. A. Kraft and W. G. Zeier, *Chem. Mater.*, 2017, **29**, 8859–8869.
281 R. Merkle and J. Maier, *Z. Anorg. Allg. Chem.*, 2005, **631**, 1163–1166.
282 N. Hainovsky and J. Maier, *Phys. Rev. B: Condens. Matter Mater. Phys.*, 1995, **51**, 15789.
283 L. Strock, *Z. Phys. Chem., Abt. B*, 1934, **25**, 441–459.
284 C. Liang, *J. Electrochem. Soc.*, 1973, **120**, 1289–1292.
285 J. Maier, *Prog. Solid State Chem.*, 1995, **23**, 171–263.
286 K. Hariharan and J. Maier, *Solid State Ionics*, 1996, **86**, 503–509.
287 A. Schirmeisen, A. Taskiran, H. Fuchs, H. Bracht, S. Murugavel and B. Roling, *Phys. Rev. Lett.*, 2007, **98**, 225901.
288 C. Pfaffenhuber, M. Göbel, J. Popovic and J. Maier, *Phys. Chem. Chem. Phys.*, 2013, **15**, 18318–18335.
289 A. J. Bhattacharyya and J. Maier, *Adv. Mater.*, 2004, **16**, 811–814.
290 R. Bouchet, S. Maria, R. Meziane, A. Aboulaich, L. Lienafa, J.-P. Bonnet, T. N. Phan, D. Bertin, D. Gigmes and D. Devaux, *Nat. Mater.*, 2013, **12**, 452–457.
291 K. D. Kreuer, A. Wohlfarth, C. C. de Araujo, A. Fuchs and J. Maier, *ChemPhysChem*, 2011, **12**, 2558–2560.
292 X. Zhang, T. Liu, S. Zhang, X. Huang, B. Xu, Y. Lin, B. Xu, L. Li, C.-W. Nan and Y. Shen, *J. Am. Chem. Soc.*, 2017, **139**, 13779–13785.
293 J. Zhang, N. Zhao, M. Zhang, Y. Li, P. K. Chu, X. Guo, Z. Di, X. Wang and H. Li, *Nano Energy*, 2016, **28**, 447–454.
294 A. Manthiram, X. Yu and S. Wang, *Nat. Rev. Mater.*, 2017, **2**, 16103.
295 S. Ohta, T. Kobayashi, J. Seki and T. Asaoka, *J. Power Sources*, 2012, **202**, 332–335.
296 Y. J. Nam, S.-J. Cho, D. Y. Oh, J.-M. Lim, S. Y. Kim, J. H. Song, Y.-G. Lee, S.-Y. Lee and Y. S. Jung, *Nano Lett.*, 2015, **15**, 3317–3323.
297 K. Takada, *Acta Mater.*, 2013, **61**, 759–770.
298 K. H. Kim, Y. Iriyama, K. Yamamoto, S. Kumazaki, T. Asaka, K. Tanabe, C. A. Fisher, T. Hirayama, R. Murugan and Z. Ogumi, *J. Power Sources*, 2011, **196**, 764–767.
299 S. Wenzel, T. Leichtweiss, D. Krüger, J. Sann and J. Janek, *Solid State Ionics*, 2015, **278**, 98–105.
300 P. Hartmann, T. Leichtweiss, M. R. Busche, M. Schneider, M. Reich, J. Sann, P. Adelhelm and J. Janek, *J. Phys. Chem. C*, 2013, **117**, 21064–21074.
301 Y. Zhu, X. He and Y. Mo, *ACS Appl. Mater. Interfaces*, 2015, **7**, 23685–23693.

302 F. Han, T. Gao, Y. Zhu, K. J. Gaskell and C. Wang, *Adv. Mater.*, 2015, **27**, 3473–3483.
303 F. Han, Y. Zhu, X. He, Y. Mo and C. Wang, *Adv. Energy Mater.*, 2016, **6**, 1501590.
304 A. Schwöbel, R. Hausbrand and W. Jaegermann, *Solid State Ionics*, 2015, **273**, 51–54.
305 J. Feng, L. Lu and M. Lai, *J. Alloys Compd.*, 2010, **501**, 255–258.
306 U. Alpen, M. Bell, W. Wichelhaus, K. Cheung and G. Dudley, *Electrochim. Acta*, 1978, **23**, 1395–1397.
307 S. Wenzel, T. Leichtweiß, D. A. Weber, J. Sann, W. G. Zeier and J. Janek, *ACS Appl. Mater. Interfaces*, 2016, **8**, 28216–28224.
308 Y. Zhu, X. He and Y. Mo, *J. Mater. Chem. A*, 2016, **4**, 3253–3266.
309 A. Sakuda, A. Hayashi and M. Tatsumisago, *Chem. Mater.*, 2009, **22**, 949–956.
310 W. Zhang, T. Leichtweiß, S. P. Culver, R. Koerver, D. Das, D. A. Weber, W. G. Zeier and J. Janek, *ACS Appl. Mater. Interfaces*, 2017, **9**, 35888–35896.
311 R. Koerver, F. Walther, I. Aygün, J. Sann, C. Dietrich, W. G. Zeier and J. Janek, *J. Mater. Chem. A*, 2017, **5**, 22750–22760.
312 N. Ohta, K. Takada, L. Zhang, R. Ma, M. Osada and T. Sasaki, *Adv. Mater.*, 2006, **18**, 2226–2229.
313 H. Kitaura, A. Hayashi, K. Tadanaga and M. Tatsumisago, *Solid State Ionics*, 2011, **192**, 304–307.
314 K. Takada, N. Ohta, L. Zhang, K. Fukuda, I. Sakaguchi, R. Ma, M. Osada and T. Sasaki, *Solid State Ionics*, 2008, **179**, 1333–1337.
315 N. Ohta, K. Takada, I. Sakaguchi, L. Zhang, R. Ma, K. Fukuda, M. Osada and T. Sasaki, *Electrochem. Commun.*, 2007, **9**, 1486–1490.
316 T. Kato, T. Hamanaka, K. Yamamoto, T. Hirayama, F. Sagane, M. Motoyama and Y. Iriyama, *J. Power Sources*, 2014, **260**, 292–298.
317 A. Sakuda, H. Kitaura, A. Hayashi, K. Tadanaga and M. Tatsumisago, *Electrochem. Solid-State Lett.*, 2008, **11**, A1–A3.
318 Y. Jin, N. Li, C. Chen and S. Wei, *Electrochem. Solid-State Lett.*, 2006, **9**, A273–A276.
319 Y.-S. Hu, *Nat. Energy*, 2016, **1**, 16042.
320 J. Schnell, T. Günther, T. Knoche, C. Vieider, L. Köhler, A. Just, M. Keller, S. Passerini and G. Reinhart, *J. Power Sources*, 2018, **382**, 160–175.
321 R.-J. Chen, Y.-B. Zhang, T. Liu, B.-Q. Xu, Y.-H. Lin, C.-W. Nan and Y. Shen, *ACS Appl. Mater. Interfaces*, 2017, **9**, 9654–9661.
322 T. Liu, Y. Zhang, X. Zhang, L. Wang, S.-X. Zhao, Y.-H. Lin, Y. Shen, J. Luo, L. Li and C.-W. Nan, *J. Mater. Chem. A*, 2018, DOI: 10.1039/C7TA06833F.
323 L. Chen, Y. Li, S.-P. Li, L.-Z. Fan, C.-W. Nan and J. B. Goodenough, *Nano Energy*, 2017, **46**, 176–184.
324 P. Hovington, M. Lagacé, A. Guerfi, P. Bouchard, A. Mauger, C. Julien, M. Armand and K. Zaghib, *Nano Lett.*, 2015, **15**, 2671–2678.